

Conditional Moment Closure Modelling of Turbulent Spray Flames

von der
Fakultät Energie-, Verfahrens- und Biotechnik
der Universität Stuttgart
zur Erlangung der Würde eines
Doktors der Ingenieurwissenschaften
(Dr.-Ing.) genehmigte Abhandlung

vorgelegt von
Satoshi Ukai
aus Kyoto, Japan

Hauptberichter: Prof. Dr. Andreas Kronenburg
Mitberichter: Prof. Dr. rer. nat. habil. Ulrich Maas
Tag der mündlichen Prüfung: 2. Oktober 2014

Institut für Technische Verbrennung
der Universität Stuttgart

2014

Erklärung

Hiermit versichere ich:

1. dass ich meine Arbeit selbständig verfasst habe,
2. dass ich keine anderen als die angegebenen Quellen benutzt und alle wörtlich oder sinngemäss aus anderen Werken übernommenen Aussagen als solche gekennzeichnet habe,
3. dass die eingereichte Arbeit weder vollständig noch in wesentlichen Teilen Gegenstand eines anderen Prüfungsverfahrens gewesen ist,
4. dass das elektronische Exemplar mit den anderen Exemplaren übereinstimmt.

Stuttgart, März 2014

Satoshi Ukai

Preface

Parts of this thesis have been presented at conferences and published in the archival literature. The background and theoretical developments given in chapters 2, 3 and 4 have been modified with respect to the originally published texts and significantly been extended to ensure completeness, coherence and consistency of the present manuscript.

The relevant papers are:

1. S. Ukai, O.T. Stein, and A. Kronenburg, Large eddy simulations of turbulent evaporating acetone spray jets, Cardiff, 2011. Proceedings of 5th European Combustion Meeting.
 - This paper has been published in the conference proceedings. Data and results discussed therein are presented in chapter 6.
 - Author's contribution: Programming (100%), data generation (100%), scientific originality (60%)
2. S. Ukai, A. Kronenburg, O. T. Stein. LES-CMC of a dilute acetone spray flame. *Proceedings of the Combustion Institute*, 34(1):1643–1650, 2013.
 - Data and results discussed in this paper are presented in chapter 7.
 - Author's contribution: Programming (100%), data generation (100%), scientific originality (60%)
3. S. Ukai, A. Kronenburg, O. T. Stein. Simulation of dilute acetone spray flames with LES-CMC using two conditional moments. *Flow Turbulence and Combustion*, 93(3):405–423, 2014.

- Data and results discussed in this paper are presented in chapter 8.
- Author's contribution: Programming (100%), data generation (100%), scientific originality (75%)

4. S. Ukai, A. Kronenburg, O. T. Stein. Large eddy simulation of dilute acetone spray flames using CMC coupled with tabulated chemistry, *Proceedings of the Combustion Institute*, 35(2):1667–1674, 2015.

- Data and results discussed in this paper are presented in chapter 9.
- Author's contribution: Programming (100%), data generation (100%), scientific originality (75%)

Acknowledgements

I would like to acknowledge my supervisor, Prof. Dr. Andreas Kronenburg. He has enlightened me in turbulent combustion research and given me a countless number of suggestions whenever I encounter new problems. Without his support, I would not be able to finish my study. In addition, I would like to affirm his promise that he provides a "happy" life. I did certainly enjoy every aspect of Stuttgart, Germany and Europe.

I would also like to thank Dr. Oliver Stein not only for his dedicated support on my research, but also for being one of the best friends here. I sincerely wish his future happiness and success.

I appreciate Prof. Dr. rer. nat. habil. Ulrich Maas being the examiner for my thesis.

Moreover, all my friends, whom I have shared a large portion of a daily/research life with, are highly acknowledged. My special thanks go to Niko Seubert, Gizem inci, Papakorn Siwaborworn, Gregor Olenik, Son Vo, Jung Choi (for the second time), Dirk BVB Dietzel, Giovanni Luigi Napoli Tufano, Santanu De and Gregor Neuber. And of course, I would appreciate our kind secretary, Frau Ricarda Schubert giving me extraordinary supports.

Last but not least, I sincerely admire my parents and family for their supports and encouragements to pursue my dream.

Contents

Table of Contents	VII
List of Figures	XIII
List of Tables	XIX
Nomenclature	XXI
Kurzfassung	XXIX
Summary	XXXIII
1 Introduction	1
1.1 Motivation	1
1.2 Background	2
1.2.1 Turbulent Flow	3
1.2.2 Turbulent Combustion	4
1.2.3 Two-Phase Turbulent Flow	4
1.3 Present Contributions	5
1.4 Outline	6
2 Gas Phase Formulation and Modelling	7
2.1 Governing Equations	7
2.2 Turbulent Flows	9
2.2.1 Spatial Filtering	10
2.2.2 Favre-Filtered Governing Equations	11

2.3	Mixing and Reacting Fields	12
2.3.1	Mixture Fraction	12
2.3.2	Progress Variable	13
2.4	Scalar Dissipation	14
2.5	Chemical Reaction	16
2.6	Combustion Modelling	17
2.6.1	Algebraic Models	18
2.6.1.1	Eddy Break Up Model	18
2.6.1.2	Eddy Dissipation Model	18
2.6.2	Low Dimensional Manifold Approaches	19
2.6.2.1	The Burke-Schumann and Equilibrium Solutions	19
2.6.2.2	Flamelet Model	19
2.6.2.3	Conditional Moment Closure	20
2.6.2.4	Conditional Source-Term Estimation	21
2.6.3	Stochastic Approaches	21
2.6.3.1	PDF Method	21
2.6.3.2	Multiple Mapping Conditioning	22
2.6.3.3	Linear Eddy Model / One Dimensional Turbulence	22
2.7	Numerical Approach	23
3	Liquid Phase Formulation and Modelling	25
3.1	Backgrounds of Two-Phase Flow Phenomena	25
3.1.1	Preferential Concentration	26
3.1.2	Turbulence Modulation	26
3.1.3	Group Combustion	27
3.2	Review of Two-Phase Flow Modelling Approaches	29
3.2.1	Fully Resolved Droplet	29
3.2.2	Lagrangian Point-Particle Approach	29
3.2.2.1	DNS-Lagrangian Approach	30
3.2.2.2	LES-Lagrangian Approach	30

3.2.2.3	RANS-Lagrangian Approach	31
3.2.3	Eulerian Approach	31
3.3	Lagrangian Approach	32
3.3.1	Particle Dispersion	32
3.3.2	Particle Temperature and Size	33
3.3.3	Two-Way Coupling	35
3.3.4	Numerical Integration	36
4	Conditional Moment Closure	39
4.1	Fundamentals of CMC	39
4.1.1	Conditional Reaction Rate	39
4.1.2	Conditional Filtering	41
4.2	Two-Phase CMC Equations	42
4.3	Closures	43
4.3.1	Conditional Velocity	43
4.3.2	Conditional Scalar Dissipation	44
4.3.3	Conditional Spray Source	46
4.3.4	Heat Radiation	47
4.3.5	Subgrid FDF	48
4.4	Numerical Approach	50
4.4.1	Computational Grid	50
4.4.2	Discretization	50
5	Target Flame Configurations	53
5.1	Burner Configuration	54
5.2	Selection of Target Cases	54
5.3	Numerical Configurations and Setups	56
6	Evaporating Spray Jet	59
6.1	Numerical Modelling Approach	59
6.2	Results and Discussion	60

6.2.1	Mean Velocity Profiles	61
6.2.2	RMS Velocity Profiles	62
6.2.3	Evaporation Rates	63
6.3	Summary	63
7	Turbulent Spray Flame with Conventional CMC	65
7.1	Two-Phase LES-CMC	65
7.1.1	Formulations	65
7.1.2	Definition of Mixture Fraction	66
7.1.3	Boundary Condition in Mixture Fraction Space	67
7.1.4	Conditioning of Spray Source Term	68
7.1.5	Validation of Two-Phase CMC in Cold Flow	69
7.1.6	Implementation of the Two-Phase LES-CMC	71
7.2	Results and Discussion	72
7.2.1	Conditional Moment	72
7.2.2	Unconditional Moment	73
7.2.3	Spray Statistics	75
7.3	Summary	77
8	Two-Conditional Moment Approach	79
8.1	Two-Conditional Moment Approach	80
8.1.1	Formulations	80
8.1.2	LES Representations in Mixture Fraction Space	83
8.1.3	Selection of Upper Mixture Fraction Boundary	84
8.1.4	Interpolation Method	85
8.1.5	Comparisons of CMC and LES Solutions	87
8.1.6	Implementation of the Two-Conditional Moment Approach	88
8.2	Results and Discussion	89
8.2.1	Conditional Moment	89
8.2.2	Unconditional Moment	91
8.2.3	Spray velocity statistics	94

8.3	Summary	95
9	CMC with tabulated chemistry	99
9.1	Coupling of CMC and Tabulated Chemistry	100
9.1.1	Formulations	101
9.1.2	Tabulation of the Composition Space	101
9.1.3	Scaling of the Tabulated Composition Space	102
9.1.4	FDFs and the Integration of Conditional Moments	103
9.1.5	Implementation of CMC with Tabulated Chemistry	106
9.2	Results and Discussion	106
9.2.1	Conditional Moment	107
9.2.2	Unconditional Moment	109
9.2.3	Spray Statistics	112
9.2.4	Model Comparisons	112
9.3	Summary	114
10	Conclusions and Future Work	117
10.1	Conclusions	117
10.2	Recommendations for Future Work	120
	Bibliography	121
	Appendix	141
A	Conditional Scalar Dissipation in Two-Phase Flows	143
A.1	Macroscopic Approach	143
A.2	Microscopic Approach	146
A.2.1	Conditioning on Droplet Surface	146
A.2.2	Droplet in Stationary Flow	147
A.3	Discussion and Summary	149
B	Spray Source Terms in Two-Phase CMC Equations	151
B.1	Behavior of CFD Cell Quantities (Lagrangian Approach)	152

B.2 Behavior of Conditional Moments (Eulerian Approach)	154
B.2.1 Intuitive Discretization Scheme (Model 1)	155
B.2.2 Improved Discretization Scheme (Model 2)	155
B.3 Lagrangian vs. Eulerian approaches	157
B.4 Numerical Implementations in CMC Solver	159
Lebenslauf	161

List of Figures

1.1	World energy consumption by fuel type (quadrillion Btu) (U.S. EIA [179]).	2
1.2	Liquid fuel consumption by sector type (quadrillion Btu) (U.S. EIA [180]).	2
1.3	CO_2 emission in Million Metric Tons (U.S. EIA [180]).	3
3.1	Distributions of particles within isotropic homogeneous turbulence with different St (Yoshimoto and Goto [192]).	26
3.2	Group combustion regimes (Chiu et al. [34]).	28
4.1	Scatter plot of the experimental datasets of Sandia flame D at $z/D=45$ [170]. Solid red lines are the conditional averages of the experimental results.	41
4.2	Diagram of CMC and LES cells. Thick lines indicate CMC cell boundaries, and thin lines represent LES cell boundaries.	50
4.3	Discretization of CMC cells in space [39].	51
5.1	Schematics of the spray burner inlet [118].	55
5.2	Diagrams for the parameters for the acetone flame cases (AcF series) taken from [70]. The lines indicate the blowoff limits. Conditions are identical for the evaporating spray jet case (SP series).	56
6.1	Instantaneous snapshot of the gas axial velocity (color contour), and the liquid droplets (black dots) from Case 1.	60

6.2	Comparisons of computations (Case 1) and experiments of the axial velocities of different particle size classes along the centerline. Lines represent results from the simulations with different particle size classes, and symbols represent the experimental results of each corresponding class.	61
6.3	Comparisons of numerical predictions and experimental results for the axial velocity, W , (right half) and the radial velocity, V , (left half). Green dots represent computed particle velocities from Case 1, and all statistics are based on particle size Class 2.	62
6.4	Comparisons of numerical predictions and experimental results for the rms of axial (right half) and radial velocities (left half). All statistics are based on particle size Class 2.	63
6.5	Comparisons of the liquid flow rates of simulations and experiments.	64
7.1	Conceptual issues with mixture fraction boundaries in two-phase flows.	68
7.2	An example of spray source term conditioned on ξ_{surf} . Black line - conditional moment of CO_2 , red line - the spray source term (the third term of RHS in Eqn. 7.2) with Π conditioned on ξ_{surf} , green line - Probability within the CMC cell constructed by assumed PDF by $\tilde{\xi}$ and $\tilde{\xi}''^2$	70
7.3	Comparison of acetone mass fraction in mixture fraction space at $z/D=5$. Solid line - CMC spray source terms on; dashed line - CMC spray source terms off; scattered green dots - solution of Eqn. 2.31 for acetone with the LES-filtered spray source term on.	71
7.4	Flowchart of the conventional CMC approach in two-phase flows.	72
7.5	Comparison of Q_{CO_2} and Q_{Ace} . Solid line - $z/D=10$, dashed line - $z/D=30$, black line - with spray source terms, red line - without spray source terms.	73

7.6	Temperature profile over mixture fraction. Solid line - $z/D=10$, dashed line - $z/D=30$, black line - with spray source terms, red line - without spray source terms.	74
7.7	Radial profiles of mean temperature. Crosses - experiments [113], solid line - with spray source terms, dashed line - without spray source terms.	75
7.8	Instantaneous contour plot of AcF3 with conventional CMC.	76
7.9	Mean (right) and rms (left) axial droplet velocity profiles for the diameter range 20-30 μm . Crosses - experiments [113], green scatter points - single realization of a simulated droplet, black line - with spray source terms, line - without spray source terms.	76
7.10	Mean (right) and rms (left) axial droplet velocity profiles for the diameter range 20-30 μm at $z/D=20$. Crosses - experiments [113], green scatter points - single realization of a simulated droplet, black line - with spray source terms, blue line - with spray source terms and stochastic spray terms.	77
8.1	Realizations of $\tilde{\xi}_\Delta$ within a CMC cell that lies within the jet core (black) and a CMC cell at the interface of the jet core and the pilot (red). The green line is ξ_{base} (Eqn. 8.13). The condition is based on AcF 3 (Table 5.1).	84
8.2	Estimation of ξ_{UL} . Cross - actual quantity in a LES cell ($\tilde{\xi}_{tot}$, $\tilde{\xi}_\Delta$), circle - (imaginary) unmixed property corresponding to the LES cell (ξ_{UL} , $\xi_{\Delta, @\xi_{UL}}$), solid line - mixing line, dashed line - ξ_{base}	86
8.3	Realization of $\tilde{\xi}_\Delta$ in the CMC cell over the core (black crosses) and the pilot (red square) with $\langle \xi_\Delta \eta \rangle$ (blue line). The green line is the base mixture fraction (Eqn. 8.13).	87
8.4	Realization Y_{ace} of LES (black plus symbol) and CMC (red X symbol) solutions over profiles of $Q_{ace,tot}$ (green line) and $Q_{ace,cons}$ (blue line).	88
8.5	Flowchart of the two-conditional moment approach.	89

8.6	Instantaneous conditionally averaged mass fractions of acetone (left) and OH (right) in flame AcF 3. The center of each CMC cell is located ($r/D=0, z/D=10$) - black, ($r/D=0, z/D=20$)- red and ($r/D=0.8, z/D=20$) -blue. Solid line - Q_{tot} , dashed line - Q_{cons}	90
8.7	Instantaneous conditionally averaged mass fraction of acetone (left) and OH (right) at ($r/D=0.8, z/D=20$) for the different flames. Black - AcF 2, red - AcF 3 and blue - AcF 5. Solid line - Q_{tot} , dashed line - Q_{cons}	91
8.8	Instantaneous LES values and conditional moments plotted over mixture fraction for different CMC cells in flame AcF 3. The centers of the CMC cells are located at ($r/D=0, z/D=10$) - black; ($r/D=0, z/D=20$) - red; ($r/D=0.8, z/D=20$) - blue.	92
8.9	Radial profiles of mean temperature. Crosses - experiments [113], solid line - the two-conditional moment approach, dashed line - one-conditional moment approach.	93
8.10	Instantaneous Contour plot of AcF3 with the two-conditional moment approach.	94
8.11	Mean axial droplet velocity profiles for the diameter range 20-30 μm . Crosses - experiments [113], scatter points - single realization of a simulated droplet, solid line - the two-conditional moment approach, dashed line - one-conditional moment approach.	95
8.12	rms of axial droplet velocity profiles for the diameter range 20-30 μm . Crosses - experiments [113], solid line - the two-conditional moment approach.	96
9.1	Diagram of the joint FDF structures. Black solid line - Q_c , purple dashed line - $\langle c \eta \rangle_{LES}^*$, brown square dotted line - $P(\eta)$ constructed by assuming a β -FDF with $\tilde{\xi} = 0.12$, $\tilde{\xi}''^2 = 0.004$ and $\xi_{UL} = 0.162$, circle - $(\tilde{\xi}, \tilde{c})$, cross - $(\tilde{\xi}, \tilde{c}_{cmc})$	105
9.2	Flowchart of CMC coupled with LES using tabulated chemistry (CMCe).	106

9.3	Progress variable comparisons. Green dots - LES-filtered values; Black solid line - conditionally averaged LES-filtered values $\langle c \eta \rangle$; Red solid line - CMC solution Q_c ; dashed line - $P_{CMC}(\eta)$ within the corresponding CMC cell.	108
9.4	Effects of joint FDF modelling on progress variable at $z/D=20$ in flame AcF 3. Solid line - $\langle c \eta \rangle$ using the correlated joint FDF (Eqn. (9.14)); dashed line - $\langle c \eta \rangle$ using the statistically independent joint FDF Eqn. (9.12); red line - Q_c	109
9.5	Conditional averages of four species constituting the progress variable: comparison of the CMC solution ($Q_\alpha(\eta)$ - solid line), with the respective values from unscaled chemistry table ($\int Q_\alpha^0(\eta, \zeta) P_{LES}(\zeta \eta) d\zeta$ - dashed line). Black lines - $z/D=10$, red lines - $z/D=30$	110
9.6	Mean temperature profiles. Solid lines - CMCe, dashed lines - conventional CMC without spray source term in CMC equations, X - experiment with error bars.	111
9.7	Instantaneous contour plot of AcF3 with CMCe.	112
9.8	Radial profiles of the mean axial droplet velocities for the droplet diameter range 20-30 μm . Solid line - CMCe, scattered green points - single realization of a simulated droplet, dashed line - conventional CMC without spray source term in CMC equations, X - experiment with error bars.	113
9.9	Radial profiles of rms of the axial droplet velocity for the diameter range 20-30 μm of AcF 3. Solid line - CMCe, X - experiment with error bars.	114
9.10	Left - radial profiles of mean temperature, right - radial profiles of the mean axial droplet velocities for the droplet diameter range 20-30 μm . Crosses - experiments, black solid line - conventional CMC with spray source terms (Chapter 7), red line - the two-conditional moment approach (Chapter 8), blue line - CMC with tabulated chemistry (This Chapter).	116

A.1	Comparisons of the mixture fraction variances.	145
A.2	Scalar dissipation rates in different physical scale.	150
B.1	Comparisons of Y_{ace} profiles between before and after the addition of the spray source term. Black circles - CFD cell quantities at the time step n , red circle - CFD cell quantities at the time step $n + 1$	154
B.2	Comparisons of acetone species profile: Green line - CMC solution with conventional discretization, Blue crosses - CFD cell solutions in the initial profile (at n), Black crosses - CFD cell solutions after the evaporation process (at $n + 1$).	156
B.3	Comparisons of acetone species profile with improved discretization approaches: Red line with circles - CMC solution with Model 2, Green line - CMC solution with Model 1, Black crosses - CFD cell solutions after the evaporation process.	157
B.4	Comparisons of acetone profiles. Red line with circles - the improved discretization, green line - the intuitive discretization, blue line - the averaged from the Lagrangian solutions, crosses - the analytical Lagrangian solution. Π is taken as the random uniform distribution ranged $[0, 0.04]$	158

List of Tables

5.1	Parameters of an evaporating spray jet (SP) and reacting acetone flames (AcF).	56
5.2	Grid size and chemistry used in each methodology.	58
A.1	Closures of σ_s based on the variance transport equation. $\tilde{\Pi}$ is the volume expansion rate per unit volume, $\tilde{\Pi} = \frac{1}{\bar{\rho}V} \sum_{i=1}^{N_d} \dot{m}_i$, \dot{m}_i is the mass evaporation rate of i -th droplet, N_d is the number of the droplets per LES cell, V is the cell volume, and ξ_{surf} is the mixture fraction at each droplet surface.	145

Nomenclature

Roman Symbols

A	pre-exponential factor	$(\text{m}^3/\text{mol})^a/\text{s}$
b	temperature exponent of Arrhenius law	
B_M	Spalding mass transfer coefficient	
B_T	Spalding heat transfer coefficient	
c	progress variable	
c_p	specific heat capacity at constant pressure	$\text{J}/(\text{Kg} \cdot \text{K})$
C_0	stochastic dispersion model coefficient	
C_D	drag coefficient	
C_{EBU}	EBU coefficient	
C_s	Smagorinsky constant	
C_M	molar concentration	mol/m^3
C_N	coefficient for subgrid scalar dissipation rate	
C_V	stochastic evaporation model coefficient	
C_ξ	coefficient for mixture fraction variance	
D	mass diffusivity	m^2/s
D	nozzle diameter	m
D_t	turbulent diffusivity	m^2/s
E_a	activation energy in reaction	J/mole
e_{rad}	radiation heat transfer rate	J/s
f	scalar	

\dot{F}_i	spray source term of momentum	kg/(m ² · s ²)
F_M	correction factor of particle mass transfer	
F_T	correction factor of particle heat transfer	
G	filter kernel	
G	group combustion number (In Sec. 3.1.3)	
g	scaling factor	
h	total enthalpy	J/m ³
h_f^0	enthalpy of formation	J/m ³
h_s	sensible enthalpy	J/m ³
h_{fg}	latent heat of evaporation	J/m ³
J	species mass diffusion	kg/(m · s)
k	reaction rate coefficient	(m ³ /mol) ^a /s
k	turbulent kinetic energy	m ² /s ²
k^{sgs}	subgrid turbulent kinetic energy	m ² /s ²
l	integral length scale	m
Le	Lewis number	
m_p	mass of particle	kg
\dot{m}_p	evaporation rate of particle	kg/s
M	representing molecule	
MW	molecular weight	g/mol
l	integral length scale	m
L_{box}	domain size	m
N	scalar dissipation	1/s
N	number of droplets in a cloud	
N_{cell}	number of computational grid	
N_d	number of droplets,	
N_{res}	resolved scalar dissipation	1/s
N_s	number of species	
N_{sgs}	subgrid scale scalar dissipation	1/s
Nu	Nusselt number	

p	pressure	Pa or $\text{kg}/(\text{m} \cdot \text{s}^2)$
P	probability	
Pr	Prandtl number	
Pr_t	turbulent Prandtl number	
q	heat diffusion flux	$(\text{kg} \cdot \text{J})/(\text{m} \cdot \text{s})$
\dot{Q}	spray source term of enthalpy	$\text{J}/(\text{m}^3 \cdot \text{s})$
Q_α	conditionally filtered mass fraction of species α	
Q_h	conditional enthalpy	J
r_l	radius of droplet	m
R	specific gas constant	$\text{J}/(\text{K} \cdot \text{kg})$
R_b	radius of droplet clouds	m
R_u	universal gas constant	$\text{J}/(\text{K} \cdot \text{mol})$
Re	Reynolds number	
Re_d	droplet Reynolds number	
S	oxygen-fuel stoichiometric mass ratio	
S	nondimensional separation (In Sec. 3.1.3)	
S_{ij}	strain rate tensor	1/s
Sc	Schmidt number	
Sc_t	turbulent Schmidt number	
Sh	Sherwood number	
St	Stokes number	
T	temperature	K
T_B	boiling temperature	K
t	time	s
u	flow velocity	m/s
v_p	particle velocity	m/s
T	temperature	K
W	Wiener process	s
x	spatial coordinate	
x_p	position of a droplet	

Y	mass fraction of species
Z	mass fraction of element

Greek Symbols

α	species	
α	model coefficient of τ_t	
α_h	thermal diffusivity	m^2/s
Γ	Gamma function	
Δ	grid width	m
δ	Dirac delta function	
δ_{ij}	Kronecker delta function	
ϵ	scalar dissipation rate	$1/\text{s}$
ζ	sample space variable in progress variable space	
η	sample space variable in mixture fraction space	
η	Kolmogorov length scale	t
θ	weighting factor	t
μ	dynamic viscosity	$\text{kg}/(\text{s} \cdot \text{m})$
μ_t	eddy viscosity	$\text{kg}/(\text{s} \cdot \text{m})$
ν	kinematic viscosity	m^2/s
ν_t	turbulent kinematic viscosity	m^2/s
ν'	stochastic coefficient of reactants	
ν''	stochastic coefficient of reactants	
ξ	mixture fraction	
ξ_{base}	base mixture fraction	
ξ_{cons}	conservative mixture fraction	
ξ_{jet}	mixture fraction at jet	
ξ_{surf}	mixture fraction at droplet surface	

ξ_{tot}	total mixture fraction	
ξ_{LL}	Lower boundary of mixture fraction space	
ξ_{UL}	Upper boundary of mixture fraction space	
ξ_{Δ}	vapour mixture fraction	
$\widetilde{\xi''^2}$	subgrid-scale variance of mixture fraction	
Π	volumetric fuel evaporation rate per unit volume	m^3/s
ρ	density	kg/m^3
$\dot{\rho}$	spray source term of mass	$\text{kg}/(\text{m}^3 \cdot \text{s})$
σ_B	Stefan-Boltzmann constant	$\text{kg}/(\text{s}^3 \cdot \text{K}^4)$
σ_s	spray source term of mixture fraction variance	kg/m^3
τ_{ij}	viscous stress tensor	$\text{kg}/(\text{m} \cdot \text{s}^2)$
τ_p	particle response time	s
τ_t	subgrid flow time scale	s
Φ	scalar	
ψ	fine-grained PDF	
Ψ	energy transfer rate	J/s
ω	reaction rate	1/s

Operators

$\langle \rangle$	conditional average
$-$	spatial filtered average
\sim	Favre (density-weighted) filtered average
\cdot	spray source term

Super- and Subscripts

$()_{ace}$	function of acetone
$()_{cons}$	function of conservative mixture fraction
$()^{sgs}$	subgrid scale
$()_{tot}$	function of total mixture fraction
$()_{\eta}$	conditional average

Abbreviations

BOFFIN	BOundary Fitted Flow INtegrator
BC	boundary condition
CFD	computational fluid dynamics
CMC	conditional moment closure
CMCe	extended conditional moment closure
CP	carrier phase
CSE	conditional source-term estimation
DNS	direct numerical simulation
EBU	eddy break up model
EDM	eddy dissipation model
EPFM	Eulerian particle flamelet model
FDF	filtered probability density function
FGM	flamelet generated manifold
FPI	flame prolongation of intrinsic low-dimensional manifold
FVM	finite volume method
FSSF	fully stochastic separated flow
GRI	Gas Research Institute
IC	internal combustion

ILDm	intrinsic low-dimensional manifolds
LEM	linear eddy model
LES	large eddy simulation
LIF	laser induced fluorescence
LHS	left hand side
MMC	multiple mapping conditioning
ODT	one dimensional turbulence
PDF	probability density function
PDA	phase-Doppler anemometry
PM	particle matter
RANS	Reynolds-averaged Navier-Stokes
REDIM	Reaction-Diffusion Manifold
RHS	right hand side
RMS	root mean square
SIMPLE	semi-implicit method for pressure-linked equations
TCS	turbulent spray combustion
TNF	turbulent non-premixed flames
TVD	total variation diminishing

Kurzfassung

Das Ziel der vorliegenden Arbeit ist die Entwicklung einer verbesserten Methode zur Simulation turbulenter Sprayflammen. Die Sprayverbrennung ist ein typisches Multiskalenproblem. Es ist praktisch nicht möglich alle relevanten physikalischen Skalen aufzulösen, weshalb geeignete Modelle für die nicht aufgelösten Skalen verwendet werden müssen. Innerhalb dieser Arbeit werden Large-Eddy Simulationen (LES) für die Berechnung des Strömungsfeldes zusammen mit dem Conditional Moment Closure (CMC) Ansatz zur Modellierung der Turbulenz-Chemie Interaktion verwendet. Basierend auf einer Lagrange'schen Partikelbeschreibung mit stochastischer Modellierung des Transports und der Verdampfung von Tropfen wird die Flüssigphase erfasst und mit LES und CMC zu einem vollständigen Modell für die Sprayverbrennung gekoppelt.

Der LES Strömungslöser und die Modelle für die Flüssigphase wurden durch einen Vergleich mit Experimenten eines verdampfenden Sprayjets validiert. Die numerischen Voraussagen zeigen eine gute Übereinstimmung mit den experimentellen Messungen. Der Einfluss der stochastischen Partikelverteilung und der Verdampfungsmodelle wurde untersucht. Die stochastische Verteilung hat, wahrscheinlich aufgrund der niedrigen Turbulenzintensität in den untersuchten Fällen, keinen starken Einfluss auf die Statistik der Tropfenverteilung. Allerdings wurden bei Verwendung des stochastischen Verdampfungsmodells erhöhte Verdampfungsraten festgestellt.

In einem weiteren Schritt wurden die Effekte zusätzlicher Terme in der CMC Formulierung, die durch das Vorhandensein verdampfender Tropfen aufkommen, durch einen Vergleich mit Experimenten einer turbulenten Ethanol-Sprayflamme unter-

sucht. Insgesamt zeigen die numerischen Ergebnisse eine gute Übereinstimmung mit den Experimenten, aber große Abweichungen der Temperatur entlang der Mittelachse wurden in stromab gelegenen Bereichen beobachtet. Die Gründe hierfür liegen in den relativ einfachen konventionellen Randbedingungen, die für diese ersten Untersuchungen verwendet worden sind. Die einfache Behandlung der Randbedingungen kann für einfache Gasflammen oder Sprayflammen ohne Vorverdampfung ausreichen. Allerdings sind diese Randbedingungen für die innerhalb dieser Arbeit untersuchten Sprayflammen nicht gültig. Eine neue Behandlung der Randbedingungen für die obere Grenze im Mischungsbruchraum ist erforderlich und deshalb wurden zwei neue Ansätze für eine konsistente Modellierung von Sprayflammen mit Vorverdampfung vorgeschlagen und entwickelt.

Das erste Modell ist ein *Two-Conditional-Moment* Ansatz. Hierbei werden zwei Sätze *Conditional Moments* gelöst. Der erste Satz wird auf einen vollständig erhaltenen Mischungsbruch konditioniert und berücksichtigt die Tropfenverdampfung nicht. Der zweite Satz ist auf einen Mischungsbruch konditioniert, der auf der Summe aus vorverdampftem und in der Brennkammer verdampftem Brennstoff basiert. Die LES Lösung kann aus den gewichtet gemittelten und über den Mischungsbruchraum integrierten Conditional Moments ermittelt werden. Der Ansatz mit zwei Conditional Moments wurde zur Simulation turbulenter Sprayflammen verwendet und die Ergebnisse sind im Vergleich zur konventionellen Methode deutlich besser.

Das zweite Modell basiert auf einem CMC Ansatz der an tabellierte Chemie gekoppelt ist. CMC beschreibt dabei die instationären und inhomogenen Conditional Moments, wohingegen die tabellierte Chemie im Pre-Processing erstellt wird und sich in Raum und Zeit nicht verändert. Die tabellierte Chemie kann auch in Abhängigkeit mehrerer charakteristischer Variablen erstellt werden, während in CMC typischerweise auf eine bestimmende Größe konditioniert wird. Deshalb wurde CMC mit tabellierter Chemie entwickelt, um die Vorteile der beiden Ansätze zu verbinden. Die numerischen Simulationen wurden gegen experimentelle Daten validiert und zeigen insgesamt gute Übereinstimmung mit allen aus den Experimenten verfügbaren Daten.

Zusammenfassend wurden eine neue Methode zur Behandlung der Randbedingung für den Mischungsbruch und zwei neue CMC Ansätze entwickelt, die die Anwendbarkeit der CMC Modellierung auf Sprayflammen mit teilweise verdampftem Brennstoff erweitern. Die neuen Modelle wurden durch Vergleiche mit Messungen einer Serie von Sprayflammen validiert, die an der Universität Sydney durchgeführt worden sind. In zukünftigen Arbeiten sollen die neuen Ansätze auf komplexere Flammenbereiche wie z.B. eine teilweise vorgemischte Sprayflamme erweitert werden.

Summary

The scope of this thesis is to develop an improved methodology for the simulation of turbulent spray flames. Spray combustion is a typical multi-scale problem. It is practically impossible to resolve all physical scales, and appropriate models need to be used for the subgrid scales. Here, large eddy simulation (LES) for the computation of the flow field, conditional moment closure (CMC) for the modelling of turbulence-chemistry interactions, and a Lagrangian particle tracking approach with stochastic droplet modelling for transport and evaporation of the droplets are combined to form a comprehensive spray combustion model.

The LES flow solver and the liquid phase models have been validated by comparison with experimental data from an evaporating spray jet. The numerical predictions show good agreement with the measurements. The influence of the stochastic particle dispersion and evaporation models is assessed. The stochastic dispersion does not have large effects on the droplet dispersion statistics probably due to low levels of turbulence in the cases investigated here. However, higher evaporation rates are seen when the stochastic evaporation model is used.

In a further step, the effects of additional terms in the CMC formulation that arise due to the presence of the evaporating droplets are investigated by comparison with experiments from a series of turbulent ethanol spray flames. Overall, the numerical predictions show good agreement with measurements, but large discrepancies of centerline temperature are found in downstream regions of the flow. The reasons can be found in the rather simplistic conventional boundary conditions used in this first study. The simplistic boundary treatment may suffice for simple gaseous flames or spray flames without pre-evaporation. However, it is not applicable to the

spray flames under investigation here, and a new boundary treatment of the upper limit in mixture fraction space is necessary. Therefore, two novel approaches are proposed and developed for the consistent CMC modelling of spray flames with pre-evaporation.

The first model is a two-conditional moment approach. It solves for two sets of conditional moments. The first set is conditioned on a fully conserved mixture fraction that does not take droplet evaporation into account. The second set is conditioned on a mixture fraction that is based on the fuel originating from the pre-evaporated droplets plus the fuel evaporated within the combustion chamber. The LES solution can be found by using the weighted average of these two conditional moments and integration across mixture fraction space. The two-conditional moment approach is applied to simulate the turbulent spray flames and the accuracy of the numerical predictions is markedly improved when compared to the conventional approach.

The second model is based on a CMC approach coupled with tabulated chemistry. CMC can solve for unsteady and inhomogeneous conditional moments, whereas tabulated chemistry is pre-processed and it is usually not a function of space or time. On the other hand, tabulated chemistry can be constructed over multiple sampling spaces, while CMC is typically conditioned on only one characteristic quantity. Therefore, CMC with tabulated chemistry is developed to couple the advantages of the two approaches. The numerical simulations have again been validated by comparison with experiments, and overall good agreement with all available experimental data are obtained.

In conclusion, a new mixture fraction boundary treatment and two novel CMC approaches have been developed that expand the applicability of CMC to spray flames with partial pre-evaporation of the fuel. The new models are validated by comparison with measurements from a spray flame series conducted at the University of Sydney. Future work will seek the extension of the current approaches to more complex flame regimes such as partially premixed spray flames.

Chapter 1

Introduction

1.1 Motivation

Liquid fuel is utilized by many modern combustion devices such as IC engines, gas turbines, aircraft engines and rocket propulsion, and it plays an important role in our daily life. In fact, liquid fuel has been the largest energy resource in the world as shown in Fig. 1.1. Moreover, the consumption of liquid fuel has been increased till now, and it is even expected to increase 1.1 % every year in future [179]. Also, a large portion of liquid fuels is consumed in transportation (Fig. 1.2). Therefore, an improvement of the efficiency of liquid combustion devices directly benefits the life of end users. On the other hand, liquid fuel is responsible for pollution to a great extent. For example, the largest CO_2 emission originates from petroleum (liquid fuel) and transportation (Fig. 1.3). Also, it causes many other pollutants such as NO_x , CO , SO_x and particulates that must be regulated to maintain air quality [111]. Thus, liquid combustion devices must be developed to increase performance and reduce pollutants, but it is still difficult to perform such an optimization since physics of turbulent spray combustion is not yet fully understood [82]. Various types of experimental studies have been carried out to gain fundamental knowledge, and parametric studies have been conducted. At the same time, the recent increase of the computational resources enables detailed simulations of large scale devices, and CFD is considered to be a more valuable tool in terms of design and optimization. For

that purpose, it is necessary to simulate turbulent spray combustion accurately, but a difficulty arises from the very wide physical length scales of turbulence, droplets and chemical reactions. Since it is practically impossible to resolve all physical scales, the turbulence-spray-chemistry interaction must be modelled appropriately. Therefore, the aim of the present study is to develop a methodology to simulate turbulent spray flames.

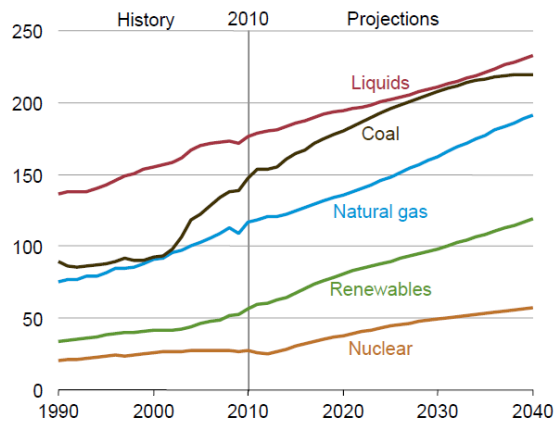


Figure 1.1: World energy consumption by fuel type (quadrillion Btu) (U.S. EIA [179]).

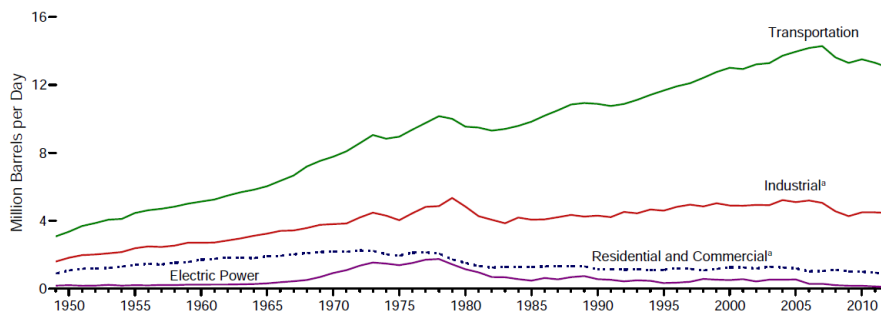


Figure 1.2: Liquid fuel consumption by sector type (quadrillion Btu) (U.S. EIA [180]).

1.2 Background

Since turbulent spray flames involve multiscale phenomena, small scale physics are described by sub-grid models. Here, a development of each sub-model is briefly reviewed.

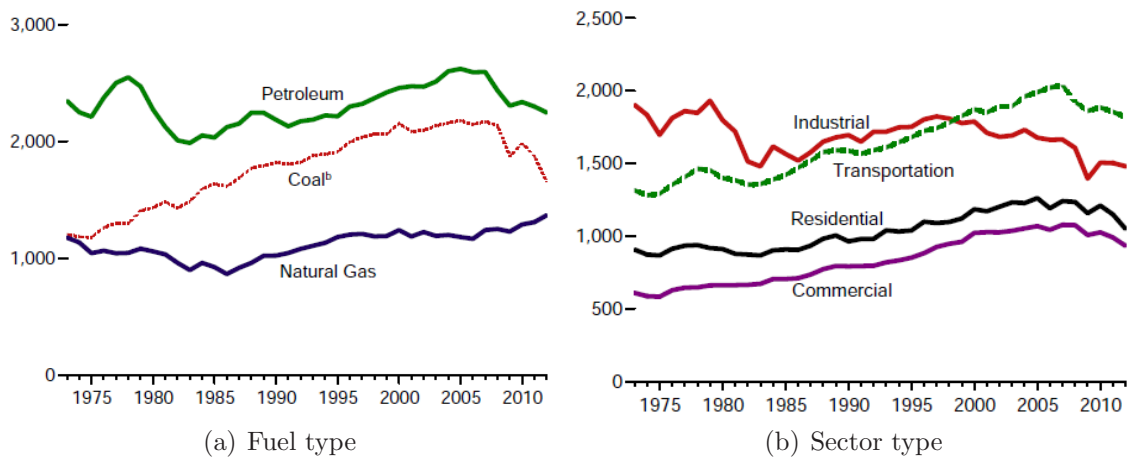


Figure 1.3: CO_2 emission in Million Metric Tons (U.S. EIA [180]).

1.2.1 Turbulent Flow

Turbulent flows are characterized by various sizes of eddies, and direct numerical simulation (DNS) can be performed to resolve the smallest eddy size. Even though DNS can provide insights of turbulent flow physics, it is not feasible to perform DNS on a practical engineering device due to limitations of computational resources. Thus, multiple modelling approaches have been proposed. Reynolds-averaged Navier-Stokes (RANS) equations provide a time-averaged solution. However, there are some physical phenomena unsuitable for RANS analysis, especially when unsteady effects play very important roles such as flow separation or instability. On the other hand, large eddy simulation (LES) solves unsteady spatially-averaged equations to capture large scale motions while modelling subgrid fluctuations. LES can capture unsteady turbulent physics with a reasonable computational power. In the 1980s and early 1990s, LES has been usually applied with a tuned model coefficient depending on a flow configuration. A breakthrough was made by the introduction of the dynamic subgrid scale model [65] based on the scale similarity within the inertial range. The dynamic subgrid model provided more flexibility of applicability of the LES, and other dynamic models have been developed later on [92]. Recently, investigations of LES closures have been extended to more complex environments such as turbulence in a compressible flow [64, 8, 29] and magnetohydrodynamic turbulence [119].

1.2.2 Turbulent Combustion

Turbulence is often favored in combustion devices since it enhances mixing (of fuel/oxidizer in non-premixed flames and of reactants/products in premixed flames) and eventually leads to higher reaction rates. Therefore, an accurate turbulent combustion model is necessary to develop a modern combustion device. One of the most challenging issues is the modelling of the filtered chemical source terms. Since the term is highly non-linear, a first order approximation is usually insufficient. Thus, various combustion models have been developed to close these terms along with LES or RANS, such as the flamelet approach [144, 79, 186], the PDF model [147], the linear-eddy model [117], the Eulerian stochastic field method [86], the multiple mapping conditioning (MMC) [63] and the conditional moment closure (CMC) [132] and so on.

1.2.3 Two-Phase Turbulent Flow

Many combustion devices are operated with liquid fuel, and it is important to model droplet behavior. One of the most popular and flexible models is the Lagrangian scheme that tracks individual particle motions and conditions. Turbulent fluctuations can influence dispersion and evaporation processes of droplets, and such small scale interactions must be considered properly. Stochastic models have been proposed for RANS applications [18]. Since RANS captures only the mean profiles, the stochastic model plays a very important role in droplet dispersion. However, it is worth noting that the stochastic model does not necessarily improve instantaneous droplet distributions. For example, preferential concentration of particles found in DNS analysis [56] cannot be captured in RANS, since there is no turbulent eddy resolved in the flow field, and the model is usually based on single point statistics which means that stochastic fluctuations in each particles are independent. In an LES, the large eddies resolved in the flowfield are considered to have large effects on the particle behavior, so the subgrid effects are often considered to be small and neglected [123, 117, 5]. However, some studies claim that subgrid fluctuations in the

LES cell have large influences, and stochastic dispersion and evaporation models are proposed [15, 16, 17, 150, 47].

1.3 Present Contributions

The scope of this study is to establish methodologies to simulate turbulent spray flames. An LES-CMC formulation is chosen since it has been very well validated for many types of the flame configurations such as piloted flames [132, 61], bluff-body flames [129] and lifted flames [130, 137, 131, 165]. Also, the Lagrangian scheme is used to model the spray behavior, and the stochastic models are applied to include subgrid turbulence fluctuations. Then, the study focuses on the interactions of turbulence-spray-chemistry.

Several early studies have applied single-phase CMC equations to simulate spray combustion in RANS [191, 190] and LES [21]. Also, some simplified two-phase CMC formulations have been utilized in RANS [91, 154]. Later, Mortensen and Bilger [126] mathematically derived extra terms within the CMC equation for spray combustion, and they were applied to turbulent spray flames successfully in auto-ignition studies [20, 172], where one conditional moment can sufficiently approximate the correct solution. This study focuses on the development of robust models based on the LES-CMC approach to simulate turbulent spray flames with pre-evaporation. First, an evaporating spray jet is analyzed to validate the LES and the Lagrangian scheme. Then, CMC with spray source terms is tested on a turbulent spray flame, and a detailed analysis of modelling difficulties is reported. To cope with the issue, two novel approaches are introduced: a two-conditional moment approach and CMC with tabulated chemistry. The two-conditional moment approach solves for two conditional moments based on different mixture fractions to account for conditional variations in the flow field. Similarly, CMC with tabulated chemistry combines the CMC solution and tabulated chemistry with a progress variable to allow for conditional fluctuations. These novel methodologies are validated against a recent set of turbulent spray flame experiments performed by Masri and Gounder [113, 69].

1.4 Outline

The outline of this thesis is as follows: Chapter 2 introduces the gas phase formulations. The Favre-filtered transport equations are introduced, and modelling approaches for the subgrid terms are explained. The Lagrangian particle tracking approach is discussed in Chapter 3. The governing equations of particle dispersion and evaporation models are outlined, and stochastic terms to model the turbulence-droplet interactions are discussed. In Chapter 4, a background of CMC is given, and the two-phase CMC equations and the closures are discussed. Chapter 5 explains the target experiments. The experimental configurations are described, and conditions of turbulent spray flame experiments are presented. The simulations of non-reacting evaporating spray jets are conducted in Chapter 6. The effects of the stochastic terms in the Lagrangian method are analyzed. Then, the study is further extended to a simulation of turbulent spray flames in Chapter 7. CMC including spray source terms is applied, and the results of the simulation and the modelling limitations are discussed. To resolve some arising shortcomings of the CMC approach, a new methodology called “two-conditional moment approach” is introduced in Chapter 8. The modelling approach is described, and improvements in the results are discussed. Chapter 9 proposes another methodology called “CMC with tabulated chemistry”. The formulation and the implementation of the methodology are explained, and the results are discussed. Chapter 10 concludes the present work and provides suggestions for future improvements.

Chapter 2

Gas Phase Formulation and Modelling

2.1 Governing Equations

The mass and momentum equations for a dilute spray (with negligible liquid volume fraction) are expressed by the Einstein notation as [43, 148]

$$\frac{\partial \rho}{\partial t} + \frac{\partial}{\partial x_j}(\rho u_j) = \dot{\rho}, \quad (2.1)$$

$$\frac{\partial}{\partial t}(\rho u_i) + \frac{\partial}{\partial x_j}(\rho u_i u_j) = -\frac{\partial p}{\partial x_i} + \frac{\partial \tau_{ij}}{\partial x_j} + \dot{F}_i, \quad (2.2)$$

where ρ is density, u_i is the velocity component in the i -direction, p is pressure and τ_{ij} denotes the viscous stress tensor. $\dot{\rho}$ and \dot{F}_i are source terms accounting for the mass and momentum added from the liquid to the gas phase. The viscous stress tensor is expressed as a function of the strain rate tensor, S_{ij} .

$$\tau_{ij} = \mu \left[2S_{ij} - \frac{2}{3} \delta_{ij} \frac{\partial u_k}{\partial x_k} \right], \quad (2.3)$$

where μ is the dynamic viscosity, δ_{ij} denotes the Kronecker delta and the strain rate tensor, S_{ij} , is defined as

$$S_{ij} = \frac{1}{2} \left(\frac{\partial u_i}{\partial x_j} + \frac{\partial u_j}{\partial x_i} \right). \quad (2.4)$$

The transport equations of the reactive scalars are

$$\frac{\partial}{\partial t}(\rho Y_\alpha) + \frac{\partial}{\partial x_j}(\rho u_j Y_\alpha) = -\frac{\partial J_{\alpha,j}}{\partial x_j} + \rho \omega_\alpha + \dot{\rho}_\alpha, \quad (2.5)$$

$$\frac{\partial}{\partial t}(\rho h) + \frac{\partial}{\partial x_j}(\rho u_j h) = -\frac{\partial q_j}{\partial x_j} + \dot{Q}, \quad (2.6)$$

where Y is the mass fraction, ω is the reaction rate, J_α is the diffusion flux of the α -th species, h is enthalpy, and q is the heat flux. $\dot{\rho}_\alpha$ and \dot{Q} are source terms describing mass and enthalpy transfer from the liquid to the gas phase. Note that low Mach number is assumed, so that the work term and the kinetic energy in the enthalpy equation are neglected. The enthalpy is defined assuming ideal gas as

$$h(T) = \sum_{\alpha=1}^{N_s} Y_\alpha \left(\Delta h_{f,\alpha}^0 + \int_{T_0}^T c_{p,\alpha}(T') dT' \right), \quad (2.7)$$

where N_s is the number of the species, c_p is the specific heat capacity at constant pressure and h_f^0 is the enthalpy of formation at the reference state. The species diffusion flux is modelled by the gradient model (Fick's law) as

$$J_{\alpha,j} = -\rho D_\alpha \frac{\partial Y_\alpha}{\partial x_j} = -\frac{\mu}{Sc} \frac{\partial Y_\alpha}{\partial x_j}, \quad (2.8)$$

where D_α is the diffusion coefficient of α , and Sc is the Schmidt number $Sc = \frac{\mu}{\rho D_\alpha}$. Similarly, the heat diffusion flux is modelled assuming the Lewis number equals unity ($Le = \frac{Sc}{Pr} = 1.0$) as

$$q_j = -\rho \alpha_h \frac{\partial h}{\partial x_j} = -\frac{\mu}{Pr} \frac{\partial h}{\partial x_j}, \quad (2.9)$$

where α_h is the enthalpy diffusion coefficient, and Pr is the Prandtl number $Pr = \frac{\mu}{\rho \alpha_h}$. Note that the Soret effect and the Dufour effect are neglected. The thermodynamics properties are correlated by the equation of state for an ideal gas

$$p = \rho RT \quad (2.10)$$

and R is the gas constant of the mixture

$$R = \sum_{\alpha=1}^{N_s} Y_{\alpha} \frac{R_u}{MW_{\alpha}}, \quad (2.11)$$

where R_u is the universal gas constant, and MW_{α} is the molecular weight of species α .

2.2 Turbulent Flows

Turbulent flows are characterized by multiple length and time scales, which would need to be fully resolved by a direct numerical simulation (DNS). The smallest scale in turbulence is so-called the Kolmogorov length scale, η , and it can be shown to scale as [45]

$$\eta \approx Re^{-3/4} l, \quad (2.12)$$

where Re is the Reynolds number of the turbulence defined as $\frac{u' l}{\nu}$ with u' being the turbulent fluctuation velocity, and l is the integral length scale that is the size of the large energy containing eddy. The grid size of the simulation must be of the order of η or smaller to resolve all scales. Thus, assuming the three dimensional isotropic turbulence, the number of grid points necessary for the simulation is

$$N_{cell} \approx \left(\frac{L_{box}}{\eta} \right)^3 \approx \left(\frac{L_{box}}{l} \right)^3 Re^{9/4}, \quad (2.13)$$

where N_{cell} is the number of CFD cells, and L_{box} is the length of the domain. Since N_{cell} increases exponentially with Reynolds number, the required computational power increase exponentially, and it is too expensive to perform DNS of large scale devices such as aircraft engines and gas turbines.

The Reynolds-averaged NavierStokes (RANS) equations are introduced to obtain time-averaged solution of the turbulent flows at low computational costs. It solves the time-averaged equations, and all the fluctuations are modelled. RANS has been used successfully for a long period, especially for large-scale devices. However, RANS

might not be suited to simulate time transient processes and effects of localized flow structures.

Therefore, large eddy simulation (LES) has been proposed to capture unsteady physics at affordable computational cost and to make large scale simulations tractable. LES resolves turbulent eddies down to the size of the computational grid, and the small-scale motions are modeled assuming local isotropy. LES has been validated on various types of turbulent flows including reacting, two-phase flows. This study takes the advantages of LES to model turbulent flows.

2.2.1 Spatial Filtering

LES solves for spatially filtered governing equations. The filtered variable is defined as [148]

$$\bar{f}(\mathbf{x}) = \int_{\Omega} f(\mathbf{x})G(\mathbf{r})d\mathbf{r}, \quad (2.14)$$

where $G(\mathbf{r})$ is a filter kernel, and Ω indicates the control volume of the LES cell. A box function is used conventionally due to its simplicity, and a filter kernel is written as

$$G(\mathbf{r}) = \prod_{i=1}^3 G(r_i), \quad (2.15)$$

where

$$G(r_i) = \begin{cases} 1/\Delta_i & |r| < \Delta_i/2 \\ 0 & |r| > \Delta_i/2 \end{cases}, \quad (2.16)$$

and Δ_i indicates the LES filter size in i -th direction.

In variable density flows, it is useful to apply Favre-filtered (or density-weighted) averaging, where \tilde{f} denotes a Favre averaged quantity defined as

$$\tilde{f} = \frac{\overline{\rho f}}{\bar{\rho}}. \quad (2.17)$$

The advantage of Favre averaging is that it reduces the number of unclosed terms in the filtered equations (e.g. if only the spatial filtering is used, an unclosed term appears even in the continuity equation.)

2.2.2 Favre-Filtered Governing Equations

The Favre-filtered mass, momentum, species and enthalpy equations for two-phase flow are [14, 17]:

$$\frac{\partial \bar{\rho}}{\partial t} + \frac{\partial}{\partial x_j} (\bar{\rho} \widetilde{u_j}) = \bar{\rho}, \quad (2.18)$$

$$\frac{\partial}{\partial t} (\bar{\rho} \widetilde{u_i}) + \frac{\partial}{\partial x_j} (\bar{\rho} \widetilde{u_i u_j}) = -\frac{\partial \bar{p}}{\partial x_i} + \frac{\partial \bar{\tau}_{ij}}{\partial x_j} - \frac{\partial \tau_{ij}^{sgs}}{\partial x_j} + \bar{F}_i, \quad (2.19)$$

$$\frac{\partial}{\partial t} (\bar{\rho} \widetilde{Y_\alpha}) + \frac{\partial}{\partial x_j} (\bar{\rho} \widetilde{u_j Y_\alpha}) = -\frac{\partial \bar{J}_{\alpha,j}}{\partial x_j} - \frac{\partial J_{\alpha,j}^{sgs}}{\partial x_j} + \bar{\rho} \widetilde{\omega_\alpha} + \bar{\rho}_\alpha, \quad (2.20)$$

$$\frac{\partial}{\partial t} (\bar{\rho} \widetilde{h}) + \frac{\partial}{\partial x_j} (\bar{\rho} \widetilde{u_j h}) = -\frac{\partial \bar{q}_j}{\partial x_j} - \frac{\partial q_j^{sgs}}{\partial x_j} + \bar{Q}, \quad (2.21)$$

where τ_{ij}^{sgs} , $J_{\alpha,j}^{sgs}$ and q_j^{sgs} are the subgrid terms of the stress tensor, species diffusion and heat flux,

$$\tau_{ij}^{sgs} = \bar{\rho} (\widetilde{u_i u_j} - \widetilde{u_i} \widetilde{u_j}), \quad (2.22)$$

$$J_{\alpha,j}^{sgs} = \bar{\rho} (\widetilde{u_j Y_\alpha} - \widetilde{u_j} \widetilde{Y_\alpha}), \quad (2.23)$$

$$q_j^{sgs} = \bar{\rho} (\widetilde{u_j h} - \widetilde{u_j} \widetilde{h}). \quad (2.24)$$

The subgrid stress tensor is traditionally modelled by an eddy viscosity model as

$$\tau_{ij}^{sgs} = -2\mu_t \widetilde{S}_{ij}, \quad (2.25)$$

where μ_t is the turbulent viscosity. Then, the Smagorinsky model [161] is often used to provide the closure of μ_t as

$$\mu_t = \bar{\rho} (C_s \Delta)^2 \| \widetilde{S} \|, \quad (2.26)$$

where Δ is the filter size, $\| \widetilde{S} \|$ is the Frobenius norm of the resolved shear stress tensor $\sqrt{2\widetilde{S}_{ij}\widetilde{S}_{ij}}$, and C_s is the Smagorinsky constant. The coefficient C_s in Eqn. 2.26 is usually tuned between 0.05 and 0.2 based on the flow configurations. However, a single value of C_s is unsuitable to describe every region within a turbulent flow. It is also shown that the flow is very sensitive to the choice of C_s [14]. Therefore,

a dynamic model has been proposed to obtain locally optimized C_s to improve predictions [65, 106, 116], it is used in this study.

Similarly, closures for $J_{\alpha,j}^{sgs}$ and q_j^{sgs} are given as

$$J_{\alpha,j}^{sgs} = -\frac{\mu_t}{Sc_t} \frac{\partial \tilde{Y}_\alpha}{\partial x_j}, \quad (2.27)$$

$$q_j^{sgs} = -\frac{\mu_t}{Pr_t} \frac{\partial \tilde{h}}{\partial x_j}, \quad (2.28)$$

where Pr_t and Sc_t are the turbulent Prandtl and Schmidt number. In this study, Pr_t and Sc_t are set to be 0.7.

2.3 Mixing and Reacting Fields

2.3.1 Mixture Fraction

The mixture fraction, ξ is a useful concept to describe the degree of mixing between fuel and oxidizer in non-premixed flame analysis. The mixture fraction is defined based on the elemental mass fraction as

$$\xi = \frac{Z_i - Z_{i,2}}{Z_{i,1} - Z_{i,2}}, \quad (2.29)$$

where Z refers to the mass fraction of the i -th element, and subscripts 1 and 2 indicate fuel and oxidizer conditions, respectively. Since the mixture fraction is based on elements, the transport equation of the mixture fraction does not contain a chemical source term,

$$\frac{\partial}{\partial t}(\rho\xi) + \frac{\partial}{\partial x_j}(\rho u_j \xi) = -\frac{\partial J_{\xi,j}}{\partial x_j} + \dot{\rho}_\xi, \quad (2.30)$$

with $\dot{\rho}_\xi$ being the spray source term. In LES, the Favre-filtered transport equation is given as

$$\frac{\partial}{\partial t}(\bar{\rho}\tilde{\xi}) + \frac{\partial}{\partial x_j}(\bar{\rho}\tilde{u}_j\tilde{\xi}) = -\frac{\partial \overline{J_{\xi,j}}}{\partial x_j} - \frac{\partial J_{\xi,j}^{sgs}}{\partial x_j} + \bar{\rho}_\xi. \quad (2.31)$$

The advantage of the mixture fraction is that the transport equation can be easily solved in reacting flows since it is an inert (no chemical source term) quantity. Also, it is used as a sample space in a manifold method to model turbulent combustion (see Sec. 2.6.2). The definition of the mixture fraction in two-phase flows is discussed in later sections (in Sec. 7.1.2).

2.3.2 Progress Variable

Another scalar used to characterize combustion is the progress variable, c , that indicates the degree of completion of a reaction for a specific mixture. The progress variable can be used to describe premixed flames and variable definitions of the progress variable can be used. c is often conventionally chosen as a summation of the major species as

$$c = Y_{CO_2} + Y_{H_2O} + Y_{CO} + Y_{H_2}, \quad (2.32)$$

or additional weighting by molecular weight is modelled:

$$c = \frac{Y_{CO_2}}{MW_{CO_2}} + \frac{Y_{H_2O}}{MW_{H_2O}} + \frac{Y_{CO}}{MW_{CO}} + \frac{Y_{H_2}}{MW_{H_2}}. \quad (2.33)$$

Also, a progress variable can be defined based on temperature or sensible enthalpy

$$c = \frac{T - T_{min}}{T_{max} - T_{min}}, \quad (2.34)$$

$$c = \frac{h_s - h_{s,min}}{h_{s,max} - h_{s,min}}, \quad (2.35)$$

where *min* and *max* indicate the solution at equilibrium and cold mixing, respectively, and h_s is sensible enthalpy. Further definitions of the progress variable using various combinations of weighting factors can be found in the literature [133].

The transport equation of the progress variable reads

$$\frac{\partial}{\partial t}(\rho c) + \frac{\partial}{\partial x_j}(\rho u_j c) = -\frac{\partial J_{c,j}}{\partial x_j} + \rho \omega_c + \dot{\rho}_c, \quad (2.36)$$

where $\dot{\rho}_c$ is the spray source term of the progress variable, which depends on the definition of c . Then, the Favre filtered form is

$$\frac{\partial}{\partial t}(\bar{\rho}\tilde{c}) + \frac{\partial}{\partial x_j}(\bar{\rho}\tilde{u}_j\tilde{c}) = -\frac{\partial \overline{J_{c,j}}}{\partial x_j} - \frac{\partial J_{c,j}^{sgs}}{\partial x_j} + \bar{\rho}\tilde{\omega}_c + \bar{\rho}\dot{\rho}_c. \quad (2.37)$$

It is not straightforward to solve Eqn. 2.37 due to the presence of the filtered reaction rates $\tilde{\omega}_c$. The modelling of $\tilde{\omega}_c$ is one of the biggest challenges in turbulent combustion and briefly reviewed in Sec. 2.6. The progress variable space is also often chosen as a sample space in a manifold method especially for premixed and partially premixed flames.

2.4 Scalar Dissipation

Scalar dissipation is an important parameter to describe turbulent flames, since it is closely correlated with the chemical reaction rate [11]. In LES, the filtered scalar dissipation rate is given as

$$\tilde{N} = D \left(\overline{\frac{\partial \xi}{\partial x_i} \frac{\partial \xi}{\partial x_i}} \right) = \tilde{N}_{res} + \tilde{N}_{sgs}, \quad (2.38)$$

where \tilde{N}_{res} and \tilde{N}_{sgs} are a resolved and subgrid scale scalar dissipation rate. \tilde{N}_{res} is modelled by using the filtered quantities

$$\tilde{N}_{res} = D \left(\frac{\partial \tilde{\xi}}{\partial x_i} \frac{\partial \tilde{\xi}}{\partial x_i} \right). \quad (2.39)$$

However, the closure of \tilde{N}_{sgs} requires some considerations. One methodology is to solve the transport equation of the mixture fraction variance, $\overline{\xi'^2}$, with the presence of the spray source term given by

$$\begin{aligned} \frac{\partial}{\partial t}(\overline{\rho\xi''^2}) + \frac{\partial}{\partial x_j}(\overline{\rho u_j \xi''^2}) = & \\ \frac{\partial}{\partial x_j} \left[\left(\overline{\rho} D + \frac{\mu_t}{Sc_t} \right) \frac{\partial \overline{\xi''^2}}{\partial x_j} \right] - \underbrace{2\overline{\rho} \widetilde{N}_{sgs}}_{\text{dissipation}} + \underbrace{2 \frac{\mu_t}{Sc_t} \left(\frac{\partial \widetilde{\xi}}{\partial x_j} \right)^2}_{\text{production}} + \underbrace{\sigma_s}_{\text{spray source term}}, & \end{aligned} \quad (2.40)$$

and σ_s is the source term associated with the evaporation process such as

$$\sigma_s = 2\overline{\rho} (\widetilde{\xi}\widetilde{\Pi} - \widetilde{\xi}\widetilde{\Pi}) + \overline{\rho} (\widetilde{\xi}^2\widetilde{\Pi} - \widetilde{\xi}^2\widetilde{\Pi}), \quad (2.41)$$

where Π is the volumetric expansion rate due to spray evaporation.

In LES, it is common to assume local equilibrium, which is to balance the production and dissipation terms, so

$$2\overline{\rho} \widetilde{N}_{sgs} = 2 \frac{\mu_t}{Sc_t} \left(\frac{\partial \widetilde{\xi}}{\partial x_j} \right)^2 + \sigma_s. \quad (2.42)$$

If there is no spray source term (single-phase flow), it follows from Eqn. 2.42 that

$$\widetilde{N}_{sgs} = \frac{\nu_t}{Sc_t} \left(\frac{\partial \widetilde{\xi}}{\partial x_j} \right)^2, \quad (2.43)$$

where $Sc_t = 0.7$. Also, there are a couple of dynamic models to compute the coefficient [143, 88].

Under two-phase flow conditions with evaporating droplets, extra considerations are necessary to treat the spray source term. Pera et al. [138] found a significant contribution of the second RHS-term of Eqn. 2.42 to the balance of N_{sgs} for all their investigated cases and suggested a dynamic modelling procedure. This modelling is not attempted here, but N_{sgs} is modelled as

$$\widetilde{N}_{sgs} = C_N \frac{\nu_t}{Sc_t} \left(\frac{\partial \widetilde{\xi}}{\partial x_j} \frac{\partial \widetilde{\xi}}{\partial x_j} \right), \quad (2.44)$$

where C_N is a model coefficient and set to 5.0. The DNS data from [138] justify

this *ad hoc* correction by this model coefficient to account for gradient steepening effects due to evaporation. Another argument for large C_N within spray flames is discussed by Hasse [74]. Considering a transport equation with a source term such as

$$\frac{\partial}{\partial t}(\rho\xi) + \frac{\partial}{\partial x_j}(\rho u_j \xi) = \frac{\partial}{\partial x_j} \left(\rho D \frac{\partial \xi}{\partial x_j} \right) + C\xi, \quad (2.45)$$

where the last term on the RHS is the source term assumed to be a linear function of ξ with C being a constant for the source term. Then, Hasse [74] has shown that the time scale of the scalar dissipation is the function of the the source term as

$$C_N = \frac{3C\tau}{1 - \exp(-3C\tau)}, \quad (2.46)$$

where τ is the eddy turnover time scale. Eqn. 2.46 indicates that a source term (positive C) in the mean transport equation would increase C_N .

2.5 Chemical Reaction

The combustion process usually involves a number of elementary reactions. A chemical reaction can generally be represented as



where N_s is the total number of species (including both reactants and products), M_i represents the i -th molecule, and ν'_i and ν''_i are the stoichiometric coefficients of reactants and products, respectively. Then, the reaction rate of the molecule M_i becomes

$$\frac{dC_{M_i}}{dt} = (\nu''_i - \nu'_i) k \prod_{i=1}^{N_s} (C_{M_i})^{\nu'_i}, \quad (2.48)$$

where C_{M_i} represents the concentration of M_i , and k is the reaction rate constant modelled by the Arrhenius law as

$$k = AT^b \exp\left(-\frac{E_a}{R_u T}\right), \quad (2.49)$$

where A is the pre-exponential factor, b is the temperature exponent, and E_a is the activation energy. Reaction mechanisms specifying these values of can be found elsewhere [171, 72].

Early DNS of reacting flows were only tractable with simple single-step (global) chemistry [181]. Recently, DNS with simple chemistry became possible with recent computer developments [30]. However, the combustion of a complex fuel involves a large number of species and elementary reactions, and it is computationally too expensive to solve all the reactions [104, 141]. For example, a recent detailed chemistry mechanism for a biofuel involves 3012 species and 8820 elementary reactions [76]. Therefore, reduced mechanisms are often used to minimize the computational requirements. The reviews of recent developments of a reduced mechanism can be found elsewhere [108, 55].

2.6 Combustion Modelling

The main challenge of turbulent combustion modelling is to accurately describe subgrid scale physics. Assuming the Arrhenius law, the reaction rates of species α is a function of mass fraction of species and temperature such

$$\omega_\alpha = f \{Y_1, Y_2, \dots, Y_N, T\}. \quad (2.50)$$

However, in LES and RANS, the reactive scalar fields are represented by filtered quantities, and exact local solutions of Y and T are not available. Therefore, it is not straightforward to obtain filtered reaction rates since the correlation is quite non-linear, as

$$\tilde{\omega}_\alpha = \{Y_1, \widetilde{Y_2, \dots, Y_{N_s}}, T\} \neq f \{\tilde{Y}_1, \tilde{Y}_2, \dots, \tilde{Y}_{N_s}, \tilde{T}\}. \quad (2.51)$$

Here, the most common turbulent combustion modelling approaches are briefly reviewed. Note that various review papers [149, 141, 104, 145, 13, 181] and books [55, 28, 140, 146] about turbulent combustion modelling are available.

2.6.1 Algebraic Models

2.6.1.1 Eddy Break Up Model

One of the first successful turbulent combustion models is the Eddy Break Up (EBU) Model. EBU assumes that the reaction occurs faster than the rate of mixing of reacting species, so that the reaction rate is considered to be same as the rate of scalar dissipation. The filtered reaction rates can then be represented as [140]

$$\tilde{\omega}_P = C_{EBU} \frac{\epsilon}{k} \sqrt{\widetilde{Y_P''^2}}, \quad (2.52)$$

where the subscript P indicates a product species, C_{EBU} is the EBU constant, $\widetilde{Y_P''^2}$ the variance of the product mass fraction. Eqn. 2.52 can be further simplified to [28]

$$\tilde{\omega}_P = C_{EBU} \frac{\epsilon}{k} \widetilde{Y}_P (1 - \widetilde{Y}_P), \quad (2.53)$$

by modelling $\sqrt{\widetilde{Y_P''^2}} = \widetilde{Y}_P (1 - \widetilde{Y}_P)$ assuming there is no intermediate combustion state.

2.6.1.2 Eddy Dissipation Model

Later, the Eddy Dissipation Model (EDM) was developed by extending the EBU concept considering all fuel, oxidizer and products. By EDM, the mean reaction rate is written as [28]

$$\tilde{\omega}_F = A \frac{\epsilon}{k} \min \left(\widetilde{Y}_F, \frac{\widetilde{Y}_{Ox}}{S}, B \frac{\widetilde{Y}_P}{1 + S} \right), \quad (2.54)$$

where the subscripts Ox and F refer to oxidizer and fuel, S is the oxygen-fuel stoichiometric mass ratio, and A and B are model parameters. EBU and EDM are still used in many CFD software packages due to their simplicity, but it is worth noting that they can be only used for infinitely fast chemistry unless the chemical time scales are explicitly taken into account [28]. Note that the terminology of EDM varies in the literature and there are also EDM variants which account for

small-scale effects of chemical kinetics.

2.6.2 Low Dimensional Manifold Approaches

Combustion usually is a function of many parameters, but the system can be simplified by assuming that selected controlling parameters are dominant. Once properties are characterized by a function of the selected sample spaces variables, filtered quantities can be obtained by integration with a subgrid filtered density function (FDF). A common choice of a sample space for non-premixed flame analysis is the mixture fraction, ξ , and a filtered quantity can be calculate as

$$\tilde{f} = \int_0^1 f_\eta P(\eta) d\eta, \quad (2.55)$$

where f_η is a scalar, f , conditioned on the sample space of mixture fraction η . It is also possible to have multiple sample spaces (e.g. mixture fraction and progress variable) to account for more complex flames such as a partially premixed flame and stratified flame. Here, a brief review of the low dimensional manifold approaches is given.

2.6.2.1 The Burke-Schumann and Equilibrium Solutions

The Burke-Schumann solution assumes one step irreversible fast chemistry and provides piece-wise linear profiles of species and temperature in mixture fraction space. Also, the profile can be improved by assuming the chemical equilibrium that is fast but reversible. If the chemical time scales of the major reactions were faster than the flow time scales, the equilibrium solution can approximate flame conditions. Knowing the limitation of the assumption, equilibrium chemistry can be used in LES and results in an adequate agreement with experimental data [89].

2.6.2.2 Flamelet Model

The flamelet model assumes a thin flame and characterizes flame properties within the reaction zone. Transforming the spatial coordinate perpendicular to the flame

surface to the mixture fraction space, the unsteady laminar flamelet equation can be derived as [140]

$$\frac{\partial Y_\alpha}{\partial t} = N \frac{\partial^2 Y_\alpha}{\partial \eta^2} + \omega_\alpha, \quad (2.56)$$

where N is the scalar dissipation rate. To adapt the flamelet approach to the LES framework, it is common to solve steady or unsteady flamelet equations and construct a chemical table (usually in low dimensions). Since a turbulent flame can be considered as an ensemble of laminar flamelets, integration of the chemical table with a joint-FDF yields the filtered quantities. For example, for the non-premixed flow, the chemical table can be a function of ξ and N , and the filtered quantities can be found as

$$\tilde{f} = \int_0^1 \int_0^\infty P(\eta, N) f(\eta, N) dN d\eta. \quad (2.57)$$

The selection of the chemical table parameters can be optimized for the respective flame configurations.

2.6.2.3 Conditional Moment Closure

The conditional moment closure (CMC) solves a transport equation for the conditional moments. The CMC equation was derived for single phase reacting flow assuming unity Lewis number and high Reynolds number as [96]

$$\frac{\partial}{\partial t} Q_\alpha + U_\eta \cdot \nabla Q_\alpha + \frac{\nabla \cdot (\bar{\rho}_\eta \tilde{P}_\eta \langle U'' Y_\alpha'' | \eta \rangle)}{\bar{\rho}_\eta \tilde{P}_\eta} = \tilde{\omega}_{\eta, \alpha} + N_\eta \frac{\partial^2 Q_\alpha}{\partial \eta^2}, \quad (2.58)$$

where Q_α is the conditional moment of species α , U'' and Y_α'' are the conditional fluctuation terms related to the instantaneous velocity and species mass fractions by $U = U_\eta + U''$ and $Y_\alpha = Q_\alpha + Y_\alpha''$, the subscript η indicates the conditionally averaged properties. Modelling the fluctuation term $\langle U'' Y_\alpha'' | \eta \rangle$ by the gradient diffusion model as $\langle U'' Y_\alpha'' | \eta \rangle = -D_t \nabla Q_\alpha$, Eqn. 2.58 can be re-written in its classical conservative

form as

$$\begin{aligned} \frac{\partial}{\partial t} Q_\alpha &+ \frac{1}{\bar{\rho}_\eta \tilde{P}_\eta} \nabla \cdot [\bar{\rho}_\eta \tilde{P}_\eta (U_\eta Q_\alpha - D_{t,\eta} \nabla Q_\alpha)] \\ &= \tilde{\omega}_{\eta,\alpha} + N_\eta \frac{\partial^2 Q_\alpha}{\partial \eta^2} + \frac{Q_\alpha}{\bar{\rho}_\eta \tilde{P}_\eta} \nabla \cdot (\rho_\eta \tilde{P}_\eta U_\eta). \end{aligned} \quad (2.59)$$

As CMC is in the focus of the present thesis, further details and formulations for two-phase flames are discussed in Chapter 4 and the later chapters.

2.6.2.4 Conditional Source-Term Estimation

Conditional Source-term Estimation (CSE) takes a unique approach to construct a manifold. Flamelet and CMC provide conditional moments and obtain filtered quantities as shown in Eqn. 2.55. However, CSE solves for unconditional scalar transport equations (e.g. Eqns. 2.20 and 2.21) and inversely reconstructs conditional moments to obtain the conditional chemical reaction rates (see Chapter 4) [167]. Inversion methods are discussed in detail elsewhere [26, 103]. In addition, a brief history and introduction of CSE is described in [25].

2.6.3 Stochastic Approaches

Another type of the turbulent combustion modelling is the stochastic approach. An advantage of the stochastic approach is that it is theoretically independent of the flame configuration such as premixed, non-premixed or partially premixed flame, whereas a low dimensional manifold approach must consider the type of flame to choose appropriate reference spaces. Here, brief reviews of stochastic approaches are given.

2.6.3.1 PDF Method

In the most general case, the PDF method solves for the joint-PDF of the velocity and scalars. Since it is computationally very expensive to solve the high-dimensional PDF transport equation, an equivalent set of Langevin equations for notional (stochastic) particles are solved to construct scalar statistics. Because the notional particle represents instantaneous local properties, reaction rates can be accurately

computed. Similarly, the Eulerian stochastic field method solves sets of Eulerian stochastic fields instead of Lagrangian notional particles. A number of stochastic Eulerian transport equations are solved and used to construct the subgrid PDF [86]. Extensive reviews of the PDF method can be found elsewhere [147, 75].

2.6.3.2 Multiple Mapping Conditioning

Multiple Mapping Conditioning (MMC) is a new approach first developed by Klimenko and Pope [97] that claims to combine advantages of CMC and PDF methods. MMC reduces the dimensions of the space by considering *major* and *minor* spaces with the *minor* species fluctuating jointly with the major species. Thus, the similarity of CMC and MMC is to describe *minor* species by *major* species, as CMC describes all reactive species by the mixture fraction. At the same time, MMC can have a higher number of dimensions similarly to PDF methods. In its stochastic form, the MMC equations are solved by notional particles [185]. A new mixing model based on a mapping concept has been also proposed [41]. Note that it is also possible to have a deterministic solution of MMC, but that is inefficient if more than one major species is chosen. In this case, MMC equations can be solved in Eulerian space as conventionally done in the CMC framework [183, 184, 49].

2.6.3.3 Linear Eddy Model / One Dimensional Turbulence

The linear eddy model (LEM) describes a turbulent mixing in one-dimensional space. It assumes that the mixing is fully resolved along a selected alignment of a turbulent mixing, and the mixing process is modelled by remapping the 1D profile stochastically. Then, the diffusion and reaction of the re-mapped profiles are computed by solving one dimensional unsteady species and energy transport equations. Because each 1D cell is small and fully resolved, the reaction rate can be obtained by the first order model. LEM has been successfully combined with LES [31]. Similarly, One Dimensional Turbulence (ODT) performs the 1D mixing on velocity fields that allows a coupling of momentum and reactive scalars [54].

2.7 Numerical Approach

The governing equations are solved in Cartesian coordinates by using the in-house code BOFFIN, that has been used in various simulations of turbulent flows [23, 86, 85]. A finite volume method (FVM) is used to discretize the set of equations. The mass and the momentum equations are discretized by a central differencing scheme with a SIMPLE-type predictor-corrector procedure with pressure smoothing, and cell quantities are stored on the cell centers (co-located). Additionally, the scalar transport equations are solved by a total variation diminishing (TVD) approach to avoid over- and undershoots of the solution. Since the implementation of BOFFIN has been discussed in various previous papers and theses, the reader is referred to the past work [22, 50, 189] and the manual [83].

Chapter 3

Liquid Phase Formulation and Modelling

The scale of liquid fuel droplets occurring in combustion devices tends to be very small to enhance evaporation, mixing and combustion. Therefore, it is not computationally feasible to fully resolve every detail of particle behavior. There are multiple methods to compute the dynamics of a multiphase flow depending on aims and flow conditions, and governing equations of the liquid phase depend on the model. In this study, a Lagrangian scheme is applied due to its flexibility to obtain detailed information of individual particles. This chapter discusses turbulent-spray-reaction interactions in Sec. 3.1, reviews modelling approaches in Sec. 3.2, and presents the Lagrangian scheme formulations in Sec. 3.3.

3.1 Backgrounds of Two-Phase Flow Phenomena

The behavior of turbulent flames and droplets are correlated to each other and cannot be neglected. The presence of the turbulence influences the particle dispersion profiles and causes so-called preferential concentration. Also, the particle within turbulent flow can change the turbulent flow structures. In addition, flame profiles can be characterized by fuel droplet distributions. Here, some aspects of particle-turbulence and particle-combustion interactions are reviewed. There are various

summary papers available [44, 6, 7, 124].

3.1.1 Preferential Concentration

Dispersion of spray in a turbulent flow results in a high concentration of droplets where the strain rate is high and the vorticity is low. Such a profile is denoted as “preferential concentration”, and it becomes apparent when the Stokes number, St , is of order of unity, which is defined as the ratio of the particle response time to the fluid time scales. Figure 3.1 shows an example of preferential particle concentration in isotropic homogeneous turbulence. When the particle time scale is small (e.g. $St = 0.05$), the particle distribution seems relatively uniform. However, as St increases, non-homogeneous structures become apparent within the turbulence field.

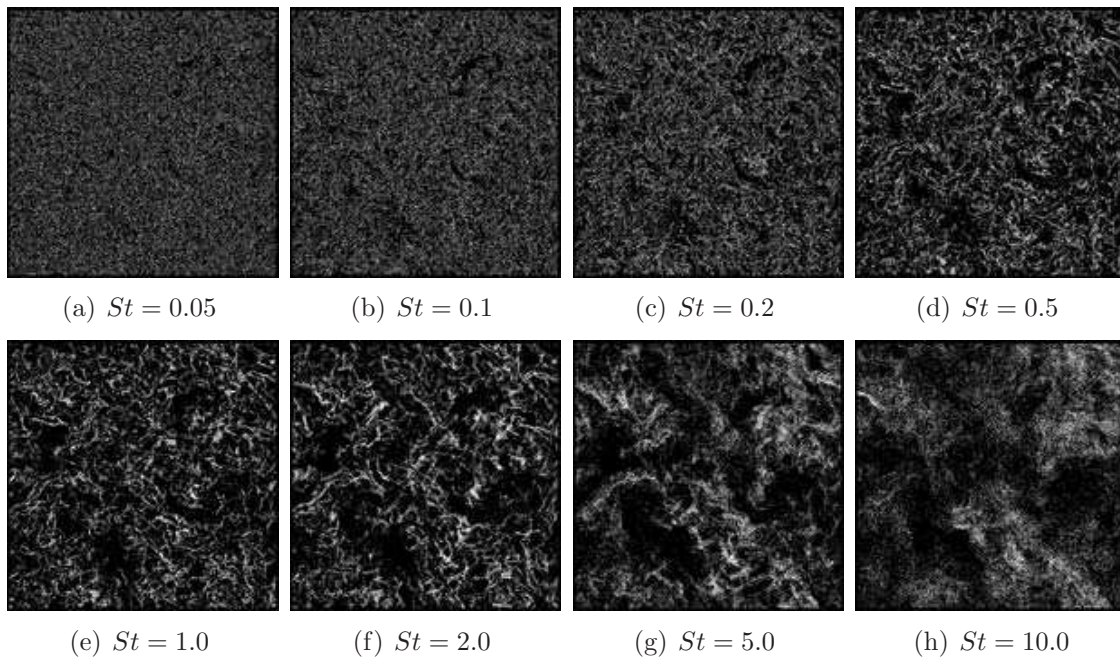


Figure 3.1: Distributions of particles within isotropic homogeneous turbulence with different St (Yoshimoto and Goto [192]).

3.1.2 Turbulence Modulation

The presence of droplets may also affect turbulence characteristics. Due to two-way coupling of momentum between gas-phase and particles, turbulence intensity can be

attenuated or enhanced depending on the Stokes number [44]. It is also known that particles introduces small scale motions that influences turbulence spectra [73, 6].

3.1.3 Group Combustion

Flame structures of fuel droplet clouds can vary depending on features of clusters. Chiu and co-workers [35, 34] considered a spherical droplet cloud in a hot oxidizing environment and proposed a group combustion model, that determines how droplet clouds burn based on droplet spacing and the evaporation process. Here, the group combustion number, G , is introduced as [35]

$$G = 3 \left(1 + 0.276 Re^{1/2} Sc_{1/3} \right) Le N \left(\frac{r_l}{R_b} \right), \quad (3.1)$$

where R_b is the radius of droplet clouds, N is the total number of droplets in the clouds, r_l is the radius of the droplet, and G describes the ratio of the evaporation rate to the fuel diffusion rate. Also, the non-dimensional separation, S , is defined as [34],

$$S = \frac{0.05}{1 + 0.276 Re^{1/2} Sc^{1/3}}. \quad (3.2)$$

Then, four combustion regimes can be defined (Fig. 3.2) as: 1) single droplet combustion, 2) internal group combustion, 3) external group combustion and 4) external sheath combustion. The single droplet combustion causes the individual droplets in the cloud to burn independently, and an envelope flame is seen around each droplet. The internal group combustion regime is characterized by a combustion zone along the outer shell where individual droplets burn, and a pre-heating zone at the center of the cloud where only pre-evaporation caused by thermal diffusion occurs. In the external group combustion regime, there are no more droplets burning individually, but all the droplets evaporate and emit gaseous fuel, and the flame is located only outside the droplet cloud. The external sheath combustion regime occurs around very dense particles clouds and in this regime spray droplets evaporate only at the sheath, while the inner droplets are shielded and do not even evaporate.

While the group combustion diagram is instructive to distinguish the various possible spray combustion modes, it is very complex [33] to apply to the prediction of spray flames in engineering applications due to the prevalent conditions (e.g. polydispersion, non-uniform particle distribution, random cluster shape, etc.). Thus, the group combustion model is rather applied as a post-processing analysis of spray flames. Recent studies have shown group combustion both experimentally [163, 155] and numerically [128, 193, 93]. Also, the group combustion model has been analyzed by percolation theory, which describes the propagation of a flame between the droplets [178].

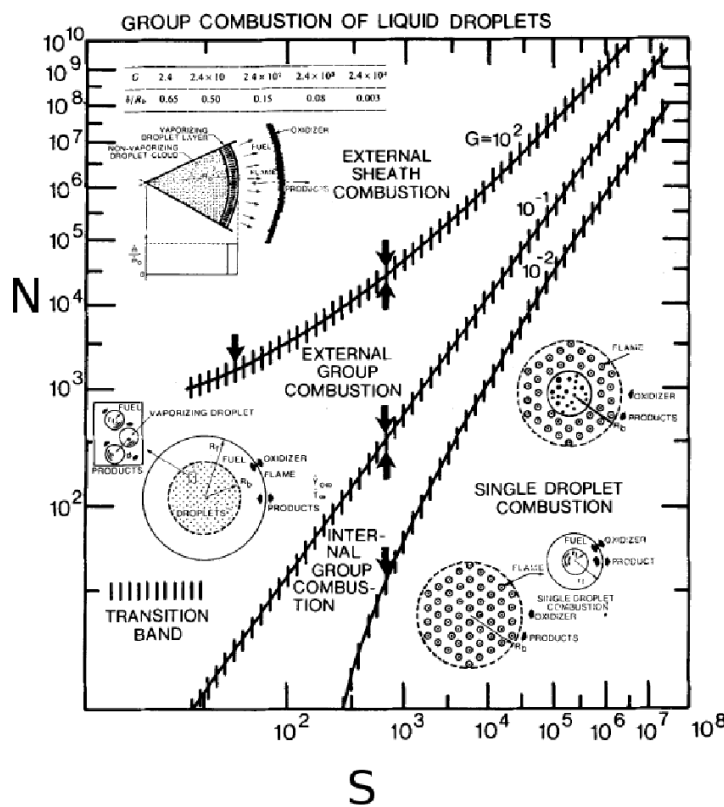


Figure 3.2: Group combustion regimes (Chiu et al. [34]).

3.2 Review of Two-Phase Flow Modelling Approaches

There are different approaches to simulate turbulent spray flames depending on the physical scale sizes to resolve. This section provides a brief summary of the main simulation approaches for multiphase flows. More detailed reviews can be found elsewhere [6, 7, 82] as well.

3.2.1 Fully Resolved Droplet

The most precise approach is to resolve all physical scales down to the droplet size, boundary layer and flame thickness, which allows to extract detailed statistics and to validate empirical models (e.g. for evaporation). Imaoka and Sirignano [81, 80] have studied quasi-steady combustion of droplet arrays. Stauch and Maas [166] have analyzed the autoignition of a single droplet under laminar convection. Zoby et al. [194, 193] used a level set method to track the liquid-gas interface of single droplets and droplet arrays and analyzed mixing and combustion statistics. Also, Duret et al. [52] have performed a parametric study of mixing statistics with different gas-liquid volume ratios. Similarly, Shinjo and Umemura [156] have simulated the atomization of liquid jets by resolving the liquid-gas interface. However, a drawback of the approach is the computational cost. It is not yet possible to fully resolve a large number of particles.

3.2.2 Lagrangian Point-Particle Approach

The Lagrangian scheme tracks the properties of each particle, and detailed information of particle clouds can be obtained (e.g. preferential dispersion). Also, it is more flexible than an Eulerian scheme since assumptions such as equilibrium or monodispersity are not necessary, and properties of particles do not need to be consistent in the flow fields. Note that advanced Eulerian models without such assumptions exist, but the formulation tends to be very complex. Also, a subgrid scale turbulence can

be modelled stochastically in the Lagrangian scheme. Therefore, the Lagrangian scheme is used for the present study. This section describes various Lagrangian particle approaches, and details of the Lagrangian scheme used in this work are given in Sec. 3.3.

3.2.2.1 DNS-Lagrangian Approach

DNS combined with a Lagrangian approach resolves all scales of the turbulent flow, but as the droplets may be considerably smaller than the Kolmogorov scale, they are modelled as point particles. Fessler et al. [56] have performed DNS of dispersing particles and the development of preferential particle concentrations by different Stokes numbers. Later, DNS of evaporating fuel droplets have been performed to examine the mixing of the evaporated fuel [105]. Recent carrier-phase DNS study the combustion of point particles under various conditions [153, 151, 187, 109, 19]. Since the turbulent flow is fully resolved, no stochastic modifications to the dispersion and evaporation models are required.

3.2.2.2 LES-Lagrangian Approach

LES with point particles are used very often to simulate engineering devices [117, 123, 85]. However, the importance of the stochastic dispersion terms in the LES framework is not fully validated yet. Since LES resolves the dynamics of the large scale motions and a large portion of the turbulent kinetic energy, subgrid effects can be relatively small. At the same time, Jones and his coworkers [16, 17, 84, 85] have analyzed the influence of the stochastic dispersion terms and found that the addition of the stochastic terms influences the flow field. Pozorski and Apte [150] have compared DNS and post-filtered DNS with typical LES subgrid terms. They reported that when the subgrid kinetic energy is chosen to recover the kinetic energy in LES, the subgrid stochastic term is too large to destroy small structures of preferential concentration, since the model is based on one-point statistics only. Thus, by including a stochastic model the prediction of particle dispersion statistics (mean and RMS) can improve, but this does not necessarily mean that the stochastic

model can reproduce the instantaneous flow field correctly.

3.2.2.3 RANS-Lagrangian Approach

In RANS, stochastic dispersion and evaporation terms are critical, since all turbulent fluctuations remain unresolved. Thus, several stochastic dispersion models have been proposed and tested in non-reacting [107, 18] and reacting flows [47, 46]. Since stochastic models based on the Langevin equations are usually based on one-point statistics, preferential droplet concentrations (see Sec. 3.1.1) cannot be captured. Another approach is to solve a Fokker-Plank equation which represents the Eulerian formulation of the Langevin equation. With the Fokker-Plank equation, the PDF can be solved and higher moments can be modelled [148, 57].

3.2.3 Eulerian Approach

The Eulerian scheme treats the liquid phase as a continuous fluid medium and describes particle dispersion by solving additional scalar transport equations. Therefore, the approach is suited to handle a large number of particles within the system especially when the particles are small. However, it can be computationally expensive when polydisperse systems are considered, since transport equations for different droplet size ranges must be solved [59]. Also, closures of the subgrid terms in the particle transport equations are not fully established yet, unless an equilibrium assumption is used [157, 58]. If the particle response time is very small, the two-phase fluid might be treated as a single phase flow (the dusty-flow assumption), the properties of which are adjusted to account for the droplet phase [6, 7]. Ukai et al. [173] have shown that the dusty-flow assumption works well if the Stokes number is very small.

3.3 Lagrangian Approach

3.3.1 Particle Dispersion

The governing equations of the particle trajectories used in this work are given as [17]

$$d\mathbf{x}_p = \mathbf{v}_p dt, \quad (3.3)$$

$$d\mathbf{v}_p = \tau_p^{-1}(\mathbf{u} - \mathbf{v}_p)dt + \sqrt{C_0 \frac{k_{sgs}}{\tau_t}} d\mathbf{W}, \quad (3.4)$$

where \mathbf{x}_p is the position of the particle, \mathbf{u} is the local velocity of the gas at the location of the particle, \mathbf{v}_p is the velocity of the particle, τ_p is the particle response time, C_0 is a model coefficient, k_{sgs} is the subgrid kinetic energy, τ_t is the subgrid flow time scale, and $d\mathbf{W}$ is the increment of a Wiener process. The general form of Eqn. 3.4 contains other terms on the right hand side to include the effect of pressure gradient, the Basset term, the Saffman lift and the Magnus lift [114]. For this dilute study, all these effects are neglected as a first approximation. The particle response time scale τ_p is defined as

$$\tau_p^{-1} = \frac{3}{8} \frac{\rho_g C_D}{\rho_p r_p} |\mathbf{u} - \mathbf{v}_p|, \quad (3.5)$$

where r_p is the particle radius, ρ_g is the gas density, ρ_p is the density of the particle, and C_D is the drag coefficient. The drag coefficient is generally expressed as a function of the particle Reynolds number, $Re_d = \frac{2r_p \rho |\mathbf{u} - \mathbf{v}_p|}{\mu}$, where μ is the viscosity of the gas. Assuming spherical particles, the drag coefficient, C_D , is obtained from empirical relations [43] as

$$C_D = \begin{cases} \frac{24}{Re_d} \left(1 + \frac{1}{6} Re_d^{2/3}\right) & Re_d < 1000 \\ 0.424 & Re_d > 1000 \end{cases}. \quad (3.6)$$

The second term on the right hand side of Eqn. 3.4 is associated with the subgrid

fluctuation in LES. Many LES studies in the past have neglected the small scale fluctuations. However, recent studies have reported the importance of the subgrid fluctuation terms in LES [16, 17, 150]. Here, the effect of subgrid kinetic energy is described by a Wiener process. The subgrid flow time scale is given as

$$\tau_t = \frac{\tau_p^{2\alpha}}{\left(\frac{\Delta}{\sqrt{k_{sgs}}}\right)^{2\alpha-1}}, \quad (3.7)$$

where $\alpha = 0.8$ is recommended [16]. This study uses $C_0 = 1.0$ as originally suggested [17], but the selection of C_0 is still under debate. Pasmazoglou et al. [139] have compared the effects of different choices of C_0 , and $C_0 = 1$ is found to agree with the DNS solution. Also, the same authors have also developed a dynamic model to locally determine C_0 based on the Germano model [65].

3.3.2 Particle Temperature and Size

While particle dispersion models are relatively well established, droplet evaporation models are still under discussion. Abramzon and Sirignano [2] have proposed an evaporation model which is commonly used in the spray community [122, 17]. The temperature and radius of the particles are computed as [122, 17].

$$dT_p = \left(\frac{Nu C_{p_g}}{3 Pr_g C_{p_l}} \left[\frac{T_g - T_p}{\tau_p} \right] + \frac{h_{fg} \dot{m}_p}{C_{p_l} m_p} \right) dt, \quad (3.8)$$

$$dm_p = - \frac{Sh + Sh^{sgs}}{3 Sc_g} \frac{m_p}{\tau_p} H_M dt, \quad (3.9)$$

where T_p is the particle temperature, Nu is Nusselt number, C_{p_g} and C_{p_l} are the specific heat of gas and liquid respectively, Pr_g is the gas phase Prandtl number, h_{fg} is the latent heat of evaporation, m_p is the particle mass, \dot{m}_p is the rate of evaporation and Sc_g is the gas phase Schmidt number, Sh is the Sherwood number, Sh^{sgs} is the subgrid Sherwood number, and H_M is the convective correction to the evaporation rate. Sh^{sgs} is modelled to account for the turbulent fluctuations and a

closure is proposed [17] as

$$Sh^{sgs} dt = C_V Sc_G^{1/3} \left(\rho_g \frac{k_{sgs}^{1/2} D}{\mu_g} \right)^{1/2} |dW_t|^{1/2} \tau_p^{3/4}, \quad (3.10)$$

where C_V is a model coefficient, and this study uses $C_V = 1.0$. Jones et al. [84] have compared the effects of different choices of C_V , and $C_V = 1.0$ is found to agree with experimental results. Derivations of the stochastic terms can also be found in [14, 17]. There are various empirical methods to approximate Nu , Sh and H_M , and the present study uses correlations proposed by Abramzon and Sirignano [2, 158] that account for a Falkner-Skan boundary layer solution around the droplets. The coefficients are given as

$$Nu = 2 + \frac{Nu^* - 2}{F_T}, \quad (3.11)$$

$$Sh = 2 + \frac{Sh^* - 2}{F_M}, \quad (3.12)$$

where

$$Nu^* = 2 + 0.552 Re_d^{1/2} Pr_g^{1/3}, \quad (3.13)$$

$$Sh^* = 2 + 0.552 Re_d^{1/2} Sc_g^{1/3}, \quad (3.14)$$

with the following correlations

$$F_T = (1 + B_T)^{0.7} \frac{\ln(1 + B_T)}{B_T}, \quad (3.15)$$

$$F_M = (1 + B_M)^{0.7} \frac{\ln(1 + B_M)}{B_M}, \quad (3.16)$$

where B_T and B_M are the Spalding number for heat and mass transfer, respectively, and defined as

$$B_T = (T_g - T_d) \frac{Cp_{vap}}{h_{fg}}, \quad (3.17)$$

$$B_M = \frac{Y_s - Y_g}{1 - Y_s}, \quad (3.18)$$

where Cp_{vap} is the specific heat of the vapour, Y_s and Y_g are the mass fractions of

the vapour at the interface and in the gas phase.

Y_s can be found by the Clausius-Clapeyron equation assuming liquid-vapour equilibrium. It obtains the mole fraction of vapour at the surface, X_s , as a function of the vapour pressure P_G such as

$$X_s = \frac{P_{atm}}{P_G} \exp \left[\frac{h_{fg} MW_V}{R} (T_B^{-1} - T_d^{-1}) \right], \quad (3.19)$$

where T_B is the boiling temperature, and P_G is found based on empirical correlations often available in a chemical handbook (for example, acetone properties used in this study are available in [71]). H_M is modelled as

$$H_M = \ln(1 + B_M). \quad (3.20)$$

There are also non-equilibrium evaporation models that can improve a prediction [122, 98, 53, 93]. The transport properties of the fluid near the droplets are usually evaluated by a one-third rule to estimate a reference temperature and species mass fraction as

$$T_r = T_S + \frac{1}{3}(T_G - T_S), \quad (3.21)$$

$$Y_r = Y_S + \frac{1}{3}(Y_G - Y_S). \quad (3.22)$$

However, ‘‘one-third’’ is an empirical choice, and some DNS studies also suggest a different ratio [193].

3.3.3 Two-Way Coupling

The gas and liquid phases are strongly coupled in multiphase systems. For example, the turbulence modulation (Sec. 3.1.2) due to particles can be seen in the shape of turbulence spectra [1], and evaporation of liquid fuel is crucial for spray combustion systems (Sec. 3.1.3). The source terms in the gas-phase equations are found by a summation of the effects that individual droplets exert on the gas phase. The present study applies the concept of computational parcels that consist of multiple

real droplets with identical characteristics such as position, velocity, temperature and radius. The spray source terms in Eqns. 2.18 - 2.21 are

$$\bar{\rho} = \frac{1}{V} \sum_{n=1}^N n_{p,n} \dot{m}_{p,n}, \quad (3.23)$$

$$\bar{\mathbf{F}} = \frac{1}{V} \sum_{n=1}^N n_{p,n} \left(m_{p,n} \tau_p^{-1} (\mathbf{v}_p - \mathbf{u}) + \dot{m}_{p,n} \mathbf{v}_p \right), \quad (3.24)$$

$$\bar{Q} = \frac{1}{V} \sum_{n=1}^N n_{p,n} \left(m_{p,n} \frac{Nu C p_g}{3 P r_g} \left(\frac{T_p - T_g}{\tau_p} \right) + \dot{m}_{p,n} h_v \right), \quad (3.25)$$

$$\bar{\rho}_k = \frac{1}{V} \sum_{n=1}^N Y_{d,\alpha} n_{p,n} \dot{m}_{p,n}. \quad (3.26)$$

Here, $n_{p,n}$ is the number of particles per parcel, N is the number of total parcels inside the computational cell, V is the cell volume, h_v is the enthalpy carried by the vapour, and $Y_{d,\alpha}$ is the mass fraction of species α in the vapour. The parcel concept is applied to simulations of evaporating spray jets in Chapter 6, but not to simulation of spray flames in Chapters 7-9 due to an instability caused by large source terms (see Chapter 7).

3.3.4 Numerical Integration

The sets of ODEs (Eqns. 3.3, 3.4, 3.8, 3.9) are integrated by explicit Euler integration such that

$$y_{n+1} = y_n + y'_n \Delta t^p, \quad (3.27)$$

where Δt^p is the time step for the particle tracking. Δt^p is chosen from the smallest time scales of the system, such as

$$\Delta t^p = \min \{ C_{int} \tau_p, C_{int} \tau_{temp}, C_{int} \tau_{mass}, \Delta t \}, \quad (3.28)$$

where τ_p is the particle response time scale defined in Eqn. 3.5, τ_{temp} is the time scale of Eqn. 3.8 defined as $\tau_{temp} = \frac{3 P r_g C p_l}{Nu C p_g} \tau_p$, τ_{mass} is the time scale of Eqn. 3.9 defined as $\tau_{mass} = \frac{3 S c_g}{Sh} \tau_p$, C_{int} is the time constant factor for the time scale, and Δt is the time

step of the CFD solver. Since this study uses Euler explicit time integration, a small value, $C_{int} = 0.1$, is chosen to avoid overshoots and ensure temporal accuracy, but this could be relaxed if a higher order scheme were chosen. Δt^p is usually smaller than a time step of the fluid solver ($\Delta t^p < \Delta t$) especially when the particle size is small, and therefore multiple sub-integrations are performed within each CFD time step.

Chapter 4

Conditional Moment Closure

The conditional moment closure has been established independently by Klimenko [95] and Bilger [10] based on different derivation approaches [96]. Conditional moment closure has been developed to model turbulent combustion and validated for many types of flame configurations. This study aims to apply CMC in spray flames that require additional modelling. In this chapter, the fundamentals of the CMC approach are provided, and the formulations of the two-phase CMC equations and the closures are discussed.

4.1 Fundamentals of CMC

4.1.1 Conditional Reaction Rate

As discussed in Sec. 2.6, the challenge of turbulent combustion is to model the filtered reaction rates,

$$\tilde{\omega}_\alpha = f \{ \overline{Y_1, Y_2, \dots, Y_N, T} \} \neq f \{ \tilde{Y}_1, \tilde{Y}_2, \dots, \tilde{Y}_N, \tilde{T} \}. \quad (4.1)$$

Favre-filtered quantities can be written as

$$Y_\alpha = \tilde{Y}_\alpha + Y'_\alpha, \quad (4.2)$$

where Y'_α is the fluctuation around the Favre-averaged quantity. Here, the conditional moment Q_α of species α is defined as

$$Q_\alpha(\xi, \mathbf{x}, t) \equiv \langle Y_\alpha(\mathbf{x}, t) | \xi(x, t) = \eta \rangle, \quad (4.3)$$

where angular brackets denote the average and the condition is given by the expression on the right of the vertical bar. Considering a non-premixed flame, the variable η is the sample space of the random variable ξ (mixture fraction). The instantaneous unconditional quantity can be related to the conditional quantity as

$$Y_\alpha = Q_\alpha(\eta, \mathbf{x}, t) + Y''_\alpha, \quad (4.4)$$

where Y''_α is the conditional fluctuation at a certain mixture fraction. Since the conditional average carries an additional correlation with the mixture fraction, the conditional fluctuations are a lot smaller than the unconditional fluctuations ($Y''_\alpha \ll Y'_\alpha$). In fact, past experimental studies indicate a decent agreement between conditionally averaged quantities and experimental samples. Figure 4.1 shows scatter plots of temperature and species compared to the conditional averages taken in a non-premixed flame experiment. It shows the clear correlation of temperature and species mass fraction with the mixture fraction, and the conditional fluctuations are found to be small. Therefore, a first order approximation is considered to be sufficient to approximate the conditional reaction rates as

$$\tilde{\omega}_{\eta,\alpha} = f \{Q_1, Q_2, \dots, Q_N, T_\eta\}, \quad (4.5)$$

where the subscript η indicates the conditional properties.

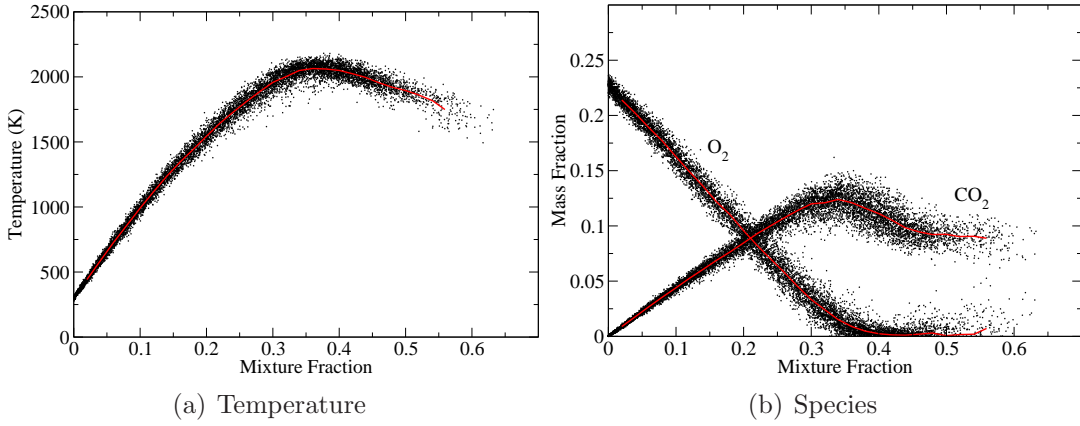


Figure 4.1: Scatter plot of the experimental datasets of Sandia flame D at $z/D=45$ [170]. Solid red lines are the conditional averages of the experimental results.

4.1.2 Conditional Filtering

In the LES formulation, the filter for the conditional moment must be properly defined [132]. First, define the fine-grained PDF, ψ , as

$$\psi_\eta \equiv \delta[\eta - \xi(\mathbf{x}, t)], \quad (4.6)$$

where δ indicates Dirac's delta function. With ψ_η and the spatial filter kernel defined for LES, G (in Sec. 2.2.1), the spatially filtered conditional moment of a scalar Φ can be defined by

$$\bar{\Phi}_\eta = \frac{\int_\Omega \Phi \psi_\eta G(\mathbf{r}) d\mathbf{r}}{\bar{P}(\eta)} \quad (4.7)$$

with a filtered PDF given by

$$\bar{P}(\eta) = \int_\Omega \psi_\eta G(\mathbf{r}) d\mathbf{r}. \quad (4.8)$$

As in LES, Favre-filtering is applied to the conditional quantities as

$$\tilde{\Phi}_\eta = \frac{\overline{\langle \rho \Phi | \eta \rangle}}{\bar{\rho}}. \quad (4.9)$$

The unconditionally filtered mass fraction is given by integration across mixture

fraction space

$$\tilde{\Phi} = \int \tilde{\Phi}_\eta \tilde{P}(\eta) d\eta. \quad (4.10)$$

The functional dependence on space and time is dropped here for convenience of notation, and $\tilde{P}(\eta) = \tilde{P}_\eta$ is the filtered conditional probability density function.

4.2 Two-Phase CMC Equations

Mortensen and Bilger [126] have developed a mathematically rigorous form of the CMC equations in two-phase flow. Based on a two-fluid model [87], gas and liquid phases are treated separately with interface conditions, and the CMC equation for liquid fuel combustion is derived as

$$\begin{aligned} \frac{\partial}{\partial t} Q_\alpha &+ \frac{1}{\bar{\rho}_\eta \tilde{P}_\eta} \nabla \cdot [\bar{\rho}_\eta \tilde{P}_\eta (U_\eta Q_\alpha - D_{t,\eta} \nabla Q_\alpha)] = \tilde{\omega}_{\eta,\alpha} + N_\eta \frac{\partial^2 Q_\alpha}{\partial \eta^2} \\ &+ \frac{Q_\alpha}{\bar{\rho}_\eta \tilde{P}_\eta} \nabla \cdot (\rho_\eta \tilde{P}_\eta U_\eta) + \left[Q_{1,\alpha} - Q_\alpha - (1 - \eta) \frac{\partial}{\partial \eta} Q_\alpha \right] \Pi_\eta \\ &- \frac{1}{\bar{\rho}_\eta \tilde{P}_\eta} \frac{\partial}{\partial \eta} ((1 - \eta) \bar{\rho}_\eta \tilde{P}_\eta \langle Y_\alpha'' \Pi'' | \eta \rangle). \end{aligned} \quad (4.11)$$

Here, subscript ‘1’ denotes the conditions in the liquid fuel, Π is the volumetric fuel evaporation rate, N is the scalar dissipation, $\tilde{\omega}_\alpha$ is the chemical source term of species α that can be closed by a first order approximation, and subscript η denotes the conditioned value at $\xi = \eta$. Also, the conditionally averaged enthalpy equation is

$$\begin{aligned} \frac{\partial}{\partial t} Q_h &+ \frac{1}{\bar{\rho}_\eta \tilde{P}_\eta} \nabla \cdot [\bar{\rho}_\eta \tilde{P}_\eta (U_\eta Q_h - D_{t,\eta} \nabla Q_h)] = N_\eta \frac{\partial^2 Q_h}{\partial \eta^2} \\ &+ \frac{Q_h}{\bar{\rho}_\eta \tilde{P}_\eta} \nabla \cdot (\rho_\eta \tilde{P}_\eta U_\eta) + e_{rad,\eta} + \left[Q_{1,h} - Q_h - (1 - \eta) \frac{\partial}{\partial \eta} Q_h \right] \Pi_\eta \\ &+ \Psi_\eta - \frac{1}{\bar{\rho}_\eta \tilde{P}_\eta} \frac{\partial}{\partial \eta} ((1 - \eta) \bar{\rho}_\eta \tilde{P}_\eta \langle h'' \Pi'' | \eta \rangle), \end{aligned} \quad (4.12)$$

where $Le = 1$ has been assumed, Q_h is the conditionally averaged enthalpy, and $e_{rad,\eta}$ is the radiation heat loss that is modelled assuming an optically thin flame. Ψ_η is the energy transfer term between spray and gas phase. As in earlier CMC

spray studies, $\langle Y_\alpha''\Pi'' | \eta \rangle$ and $\langle h''\Pi'' | \eta \rangle$ are assumed to be small and negligible [20] in the present study.

4.3 Closures

4.3.1 Conditional Velocity

The conditional properties U_η and $D_{t,\eta}$ are necessary to solve Eqns. 4.11 and 4.12. Various closures have been developed to model these conditional quantities. One of the simplest methods is a linear approximation given as [96, 127]

$$U_\eta \approx \tilde{U} + \frac{\overline{U''\xi''}}{\xi''^2} (\eta - \tilde{\xi}), \quad (4.13)$$

and it is assumed to be accurate when $|\eta - \tilde{\xi}|$ is small. Another common model is a gradient model [42] described by

$$U_\eta \approx \tilde{U} - \frac{D_t}{\tilde{P}(\eta)} \nabla P(\eta). \quad (4.14)$$

The gradient model is considerably better than the linear model since the linear model can only satisfy first moments whereas the gradient model is consistent in first and second moments [125]. In practice, both linear and gradient models are used in many computations. Earlier studies tested both models and reported that no significant difference is found [39, 40, 164]. Also, conditional averages can be established by taking samples from CFD cells since a CMC cell consists of a number of CFD cells, $\Delta_{CMC} \gg \Delta_{CFD}$ (see Sec. 4.4.1). Therefore, sampling can be performed to construct the conditional velocity as [132]

$$U_\eta \approx \langle \tilde{U} | \tilde{\xi} = \eta \rangle. \quad (4.15)$$

Similarly, the conditional turbulent diffusivity is modeled as

$$D_{t,\eta} \approx \langle \widetilde{D}_t | \widetilde{\xi} = \eta \rangle. \quad (4.16)$$

This thesis uses this sampling process to construct conditionally averaged quantities.

4.3.2 Conditional Scalar Dissipation

There are sets of standard models for conditional scalar dissipation. The amplitude mapping closure (AMC) [134] is one of the most common approaches. AMC specifies a profile of N_η over mixture fraction space, and an amplitude is selected to recover a scalar dissipation rate at a reference point. AMC is given as

$$N_\eta = N_0 \exp\left(-2 \left[\operatorname{erf}^{-1}(2\eta - 1)\right]^2\right), \quad (4.17)$$

where N_0 is the scaling parameter chosen as

$$N_0 = \frac{\widetilde{N}}{\int_0^1 \widetilde{P}(\eta) \exp\left(-2 \left[\operatorname{erf}^{-1}(2\eta - 1)\right]^2\right) d\eta}. \quad (4.18)$$

A drawback is that the model assumes the presence of unmixed fluid, so AMC might not be strictly applicable in the mixing region of a complex system. However, it is often used due to its simplicity. Girimaji's model [68] is given as [164]

$$N_\eta = -2\widetilde{N} \frac{\widetilde{\xi}(1 - \widetilde{\xi}) I(\eta)}{\widetilde{\xi}''^2 \widetilde{P}(\eta)}, \quad (4.19)$$

where

$$I(\eta) = \int_0^\eta \left\{ \widetilde{\xi}(\ln \eta' - \widetilde{\ln} \xi + (1 - \widetilde{\xi}) [\ln(1 - \eta') - \widetilde{\ln}(1 - \xi)]) \right\} \widetilde{P}(\eta') (\eta - \eta') d\eta'. \quad (4.20)$$

Girimaji's model assumes a homogeneous flow, so that it might not be valid for strong shear layers. Kronenburg et al. [100] have proposed a PDF transport equation model that does not require assumptions used in AMC and Girimaji's model.

Assuming high-Reynolds number flow, the PDF transport equations can be written as [100]

$$\frac{\partial \rho_\eta P_\eta}{\partial t} + \nabla \cdot (\langle \rho \mathbf{U} | \eta \rangle P_\eta) + \frac{\partial}{\partial \eta^2} (\langle \rho N | \eta \rangle P_\eta) = 0. \quad (4.21)$$

Depending on the flow configuration, a spatial averaging process can be carried out to simplify Eqn. 4.21. Assuming local self-similarity, steady-state and small conditional fluctuations of U_η ($U_\eta \approx \tilde{u}$), Eqn. 4.21 can be rewritten as

$$\{\bar{\rho} N_\eta \tilde{P}_\eta\}_R = \frac{\partial}{\partial x} \left\{ \bar{\rho} \tilde{u} \int_\eta^1 \tilde{P}_\eta(\eta', r) (\eta - \eta') d\eta' \right\}_R, \quad (4.22)$$

where $\{ \}_R$ denotes averaging in radial direction. Even though this approach does not rely on assumptions used for the AMC and Girimaji's model, it can be computationally expensive if a robust solution procedure that involves a coordinate transformation and double integration is employed [100]. A comparison of AMC, Girimaji's model and a PDF transport equation model has been carried by Sreedhara et al. [164]. Even though some differences between models are observed, it is difficult to argue superiority of one of the models. A more general form including unsteadiness and conditional velocity fluctuations was developed by Devaud et al. [48]. Assuming Eqn. 4.13, Eqn. 4.21 can be rewritten as [48],

$$\tilde{P}_\eta N_\eta = -\frac{1}{\bar{\rho}} \left\{ \frac{\partial \bar{\rho} \tilde{I}_1(\eta)}{\partial t} + \nabla \cdot \left(\bar{\rho} \tilde{U} \tilde{I}_1(\eta) + \bar{\rho} \frac{\overline{U'' \xi''}}{\xi''^2} \tilde{I}_2(\eta) \right) \right\}, \quad (4.23)$$

where

$$\tilde{I}_n(\eta) = \int_\eta^1 (\eta' - \eta) (\eta' - \xi)^{n-1} \tilde{P}(\eta') d\eta', \quad n = 1, 2. \quad (4.24)$$

The new PDF transport equation model and its derivation with a coupling with the gradient model (Eqn. 4.14) are analyzed and compared to AMC and Girimaji's model for a lifted jet flame in [120, 24].

Even though the PDF transport equation model may improve the prediction of N_η , it still is restricted by the models for conditional velocity. Also, the integration of the probability can be computationally expensive in LES. Therefore, this study

uses the sampling from LES cells by assuming that $\Delta_{CMC} \gg \Delta_{LES}$ [132] as

$$N_\eta \approx \langle \widetilde{N} | \widetilde{\xi} = \eta \rangle. \quad (4.25)$$

4.3.3 Conditional Spray Source

The two-phase CMC equations introduce extra spray terms appearing as

$$\left[Q_{1,\alpha} - Q_\alpha - (1 - \eta) \frac{\partial}{\partial \eta} Q_\alpha \right] \Pi_\eta. \quad (4.26)$$

in Eqn. 4.11. A major difficulty of this term is the selection of a mixture fraction for conditioning, and there are two major approaches: the *microscopic* and *macroscopic* approach. The microscopic approach models the small scale physics around individual droplets. The droplet evaporation physically occurs at the surface condition, so the mixture fraction at the surface, ξ_{surf} is selected for conditioning, and Borghesi et al. [20] have modelled the conditional evaporation term as

$$\Pi_\eta = \frac{\widetilde{\Pi} \delta(\eta - \xi_{surf})}{\widetilde{P}(\eta)}. \quad (4.27)$$

This approach requires subsequent models for the probability $\langle N | \xi_{surf} \rangle$ and scalar dissipation rate on a droplet surface $\widetilde{P}(\xi_{surf})$. Moreover, the microscopic approach requires proper models for $\widetilde{\xi}$ and ξ_{surf} since ξ_{surf} tends to be a lot larger than $\widetilde{\xi}$, and it is usually possible only under a certain flow condition such as steady stationary condition as demonstrated in the Appendix A.2. Under a fully resolved droplet simulation, the microscopic approach would be appropriate, and no extra subgrid modelling associated with droplets would be necessary. However, it would be difficult to apply the microscopic approach with a Lagrangian tracking approach where the microstructures around droplets are empirically modelled. Therefore, this study chooses the macroscopic approach that models the spray source terms based on the filtered quantities. Assuming a droplet diameter is a lot smaller than an LES cell size, the scalar dissipation rate near the droplet surface is a lot larger than the scalar

dissipation rate at the filtered mean due to the large gradient (see. Appendix A.2). Therefore, the effects of the spray evaporation source terms are rapidly transferred from ξ_{surf} to $\tilde{\xi}$. Thus, the conditional spray evaporation term is modelled as

$$\Pi_\eta = \frac{\tilde{\Pi}\delta(\eta - \tilde{\xi})}{\tilde{P}(\eta)}, \quad (4.28)$$

and similarly the conditional heat transfer term is

$$\Psi_\eta = \frac{\tilde{\Psi}\delta(\eta - \tilde{\xi})}{\tilde{P}(\eta)}, \quad (4.29)$$

where the unconditional quantities are

$$\tilde{\Pi} = \frac{1}{\bar{\rho}V} \sum_{n=1}^N \dot{m}_{p,n}, \quad (4.30)$$

$$\tilde{\Psi} = \frac{1}{\bar{\rho}V} \sum_{n=1}^N m_{p,n} \frac{NuCp_g}{3Pr_g} \left(\frac{T_p - T_g}{\tau_p} \right). \quad (4.31)$$

Here, Nu is the Nusselt number, Cp_g is the specific heat of the gas, Pr_g is the gas phase Prandtl number, and T_p and T_g are the temperatures of the droplet and the gas phase, respectively. More discussion of the conditional spray source terms is given in Sec. 7.1.4. A detailed discussion of micro- against macroscopic approaches is given in Appendix A with examples.

4.3.4 Heat Radiation

Radiation is often neglected in turbulent combustion models, but it is well known to cause noticeable differences in the flame temperature profiles. It is common to follow an optically thin medium assumption in single phase flow, and a computationally cheap radiation model is well established [9, 170]. In case of solid fuel combustion (e.g. coal), the effect of radiation interactions are very strong, and the optically thin assumption is not usually valid [162]. Regarding the spray flame, Watanabe et al. [188] tested a radiation model based on the discrete ordinate method and found that radiative heat transfer between gaseous phase and liquid fuels to be negligible.

Thus, this study utilizes the optically thin radiation model. In the conditionally averaged form, the radiation model is

$$e_{rad,\eta} = 4\sigma_B (T_\eta^4 - T_0^4) \sum_{i=1} (P_i a_{p,i}), \quad (4.32)$$

where P_i is the partial pressure of the i -th radiating species, $a_{p,i}$ is the Planck mean absorption coefficient of the i -th species, σ_B is the Stefan-Boltzmann constant and T_0 is the background temperature. The radiating species are chosen as CO_2 , H_2O , CO and CH_4 , and the coefficients are available in [9, 170].

4.3.5 Subgrid FDF

Once conditional moments are obtained by solving their transport equations, the LES-filtered quantity is obtained by integrating over the filtered density function. For example, the LES-filtered species mass fraction is computed as

$$\tilde{Y}_\alpha = \int Q_\alpha \tilde{P}(\eta) d\eta. \quad (4.33)$$

Here, the subgrid scale FDF $\tilde{P}(\eta)$ must be modelled appropriately. Since it is computationally very expensive to obtain the subgrid FDF in each LES cell, an assumed form is often utilized. Usually, an assumed FDF requires two inputs, the mean and the variance of the distribution. Even though the mean of the mixture fraction is easily obtained by solving the transport equation, the variance of the mixture fraction, $\widetilde{\xi'^2}$, requires extra modelling. In RANS, $\widetilde{\xi'^2}$ is often obtained by solving its transport equation of $\widetilde{\xi'^2}$ (cf. Eqn. 2.40). In the LES study, $\widetilde{\xi'^2}$ is often modelled by the local gradient of the resolved mixture fraction as

$$\widetilde{\xi'^2}_{sgs} = C_\xi \Delta^2 \left(\frac{\partial \tilde{\xi}}{\partial x_i} \frac{\partial \tilde{\xi}}{\partial x_i} \right). \quad (4.34)$$

where $C_\xi = 0.1$ [132]. Comparisons of the local gradient model and the transport equations with three different spray source term closures are performed in Appendix A, but due to the uncertainty of the spray source term closures, this study chooses

the local gradient model.

For the case of binary mixing of a passive scalar, the β -FDF is known to represent the FDF well [67, 121, 57]. The β -FDF can be written as

$$P(\eta) = f(\eta; s, t) = \frac{\Gamma(s+t)}{\Gamma(s)\Gamma(t)} \eta^{s-1} (1-\eta)^{t-1}, \quad (4.35)$$

where Γ is the gamma function, and s and t are the shape factors given as functions of mean and variance of the mixture fraction,

$$s = \tilde{\xi} \left[\frac{\tilde{\xi}(1-\tilde{\xi})}{\widetilde{\xi''^2}} - 1 \right], \quad (4.36)$$

$$t = (1-\tilde{\xi}) \left[\frac{\tilde{\xi}(1-\tilde{\xi})}{\widetilde{\xi''^2}} - 1 \right]. \quad (4.37)$$

However, strictly speaking, the conventional β -FDF is only valid if the unmixed properties (or initial state) is bounded by 0 and 1. If the scalar has a source or sink term (e.g. evaporation or condensation), the bounds may change. Therefore, to ensure validity of the FDF modelling approach, a *bounded* β -FDF is introduced as

$$P(\eta) = f(\eta; p, q, \xi_{LL}, \xi_{UL}) = \frac{\Gamma(p+q)}{\Gamma(p)\Gamma(q)} \frac{(\eta - \xi_{LL})^{p-1} (\xi_{UL} - \eta)^{q-1}}{(\xi_{UL} - \xi_{LL})^{p+q-1}}, \quad (4.38)$$

where ξ_{LL} and ξ_{UL} are the lower and upper bounds of the FDF, and p and q are shape parameters for the bounded β -FDF constructed as

$$p = \frac{\tilde{\xi} - \xi_{LL}}{\xi_{UL} - \xi_{LL}} \left[\frac{(\tilde{\xi} - \xi_{LL})(\xi_{UL} - \tilde{\xi})}{\widetilde{\xi''^2}} - 1 \right], \quad (4.39)$$

$$q = \frac{\xi_{UL} - \tilde{\xi}}{\xi_{UL} - \xi_{LL}} \left[\frac{(\tilde{\xi} - \xi_{LL})(\xi_{UL} - \tilde{\xi})}{\widetilde{\xi''^2}} - 1 \right]. \quad (4.40)$$

Chapter 8 proposes a new modelling approach of ξ_{UL} in two-phase flows, and ξ_{LL} in this thesis is kept as zero.

4.4 Numerical Approach

The conservative form of the two-phase CMC equations (Eqns. 4.11 and 4.12) are discretized using the finite volume method. The numerical schemes are presented elsewhere [39, 182, 159, 160] and adapted without major modifications. Here, a brief description of the numerical approach is given.

4.4.1 Computational Grid

Since the CMC equation is solved using one additional independent scalar, (e.g. mixture fraction space), the dimensionality of the problem is higher, and it is not computationally tractable to have a CMC cell as small as an LES cell. Therefore, a large CMC grid is constructed over ensembles of LES cells as shown in Fig. 4.2, and conditional quantities are assumed to be homogeneous within a CMC cell.

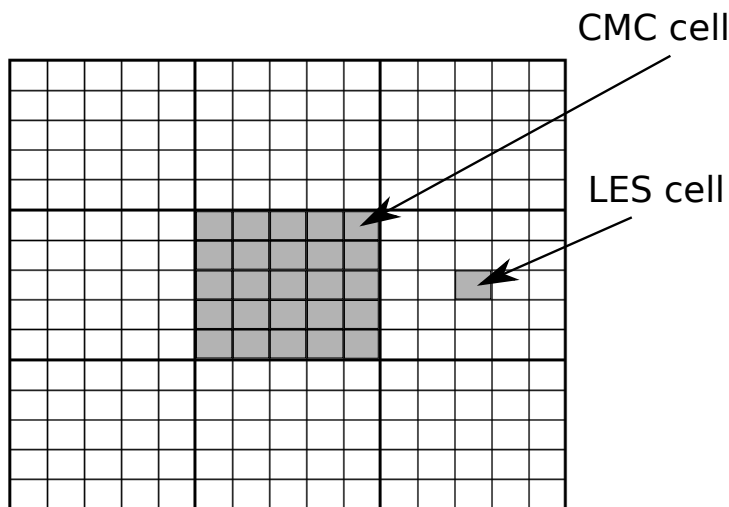


Figure 4.2: Diagram of CMC and LES cells. Thick lines indicate CMC cell boundaries, and thin lines represent LES cell boundaries.

4.4.2 Discretization

The finite volume method solves for the transport equation with the volume integration. The Gauss's divergence theorem is applied to transform divergence terms

into the surface integration that can be represented as the surface area and the flux. A section of the CMC cell (Fig. 4.3) is shown as an example for the discretization in 2D space, and the discretization of Eqn. 4.11 is given as

$$\begin{aligned}
\frac{\partial}{\partial t}(\gamma Q_\alpha V)_P &+ \gamma_e A_e \left(\tilde{u}_\eta Q_\alpha - D_{t,\eta} \frac{\partial Q_\alpha}{\partial x} \right)_e - \gamma_w A_w \left(\tilde{u}_\eta Q_\alpha - D_{t,\eta} \frac{\partial Q_\alpha}{\partial x} \right)_w \\
&+ \gamma_n A_n \left(\tilde{v}_\eta Q_\alpha - D_{t,\eta} \frac{\partial Q_\alpha}{\partial y} \right)_n - \gamma_s A_s \left(\tilde{v}_\eta Q_\alpha - D_{t,\eta} \frac{\partial Q_\alpha}{\partial y} \right)_s \\
&= \gamma V \left(\tilde{w}_{\alpha,\eta} + \tilde{N}_\eta \frac{\partial^2 Q_\alpha}{\partial \eta^2} + \left[Q_{1,\alpha} - Q_\alpha - (1-\eta) \frac{\partial}{\partial \eta} Q_\alpha \right] \Pi_\eta \right)_P \\
&+ Q_{\alpha,P} ((\gamma \tilde{u}_\eta A)_e - (\gamma \tilde{u}_\eta A)_w + (\gamma \tilde{v}_\eta A)_n - (\gamma \tilde{v}_\eta A)_s).
\end{aligned} \tag{4.41}$$

where, γ is the density weighted FDF, $\gamma \equiv \rho_\eta P_\eta$, A and V is the face area and the volume of the CMC cell, respectively, and subscripts e , w , n and s denote the conditions of faces at the CMC cell P .

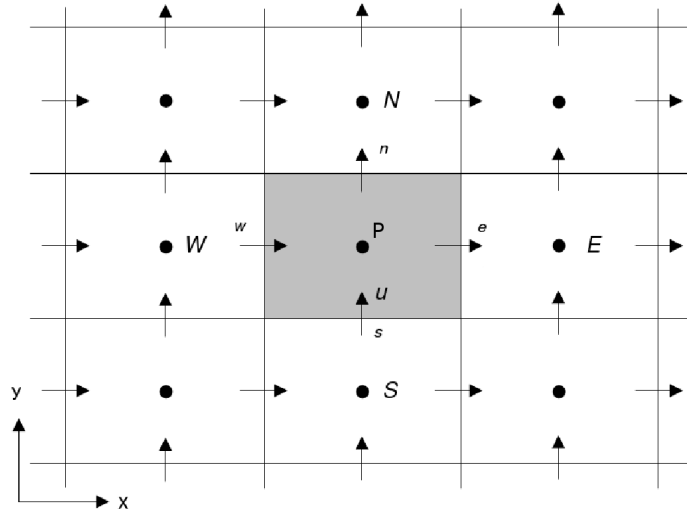


Figure 4.3: Discretization of CMC cells in space [39].

The scalar dissipation is discretized by a standard finite difference method (FDM) in mixture fraction space. The discretization approaches of the spray source terms

are given as

$$\begin{aligned} & \left[Q_{1,\alpha} - Q_\alpha - (1 - \eta) \frac{\partial}{\partial \eta} Q_\alpha \right] \Pi_\eta = \\ & \left[Q_{1,\alpha} - Q_\alpha - (1 - \eta) \frac{Q_\alpha(\eta) - Q_\alpha(\eta^*)}{\eta - \eta^*} \right] \frac{\Pi}{1 + \Delta\Pi} \frac{\delta(\eta - \tilde{\xi})}{P(\eta)}, \end{aligned} \quad (4.42)$$

where $\Delta\Pi$ is the volume of fuel evaporated within a time step, Δt , given as $\Delta\Pi = \Delta t \cdot \Pi$ and η^* is the pseudo-mixture fraction before the evaporation step and found as $\eta^* = \eta(1 + \Delta\Pi) - \Delta\Pi$. Detailed derivations of the discretization of the spray source term is given in Appendix B. Readers may find further details on the numerical scheme employed in past theses [39, 182, 159].

Chapter 5

Target Flame Configurations

Experimental datasets lay the foundation for the validation of numerical models. The workshop series on turbulent non-premixed flames (TNF), for example, has established a culture for worldwide collaboration between many numerical and experimental groups which led to high quality databases of well-defined turbulent flames (e.g. the Sandia flame series) and has set the grounds for model validation and comparison which is almost unique for the community. In a similar vein, a new workshop called “Workshop on Measurement and Computation of Turbulent Spray Combustion” (TCS) has been established in 2009. In TCS 2, spray flame experiments were reviewed and summarized (also seen in [82]), and a series of spray flame studies performed by Masri and Gounder [69, 113] were chosen to be reference cases to test numerical approaches. They have conducted experiments for a series of acetone evaporating jets, acetone spray flames and ethanol spray flames by changing jet velocity and the amount of fuel, and prepared datasets available to researchers for model development and validation. This chapter briefly introduces the experimental configurations, and selected cases are used for validation of the proposed new models. Detailed information on the experiments can be found in [113, 69, 118, 70, 82]

5.1 Burner Configuration

Figure 5.1 shows the setup and configuration of the burner. An ultrasonic nebulizer is used to atomize the liquid fuel upstream of the jet inlet. The nozzle diameter, D , is 10.5 mm, the outer annulus diameter of the piloted flow is 25 mm, and the co-flow diameter is 104 mm. Parametric studies of bulk velocities and spray mass flow rates were conducted in the experiments. The bulk velocity of the pilot is 4.5 m/s for a non-reacting jet and 11.9 m/s for a reacting flame, and the bulk velocity of the co-flow is 4.5 m/s for both reacting and non-reacting flows. Acetone spray is generated upstream of the nozzle exit, so that a certain portion of the spray evaporates before reaching the nozzle exit.

Mean temperature profiles were measured by an R-Type thermocouple. The spray velocities were obtained by phase-Doppler anemometry (PDA) at different cross sections. Also, laser induced fluorescence (LIF) was used to take images of acetone and OH. Typical measurement uncertainties that can be associated with these techniques are of the order of 10% for the temperature measurements, and 6% and 15% for the velocity measurements of mean and rms, respectively [112].

5.2 Selection of Target Cases

Masri and Gounder [113] have performed a parametric study of non-reacting spray jets (the SP series) and reacting acetone spray flames (the AcF series) by changing the gas and liquid flow rates, and the diagram of the parametric study is shown in Fig. 5.2. This study selects some cases as target experiments and performs numerical analysis. First, the LES and the spray modelling introduced in Chapters 2 and 3 are tested based on SP 4 in Chapter 6. Then, simulations of acetone spray flames are carried out to test different CMC approaches in Chapters 7 - 9. Since the present CMC is an extension of a mixture fraction based approach for non-premixed gaseous flames, the flame shall burn largely in non-premixed mode which excludes flames with pre-evaporation leading to a gaseous mixture being close to stoichiometric at the nozzle exit. Therefore, the study considers the four cases, AcF 1, AcF 2, AcF 3

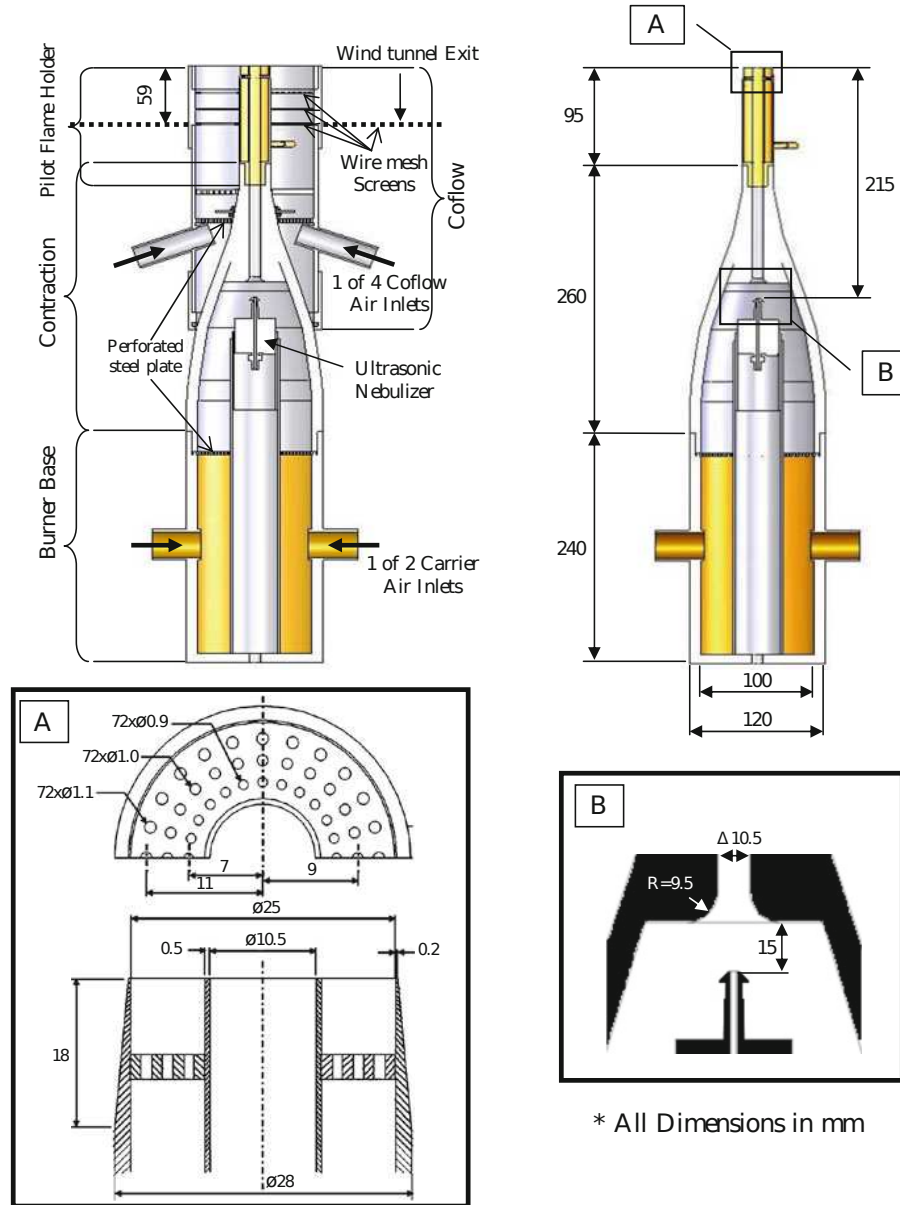


Figure 5.1: Schematics of the spray burner inlet [118].

and AcF 5. The inflow gas velocity and liquid fuel flow rates of the selected cases are listed in Table 5.1. Since the maximum mixture fraction within the domain changes dynamically due to the evaporation, the mixture fraction is scaled such that it is unity for pure fuel mixtures. Thus, the mixture fraction of the jet fuel is simply taken as

$$\xi_{jet} = \frac{\dot{m}_{vf}}{\dot{m}_{vf} + \dot{m}_{air}}, \quad (5.1)$$

where \dot{m}_{vf} and \dot{m}_{air} are the mass flow rate of fuel vapour and air, respectively. The mixture fraction of the pilot is $\xi_{pilot} = 0.0858$, and ξ_{jet} of each case is listed in Table 5.1.

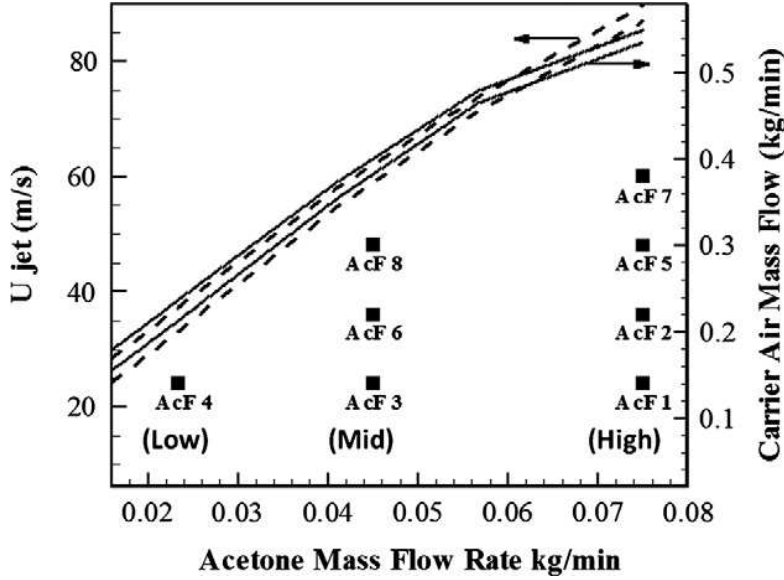


Figure 5.2: Diagrams for the parameters for the acetone flame cases (AcF series) taken from [70]. The lines indicate the blowoff limits. Conditions are identical for the evaporating spray jet case (SP series).

Table 5.1: Parameters of an evaporating spray jet (SP) and reacting acetone flames (AcF).

	SP 4	AcF 1	AcF 2	AcF 3	AcF 5
Bulk velocity (m/s)	24	24	36	24	48
Carrier mass flow rate (g/min)	150	150	225	150	301
Liquid fuel injection rate (g/min)	23.4	75	75	45	75
Measured liquid fuel rate at inlet (g/min)	10.6	18.0	23.9	15.9	27.8
Vapour fuel rate at inlet (g/min)	12.8	57.0	51.1	29.1	47.2
ξ_{jet}	-	0.275	0.185	0.162	0.136

5.3 Numerical Configurations and Setups

Mean and fluctuation of the axial velocity at the nozzle exit were measured in the experiments, and the mean inflow velocity profiles for LES are generated based on it. The digital filtering technique developed by Klein et al. [94] is used to generate

inflow turbulence. More detailed investigations of inflow turbulence generators can be found elsewhere [51]. The temperature of the jet was not measured in the experiments, so that 293 K is used as proposed in [69]. Since the particle statistics are measured at $z/D = 0.3$, the particles are inserted into the numerical domain at this location using the measured size and velocity distribution.

For the non-reacting study (Chapter 6), the numerical domain is taken to be a rectangular box with $20D \times 20D \times 50D$, and $82 \times 82 \times 252$ LES cells are used with grid clustering close to the jet nozzle. To reduce the computational cost of the particle tracking scheme, computational parcels representing 20 spray particles are used. A slip-wall BC is used at the side, and a zero-gradient BC is applied at the outflow boundary. Then, the reacting spray flame simulations conducted in Chapters 7 - 9 use a diverging domain with $40D$ in axial direction and $10D \times 10D$ at the inlet cross section to cluster more grid points near the jet inlet. In Chapter 7, $96 \times 96 \times 240$ LES cells and $3 \times 3 \times 40$ CMC cells are applied. The two-conditional moment approach developed in Chapter 8 focuses on the effects of evaporated vapour on conditional moments, so that finer CMC grids are applied. Thus, $90 \times 90 \times 240$ LES cells and $15 \times 15 \times 40$ CMC cells are used. Note that the LES grid size is slightly modified to adjust the CMC cell distribution. CMC with tabulated chemistry in Chapter 9 uses $90 \times 90 \times 240$ LES cells $3 \times 3 \times 16$ and CMC cells. The coarse CMC grid resolution is applied since the memory and computational loads of the employed two-dimensional tabulated chemistry is large. In the analysis of reacting flows, the computational parcel approach is not applied to avoid large source terms and to keep the computation stable.

The properties of acetone are adapted from [71]. There are several acetone mechanisms available in past studies. Chong and Hochgreb [36] have extended GRI 3.0 by additional acetone sub-mechanisms, and it consists of 38 species and 224 reactions. Pichon et al. [142] have developed another acetone mechanism based on the dimethyl ether mechanism, and it involves 81 species and 419 reactions. Note that this thesis assumes N_2 to stay inert to reduce computational requirements, so both mechanisms are reduced from the original sets by removing nitrogen related

reactions. Both mechanisms are compared, but no significant difference could be observed under the condition discussed in Chapter 7. Thus, Chong’s mechanism is preferred because the number of species and reactions are lower, and it is applied to simulations presented in Chapters 7 and 8. However, in Chapter 9, Chong’s mechanism causes some instabilities when computing the equilibrium solution needed for the construction of the tabulated chemistry, so that Pichon’s mechanism is used instead. The computational considerations are summarized in Table 5.2.

Table 5.2: Grid size and chemistry used in each methodology.

	LES grid	CMC grid	Parcel size	Chem. Mech.
Chapter 6	$82 \times 82 \times 252$	-	20	-
Chapter 7	$96 \times 96 \times 240$	$3 \times 3 \times 40$	1	Chong
Chapter 8	$90 \times 90 \times 240$	$15 \times 15 \times 40$	1	Chong
Chapter 9	$90 \times 90 \times 240$	$3 \times 3 \times 16$	1	Pichon

Chapter 6

Evaporating Spray Jet

The scope of this chapter is to analyze the behavior of the non-reacting evaporating spray jets that is essential for the understanding of spray combustion. Experiments of evaporating spray jets of acetone have been conducted [32], and numerical studies based on the configuration were successfully performed with the combination of LES and the Lagrangian particle tracking approach with stochastic dispersion and evaporation models [17]. However, these studies lack the direct link to reacting flows. A series of non-reacting and reacting spray jets was performed with well defined boundary conditions [69, 113]. One of the non-reacting cases from the database is chosen to test LES and a Lagrangian approach with and without the stochastic particle models developed by Bini and Jones [17] to establish a baseline analysis of non-reacting two-phase flows [174].

6.1 Numerical Modelling Approach

This evaporation study is to validate the LES-particle interactions. Mass, momentum, fuel species and enthalpy transport equations are solved simultaneously (see Eqn. 2.18-2.21). A Lagrangian approach is used to solve spray dispersion and evaporation (cf. Eqns. 3.3, 3.4, 3.8 and 3.9). The effects of the stochastic terms in Eqns. 3.4 and 3.9 are also examined. The simulation is based on one of the acetone evaporating spray jet experimental cases, SP 4, and the conditions are given in Table 5.1.

Also, numerical configurations are summarized in 5.3

6.2 Results and Discussion

Two different simulations have been performed: in Case 1 the Lagrangian particles are not subject to any turbulent (stochastic) subgrid effects on transport and evaporation. They move deterministically following the instantaneous, filtered velocity vectors interpolated on the particle location. In Case 2, a Lagrangian particle tracking method with additional stochastic motion and evaporation terms are employed [17]. Then, the effects of the stochastic model on particle distributions and evaporation can be examined for the present flow configuration.

First, an instantaneous profile of gas flow and particle distributions is shown in Fig. 6.1. Liquid particles initially stay near the center of the jet, but after the jet breakup, turbulent eddy motion causes the dispersion of particles in radial direction.

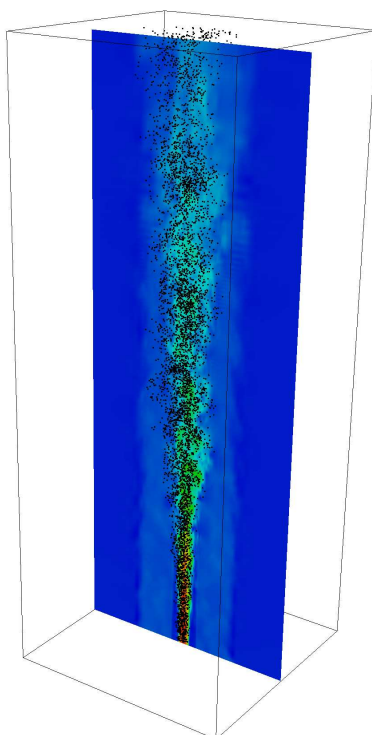


Figure 6.1: Instantaneous snapshot of the gas axial velocity (color contour), and the liquid droplets (black dots) from Case 1.

6.2.1 Mean Velocity Profiles

Since the relative motion between particle and gas phase strongly depends on the particle response time given by Eqn. 3.5, the different particle statistics are based on the particle diameter, D . Here, five particle size classes are defined as Class 1 with $D < 10\mu m$, Class 2 with $10\mu m < D < 20\mu m$, Class 3 with $20\mu m < D < 30\mu m$, Class 4 with $30\mu m < D < 40\mu m$ and Class 5 with $40\mu m < D < 50\mu m$. The effect of the particle diameter on droplet velocity is clearly observed in Fig. 6.2.

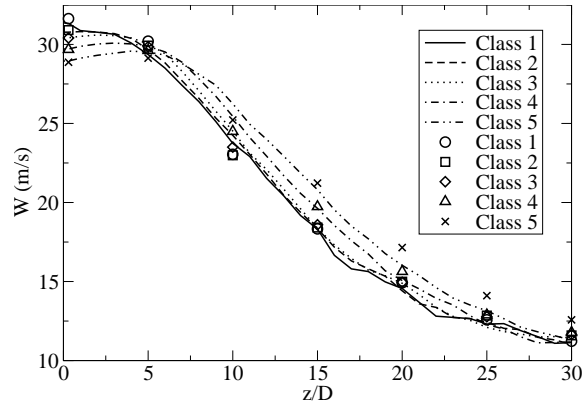


Figure 6.2: Comparisons of computations (Case 1) and experiments of the axial velocities of different particle size classes along the centerline. Lines represent results from the simulations with different particle size classes, and symbols represent the experimental results of each corresponding class.

The initial axial velocities of each size class are different. The mean axial velocity of Class 1 is about 31 m/s , whereas it is for Class 5 only 29 m/s . After the jet breaks up at around $z/D = 5$, the small particles decelerate more rapidly following the gas flow, while the larger particles (Classes 4 and 5) conserve their larger axial velocities due to their inertia. The mean velocities of Classes 1-3 do not vary significantly since their particle response times are small enough for the particles to follow the spreading of the jet and the accompanying decay of the axial gas velocity. Overall, the numerical predictions match the experimental results for all classes quite well, and particle dispersion can be modelled reasonably well using LES even without subgrid-scale models as will be quantified now. The turbulent eddies have strong effects on the radial dispersion of the particles. Here, the numerical predictions and experimental results are compared in two planes, at $z/D = 10$ and $z/D = 20$, and

the effect of the stochastic models is explicitly examined. The mean axial and radial velocity profiles are presented in Fig. 6.3. The mean axial velocities of the numerical and experimental results agree very well in both planes. The mean radial velocity profiles tend to be underpredicted but predictions are still very good. The effects of the stochastic models (Case 2) on the axial and radial mean profiles are found to be small.

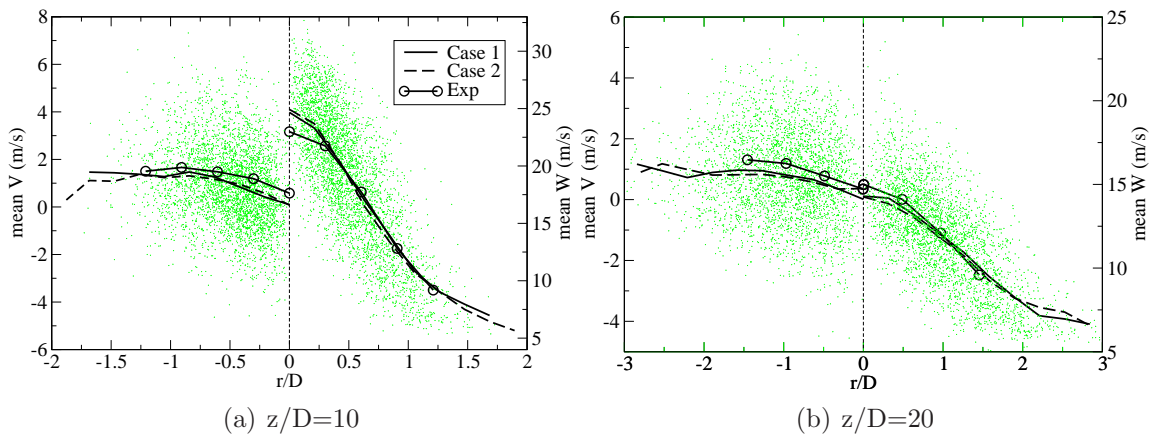


Figure 6.3: Comparisons of numerical predictions and experimental results for the axial velocity, W , (right half) and the radial velocity, V , (left half). Green dots represent computed particle velocities from Case 1, and all statistics are based on particle size Class 2.

6.2.2 RMS Velocity Profiles

The root mean square (rms) profiles of the axial and radial velocities at different cross sections are presented in Fig. 6.4. At $z/D = 10$, the rms of the axial velocities closely follows the experimental data. However, at $z/D = 20$, the numerical results predict 10 % to 20 % smaller values than observed in the experiments. The rms of the radial velocity shows the correct qualitative behavior, but the numerical study underpredicts the measured magnitude by about 20 %. However, more importantly, the effects of subgrid scale models are not very prominent and do affect neither the predictions of mean velocities nor their rms. One of the reasons may be the relatively low jet exit Reynolds number of the jet investigated here.

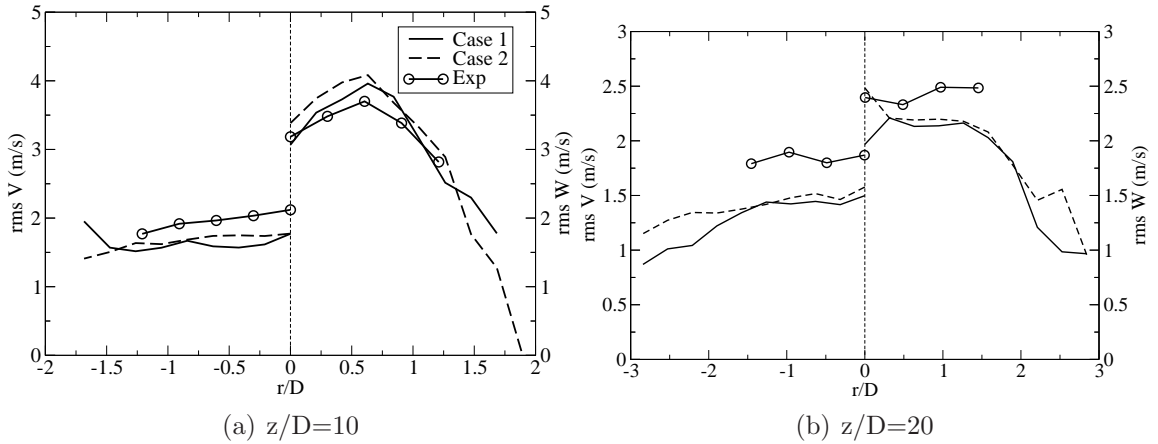


Figure 6.4: Comparisons of numerical predictions and experimental results for the rms of axial (right half) and radial velocities (left half). All statistics are based on particle size Class 2.

6.2.3 Evaporation Rates

In addition to spray dispersion, the evaporation rates are an important parameter for spray combustion. The flow rate of the liquid phase is a good indicator for the evaporation rate, and computed and measured liquid volume flow rates are compared in Fig. 6.5 as functions of the axial distance from the nozzle. Rapid evaporation is found right after the injection, and the flow rate decreases linearly in axial direction. It is notable that now the subgrid scale seems to affect the evaporation rate. This is in contrast to the droplet motion that was only weakly affected by the introduction of the stochastic model. With respect to the evaporation rates, however, the subgrid effects cause larger evaporation rates since the subgrid term is always positive ($Sh^{sgs} \geq 0$ from Eqn. 3.10). This is consistent with the finding of [17] for a similar evaporation study.

6.3 Summary

The current study has examined the evaporating spray jet by LES and a Lagrangian tracking scheme with a stochastic subgrid model. Two numerical simulations, a Lagrangian model with and without stochastic subgrid scale closure have been compared with the experimental results. The numerical studies recover the mean axial

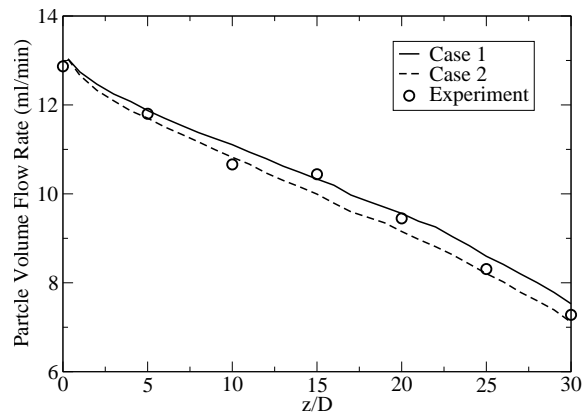


Figure 6.5: Comparisons of the liquid flow rates of simulations and experiments.

velocity profile in axial and radial directions. Also, the rms profiles of axial velocity are well predicted. However, the mean and rms profiles of the radial velocities are underpredicted by about 20 %. Effects of subgrid scales on velocity statistics are not very important, probably due to the moderate turbulence levels of the spray jet investigated here. This chapter indicates that the basic LES and spray modelling approach is valid. From the next chapter, CMC is added in the modelling methodology to simulate turbulent spray flames.

Chapter 7

Turbulent Spray Flame with Conventional CMC

As discussed earlier in Chapter 1, turbulent spray combustion involves a very wide range of physical scales. Chapter 6 shows that the numerical predictions of evaporation spray jets agree well with experimental results. This chapter further extends the analysis into turbulent spray flames, and performs the LES-CMC with the spray source term for the first time [175]. The modelling of the conditionally averaged evaporation terms in the CMC species and enthalpy equations are examined, and improved closures are suggested to ensure consistency with the LES-filtered values. Also, the treatment of the boundaries in mixture fraction space is investigated. After the justifications of the modelling approach, a simulation of a turbulent spray flame (AcF 3 in Table 5.1) is conducted, and the results are compared with the experiments.

7.1 Two-Phase LES-CMC

7.1.1 Formulations

In the LES context, the mass, momentum and mixture fraction transport equations are solved (Eqns. 2.18, 2.19 and 2.31). The Lagrangian method is used to com-

pute the droplet behavior. To reduce the complexity, the stochastic dispersion and evaporation model is not used unless noted (except for the analysis in Sec. 7.2.3). The CMC equations with spray source terms (Eqns. 4.11 and 4.12) are solved, and closures of the spray source term follows Eqns. 4.28 and 4.29.

7.1.2 Definition of Mixture Fraction

It is necessary to define the upper bound of mixture fraction to solve the CMC equations. Usually, mixture fraction is defined to be unity in the fuel mixture and zero in the oxidizer stream. The boundary conditions in the mixture fraction space can then easily be defined at these bounds, and they do not vary with time. The definition is valid only because mixture fraction is strictly conserved and cannot increase above one anywhere in the computational domain. In spray flames with pre-vapor, however, mixture fraction can be locally higher than the jet condition due to the evaporation process. Therefore, the upper bound of mixture fraction is defined as being pure fuel as given by the liquid droplets, and the mixture fraction transport equation therefore includes an evaporation source term as can be seen in Eqn. 2.31. Mixture fraction is not a fully conserved quantity, since the maximum value can vary in space and time, but cannot exceed $\xi = 1.0$ which would be equivalent to being a mixture of pure acetone. An alternative possible definition is to consider the sum of the fuel in the gaseous and liquid phase will lead to the definition of a fully conserved scalar [12]. This may facilitate the definition of the upper mixture fraction bound, but it will invoke different modelling challenges related to the correlation of the reactive species with this new mixture fraction. Also, the mixture fraction works with Eulerian-Eulerian approaches where liquid fuel is treated with a scalar transport equation, but a coupling with a Lagrangian approach is not straightforward. Thus, these fully conservative approaches are not pursued here.

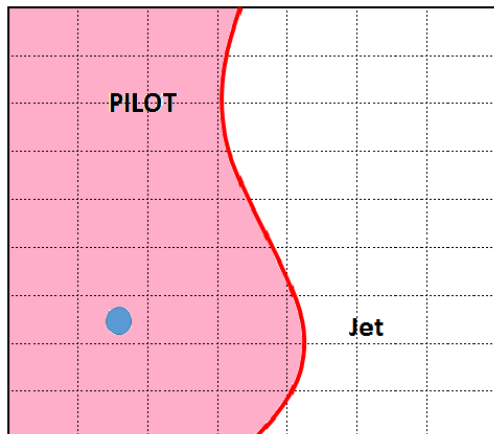
7.1.3 Boundary Condition in Mixture Fraction Space

In the present case some of the fuel is pre-evaporated leading to a rich mixture of $\xi_{jet} = 0.162$ exiting the jet, and the filtered mixture fraction can locally increase due to further evaporation of the droplets. Even though the range of mixture fraction space is specified, the upper bound of the mixture fraction, ξ_{UL} , must be properly set to solve the CMC equations. To illustrate the problem, consider a simplified unsteady zero-dimensional CMC equation,

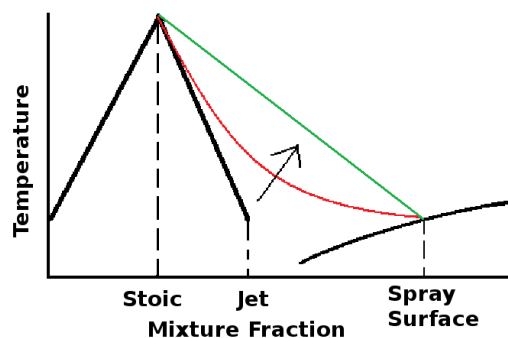
$$\frac{\partial Q_\alpha}{\partial t} = N_\eta \frac{\partial^2 Q_\alpha}{\partial \eta^2} + \omega_{\eta,\alpha}. \quad (7.1)$$

To solve the dissipation term (1st term on RHS), the range of the lower and upper mixture fraction boundaries must be specified. However, within a two-phase flow, ξ_{UL} depends on flow configurations and physical scales. As an example of a conceptual spray flame study, consider a CMC cell that contains a fuel jet with pre-evaporation and a liquid droplet located within a piloted flame as in Fig. 7.1(a). If there is no liquid droplet, the conditional temperature profile within the CMC cell would follow the black line in Fig. 7.1(b), and so $\xi_{UL} = \xi_{jet}$ in this case. On the other hand, with the presence of a liquid droplet, an LES cell in the pilot flame with the droplet can locally have a high mixture fraction at the surface of the droplet, such as $\xi_{UL} = \xi_{surf}$, and takes another conditional moment solution (the green line in Fig. 7.1(b)). However, there is only one conditional moment available within a CMC cell. If the mixing between the jet and pilot mixture fractions (the black line in Fig. 7.1(b)) is enforced, the high mixture fraction regime around the droplet follows the non-reacting solution. If the mixing between the droplet surface and pilot mixture fractions (the green line in Fig. 7.1(b)) is considered, $\xi_{UL} = \xi_{surf}$, and the temperature increases for $\eta = \xi_{jet}$ due to diffusion in mixture fraction space. This implies that the non-reacting solution cannot be preserved at ξ_{jet} , even though the droplet does not physically interact with the jet as in Fig. 7.1(a). Thus, in theory, one single droplet in the pilot suffices to raise the jet temperature since the reactive-diffusive balance (the first and second RHS-terms in Eqn. 4.11) is indepen-

dent of mixture fraction probabilities and cannot distinguish between one droplet with low probability and a spray of pure fuel with high probability. These modelling difficulties can be relaxed if there is no pre-evaporated fuel, such as spray ignition processes [20].



(a) Physical space representation. The large box with the bold line represents a CMC cell, and small boxes shown by dotted lines are LES cells. The left half (red zone) of the domain is reacting solution originated from a piloted flame, and the right half of the domain (white zone) is non-reacting gas from the jet. A blue circle represents a droplet.



(b) Mixture fraction space representation. The thick solid black line indicates the conditionally averaged temperature close to the jet exit, the curved black line indicates the droplet surface temperature as function of the equilibrium surface mixture fraction. The grey and black dashed lines illustrate the evolution of the conditional temperature due to diffusion in mixture fraction space.

Figure 7.1: Conceptual issues with mixture fraction boundaries in two-phase flows.

7.1.4 Conditioning of Spray Source Term

The conditioning of spray source terms are discussed in Sec. 4.3.3. Here, a more detailed discussion of the choice of the conditioning mixture fraction is given. Consider a zero dimensional unsteady CMC equation with the spray source term,

$$\frac{\partial Q_\alpha}{\partial t} = N_\eta \frac{\partial^2 Q_\alpha}{\partial \eta^2} + \omega_{\eta,\alpha} + \left[Q_{1,\alpha} - Q_\alpha - (1 - \eta) \frac{\partial}{\partial \eta} Q_\alpha \right] \Pi_\eta. \quad (7.2)$$

If the spray source term is conditioned on ξ_{surf} , the conditional evaporation rate can be written as

$$\Pi_\eta = \frac{\tilde{\Pi}\delta(\eta - \xi_{surf})}{\tilde{P}(\eta)}. \quad (7.3)$$

However, when the droplet temperature is high, ξ_{surf} might be a lot higher than the filtered mixture fraction, $\tilde{\xi}$, and the spray source term appears far away from the high probability regime in mixture fraction space as show in Fig. 7.2. It is obvious that there is a large gap between ξ_{surf} and the region with non-zero $P(\eta)$, and if the unconditional quantities are obtained by integrating Q_α with $P(\eta)$, the spray source term does not influence the unconditional moment at all, unless $P(\eta)$ is modified to account for the presence of the droplet. However, under the complex flow conditions, it is not feasible to estimate the right profile of $P(\eta)$ between $\tilde{\xi} < \eta < \xi_{surf}$.

Also, it is not clear how to model the transport of mass and heat in mixture fraction space from the relatively high mixture fraction ξ_{surf} to the usually much lower filtered mixture fraction $\tilde{\xi}$. Only the scalar dissipation can carry the effect of the spray source term to the lower mixture fraction regime. However, the correct conditionally averaged scalar dissipation needs to be known for the range of $\tilde{\xi} < \eta < \xi_{surf}$, but the necessary data are not available from LES-CMC. Recently, new models to describe the probability density function and scalar dissipation rate around stationary spherically symmetric droplets have been discussed [12], but with the presence of convective flows and turbulence, such idealized models are not directly applicable [96]. DNS of fully resolved evaporating droplets can provide this information [194], but validated models do not yet exist. The conditioning on the spray surface mixture fraction, ξ_{surf} , requires these two unsolved problems (the predictions of the FDF and N_η between $\tilde{\xi} < \eta < \xi_{surf}$), so this study conditions the spray source term on $\tilde{\xi}$. The validation of the approach is shown in the next section.

7.1.5 Validation of Two-Phase CMC in Cold Flow

The closure of the spray source terms in the CMC equation (4th term on the RHS of Eqn. 4.11) is examined by comparing CMC and LES solutions under the cold flow

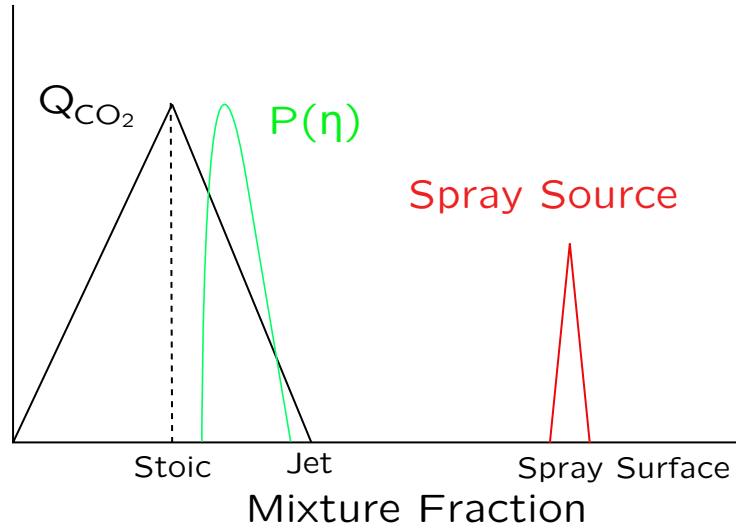


Figure 7.2: An example of spray source term conditioned on ξ_{surf} . Black line - conditional moment of CO_2 , red line - the spray source term (the third term of RHS in Eqn. 7.2) with Π conditioned on ξ_{surf} , green line - Probability within the CMC cell constructed by assumed PDF by $\tilde{\xi}$ and $\tilde{\xi}''^2$.

assumption (the reaction rate is zero) to clearly separate the effects of evaporation from reaction. To compute the LES solution of the acetone, an additional transport equation is solved, and it is given as

$$\frac{\partial}{\partial t}(\bar{\rho}\tilde{Y}_{ace}) + \frac{\partial}{\partial x_j}(\bar{\rho}\tilde{u}_j\tilde{Y}_{ace}) = -\frac{\partial \overline{J_{ace,j}}}{\partial x_j} - \frac{\partial J_{ace,j}^{sgs}}{\partial x_j} + \bar{\rho}_{ace}, \quad (7.4)$$

where \tilde{Y}_{ace} is the mass fraction of acetone, and closures are modelled as the mixture fraction transport equation (Eqn. 2.31). Fig. 7.3 compares the result of CMC and LES predictions. The lines represent the conditional Moment Q_{ace} , the dots represent the LES-filtered solution \tilde{Y}_{ace} . \tilde{Y}_{ace} can be obtained from Eqn. 2.31 in the case of this non-reacting acetone spray jet since it is then only different from mixture fraction due to different inflow boundary conditions (no acetone in the hot pilot). As can be seen, the conditional moment without the CMC spray source term ($\Pi_\eta = 0$) shows a large offset around $\xi = 0.15$, whereas the solution with the CMC spray source term closely follows the LES solution. It is also noted that the difference between the two conditional moments shown in Fig. 7.3 should not necessarily be

interpreted as a decrease of the conditionally averaged acetone mass fraction due to including Π_η in the CMC equation. It is rather a shift in mixture fraction space towards higher values due to evaporation and therefore increasing values of the underlying mixture fraction field (compare also the analysis in Appendix B).

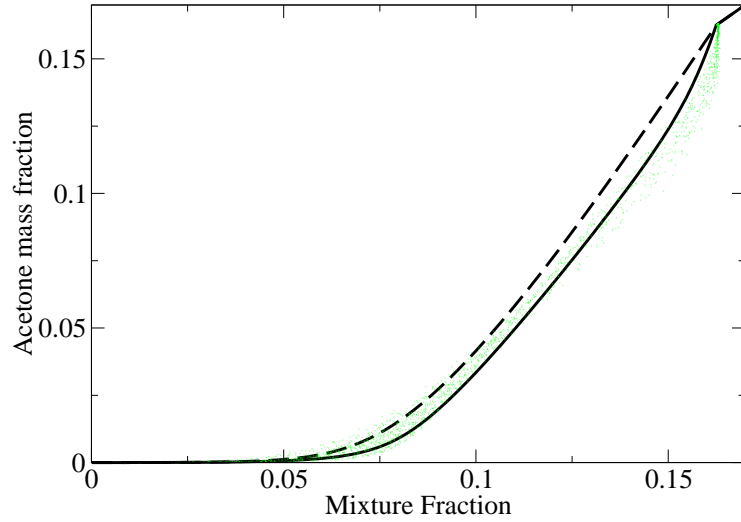


Figure 7.3: Comparison of acetone mass fraction in mixture fraction space at $z/D=5$. Solid line - CMC spray source terms on; dashed line - CMC spray source terms off; scattered green dots - solution of Eqn. 2.31 for acetone with the LES-filtered spray source term on.

7.1.6 Implementation of the Two-Phase LES-CMC

Figure 7.4 summarizes the sequence of the numerical approaches used in this chapter. Boffin provides the flow and mixing fields that is used to solve the spray formulations and CMC equations. Also, the FDF within each cell is computed by mean and variance of mixture fraction, and the LES quantities are computed by integrating along the conditional moments provided by CMC. Then, the unconditioned quantities and spray source terms are applied to update flow fields for the next time step.

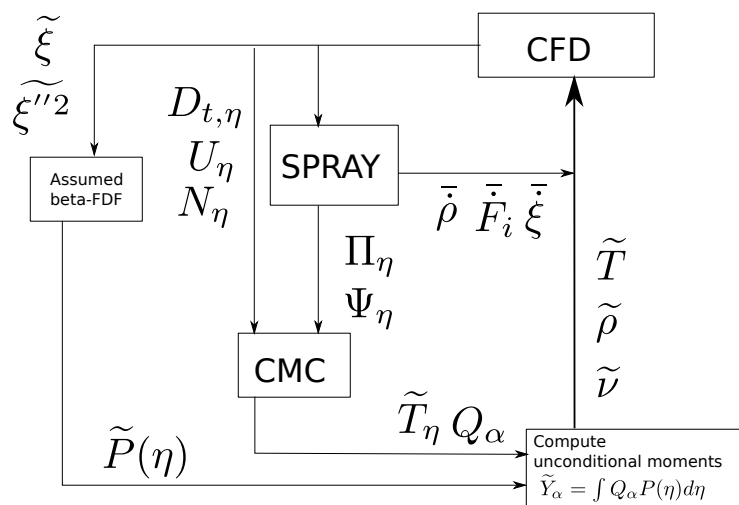


Figure 7.4: Flowchart of the conventional CMC approach in two-phase flows.

7.2 Results and Discussion

The effects of the evaporation source terms are now examined for the LES-CMC simulations of a reacting acetone spray flame. Here, AcF 3 from Table 5.1 is chosen as a reference case, and the numerical configurations are given in Sec. 5.3. First, the effect of the CMC spray source terms, Π_η and Ψ_η on the conditional moments is analyzed. Then, the method is evaluated by comparison of the unconditional temperature and spray velocity statistics with the experimental data from Masri and co-workers [113].

7.2.1 Conditional Moment

The conditionally averaged mass fractions of acetone and CO_2 obtained from the solution of Eqs. 4.11 and 4.12 are shown Fig. 7.5. Results have been obtained for cases where Π_η and Ψ_η are modelled and for cases where these terms have been neglected. As discussed above, the inclusion of the CMC spray source shifts Q_{ace} towards higher mixture fraction values. As expected, all conditionally averaged species and temperature (see Fig. 7.6) are hardly affected by evaporation on the lean side. The spray source terms will only affect mixture fraction ranges on the rich side of stoichiometric. Droplets evaporate predominantly in regions where the

filtered mixture fractions are larger than stoichiometric since the flame is piloted and fully burning, and droplets are unlikely to cross the stoichiometric contour (see Fig. 7.8). Consistent with lower conditional acetone mass fractions on the rich side are increased product mass fractions and temperature. The inner flame structure around stoichiometric does not seem to be affected at positions closer to the jet, but further downstream, a clear shift of the maximum temperature away from the stoichiometric value towards higher mixture fraction values can be observed. The reduction of the maximum temperatures by 4K ($x/D=10$) and 24K ($x/D=30$) can be associated with the energy transfer between droplets and gas phase that is modelled in the CMC equations by Ψ_η .

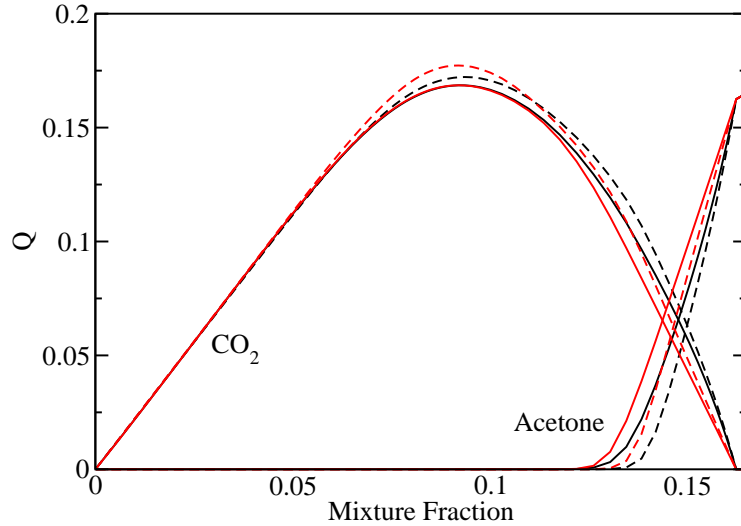


Figure 7.5: Comparison of Q_{CO_2} and Q_{Ace} . Solid line - $z/D=10$, dashed line - $z/D=30$, black line - with spray source terms, red line - without spray source terms.

7.2.2 Unconditional Moment

Temperature profiles at selected planes are compared to experimental values in Fig. 7.7. At $z/D=10$, both numerical results with and without CMC spray source terms predict the flame to be shifted slightly inward. Further downstream, the case with the CMC spray source term shows better agreement in the radial location and in peak temperature. As seen from the conditional moment, the CMC spray source

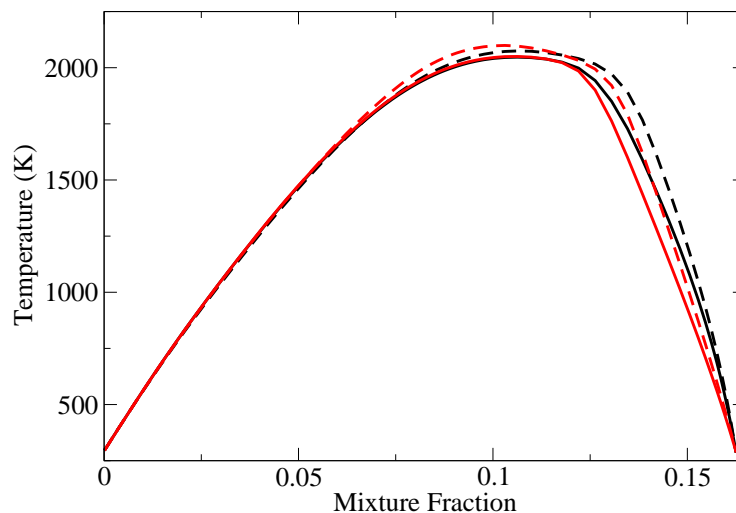


Figure 7.6: Temperature profile over mixture fraction. Solid line - $z/D=10$, dashed line - $z/D=30$, black line - with spray source terms, red line - without spray source terms.

makes the high mixture fraction regime more “reacted”. Therefore, the peak location is found to be shifted inwards, towards richer mixtures, consistent with the trend of the conditional temperature in Fig. 7.6. At $z/D=30$, the conditional moment also suggests a temperature shift to higher mixture fractions due to the CMC spray source terms, and the unconditional average exhibits the temperature peak slightly inward, at a larger mixture fraction. However, it can be observed that the centerline temperature is underpredicted. This is most probably caused by the choice of boundary condition. As discussed in Sec. 7.1.3, the mixture fraction space above the upper bound, $\xi > \xi_{jet}$, is fixed to the cold solution to keep the jet non-reactive. In reality, the upper mixture fraction bound may shift based on the spray evaporation, and the conditional average at this bound will change with downstream position reflecting diffusion of heat and products into the jet core. Similar trends can be observed in Fig. 7.8. The jet core stays at low temperature at all axial position since the evaporation maintains the relatively high mixture fraction values in regions close to the centerline. However, this conventional CMC approach can only describe on conditional moment even though it is not sufficient. Alternative approaches to improve these shortcomings are proposed in Chapters 8 and 9.

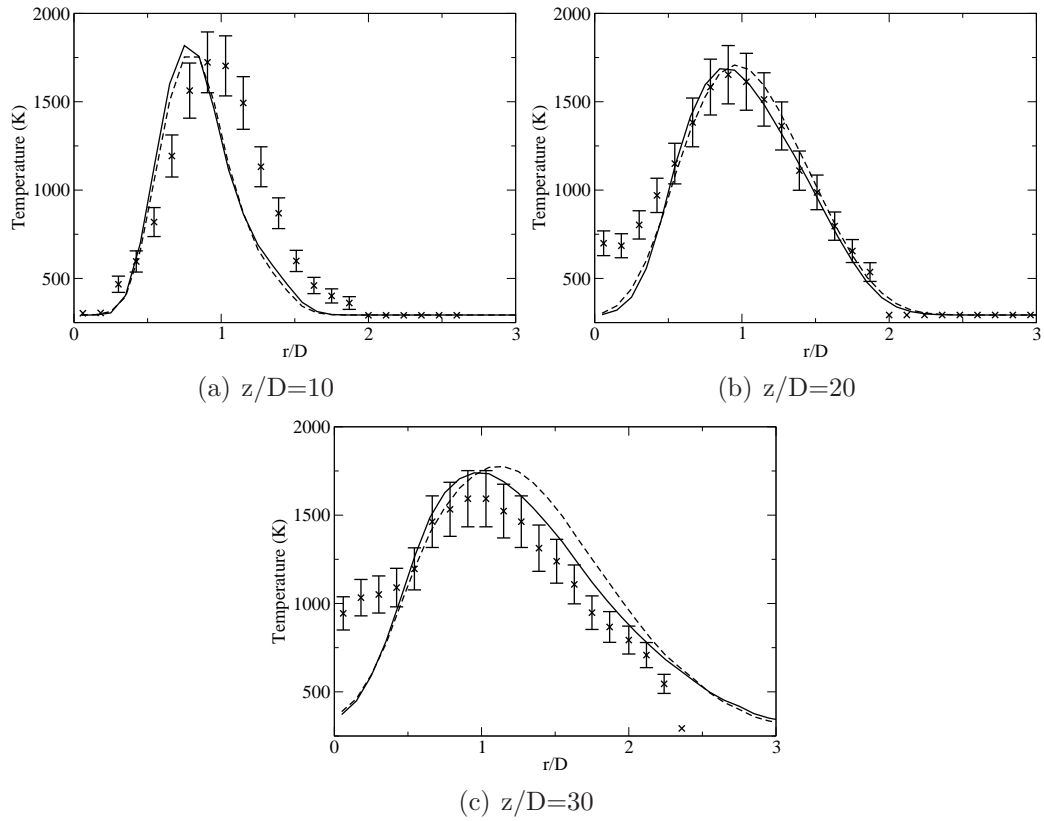


Figure 7.7: Radial profiles of mean temperature. Crosses - experiments [113], solid line - with spray source terms, dashed line - without spray source terms.

7.2.3 Spray Statistics

Mean and rms of the axial spray droplet velocity at $z/D=10$ are compared to the experiments in Fig. 7.9(a). The mean velocity profiles from the simulations both agree well with the experimental data, with the trend of a slight underprediction at the centerline and an overprediction near $r/D=1$ which is consistent with the slight temperature discrepancies seen in Fig. 7.7(a). The rms velocities near the centerline are captured well, particularly by the simulation with the spray source terms, whereas the rms is underpredicted at higher radii. Comparisons of downstream velocities at $z/D=20$ (Fig. 7.9(b)) indicates that the numerical predictions tend to underpredict mean velocities near the centerline. The effects of the stochastic dispersion and evaporation models are examined in Fig. 7.10. The stochastic models do not show large impact on the spray statistics as present in non-reacting analysis

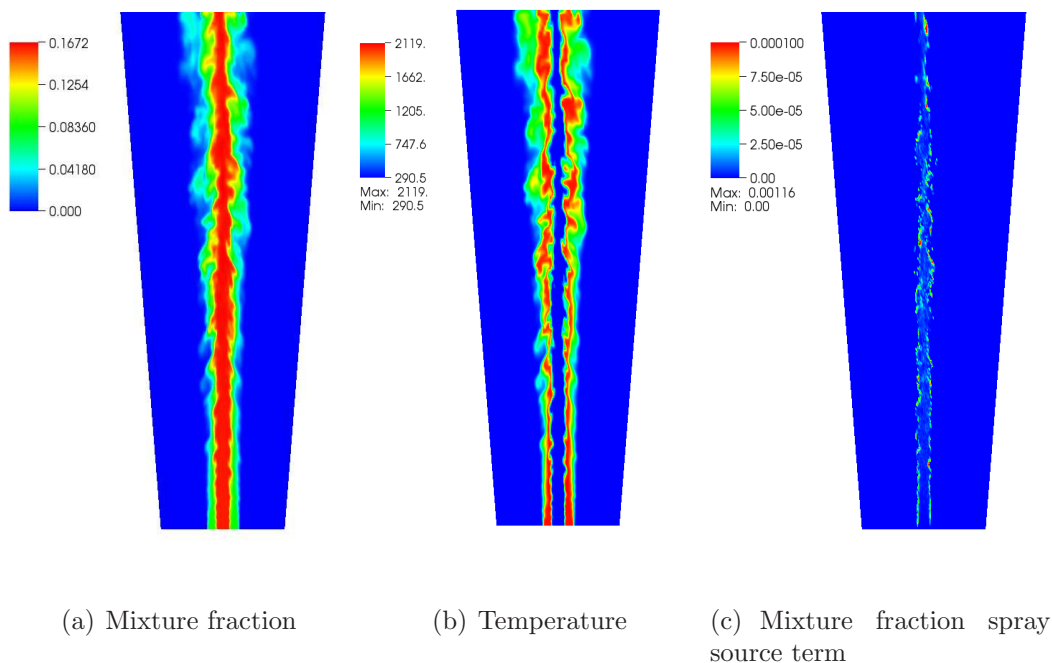


Figure 7.8: Instantaneous contour plot of AcF3 with conventional CMC.

(Sec. 6.2), and still exhibit the same problem: low velocity along the centerline and small rms at outer radii. The low velocity can be attributed to the lack of predicted thermal expansion in these regions. A possible reason of the small rms is further discussed in a later section with multiple cases (see Sec. 8.2.3).

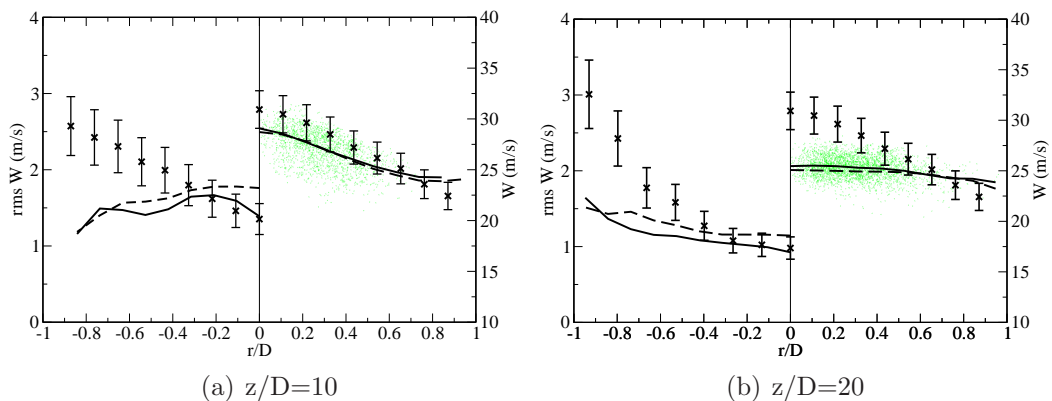


Figure 7.9: Mean (right) and rms (left) axial droplet velocity profiles for the diameter range $20\text{-}30\ \mu\text{m}$. Crosses - experiments [113], green scatter points - single realization of a simulated droplet, black line - with spray source terms, line - without spray source terms.

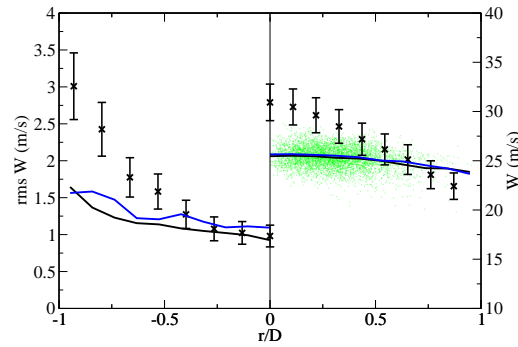


Figure 7.10: Mean (right) and rms (left) axial droplet velocity profiles for the diameter range $20\text{-}30\ \mu\text{m}$ at $z/D=20$. Crosses - experiments [113], green scatter points - single realization of a simulated droplet, black line - with spray source terms, blue line - with spray source terms and stochastic spray terms.

7.3 Summary

This chapter presents simulations of evaporating spray flames with LES-CMC. The CMC source terms due to evaporation that has often been neglected in earlier CMC studies, have now been modelled within the LES framework, and some conceptual difficulties with respect to the correct choice of boundary conditions are discussed. The closures of CMC spray terms are first validated by comparison of an LES-filtered solution for acetone with the CMC solution for a non-reacting jet. The computations of the acetone spray flames show that the CMC spray source terms shift the reacting solution to higher mixture fraction values, and inclusion of the CMC spray sources should not be neglected. The consistent CMC model gives very good agreement of predicted and measured temperatures, with the only exception of some locations near the centerline. This can mainly be attributed to the selected boundary conditions that are implemented to avoid the prediction of an unphysical heating of the jet near the nozzle. The predictions of the mean and rms axial velocity distribution are good at $x/D=10$, but at the downstream position ($x/D=20$), low mean velocities are predicted. The low velocities are attributed to the low temperature predictions along the centerline that reduce the velocity of the flow by lower heat expansion rates. No noticeable differences are observed in spray statistics between CMC with and without spray terms. Also, the stochastic particle dispersion

and evaporation models do not influence the spray statistics as shown in the non-reacting study in Chapter 6.

The main reason for the very localized low temperature prediction and low mean velocity profiles can be associated with the selection of the upper mixture fraction boundary in CMC equation as $\xi_{UL} = \xi_{jet}$. However, within the conventional CMC framework, it is difficult to model the upper bound appropriately. Therefore, two different approaches are proposed: two-conditional moment approach in Chapter 8 and CMC with tabulated chemistry in Chapter 9.

Chapter 8

Two-Conditional Moment Approach

In the previous Chapter, two-phase LES-CMC has been applied to a dilute acetone spray jet flame, and the impact of the additional spray terms has been discussed. However, “conventional” CMC indicates difficulties of selecting an appropriate upper limit of mixture fraction, ξ_{UL} , due to the evaporating droplets. In general, a single-phase CMC implementation (or non-premixed approaches in general) assumes ξ_{UL} to be fixed according to the fuel condition. However, the maximum mixture fraction varies in space and time due to evaporation, and it is difficult to define a single upper limit applicable throughout the entire domain. One compromise has been applied in Chapter 7 where ξ_{UL} has been fixed to be equal to the fuel jet mixture fraction ξ_{jet} originating from pre-evaporation inside the jet nozzle. This approach leads to a good match of the predictions with experiments near the jet inlet where most of the evaporation occurs without any mixing with the surrounding streams. However, the assumption is not fully valid where droplet vapour and oxidizer are mixed more homogeneously, and, as a result, low temperature regimes have been wrongly observed along the centerline further downstream. An alternative approach is to adjust ξ_{UL} dynamically based on the mixing fields, and better predictions can be expected downstream. However, if only the dynamically moving ξ_{UL} is used, the scalar dissipation can cause unphysical mixing in the jet core where mixing with the

surrounding flow should not occur (see Sec. 7.1.3). Thus, a new method must be developed to treat evaporating sprays more appropriately.

This chapter aims to develop a two-conditional moment approach that can deal with a shift of ξ_{UL} dynamically that accounts for the existence of pre-evaporated fuel by introducing two sets of conditional moments based on two different definitions of mixture fraction [176]. First, the formulations of the two-conditional moment approach are presented. Then, the conditional fluctuations and dynamically moving upper mixture fraction boundary caused by the evaporation process are demonstrated, and modelling approaches are discussed using a test case with a non-reacting evaporating spray jet in Sec. 8.1. Then, the effect of the modelling approach using two-conditional moments is analyzed and discussed, and the improved numerical predictions are compared with the experimental results in Sec. 8.2.

8.1 Two-Conditional Moment Approach

Chapter 7 discusses modelling limitations of the upper mixture fraction boundaries. A compromise is found by fixing the upper bound at the jet condition, but in reality, the mixture fraction changes due to the evaporation process, and the nominal upper mixture fraction boundary changes with time and position. Also, the evaporation process can violate the assumption of small conditional fluctuations in mixture fraction space. Therefore, not one but two conditional moments are computed that represent the extrema, and an interpolation routine is implemented to determine a suitable average of the two.

8.1.1 Formulations

Here, two definitions of mixture fraction are introduced: the total mixture fraction, ξ_{tot} , and the conserved mixture fraction, ξ_{cons} . ξ_{tot} represents the mixture fraction associated with the inlet conditions (a pilot flame and fuel originating from pre-evaporated droplets that lead to fuel vapour at the jet exit) *and* fuel originating from droplet evaporation within the domain. ξ_{cons} is based on the fuel from pre-

evaporation within the nozzle and the fuel elements of the pilot flame. ξ_{cons} is not affected by the fuel evaporating from the droplets within the domain. Solving these two mixture fractions, the mixture fraction evaporated from the droplets after exiting the nozzle can be computed as $\xi_{\Delta} = \xi_{tot} - \xi_{cons}$, and it plays an important role in the following modelling approach. The maximum value of ξ_{tot} changes dynamically and is defined to be unity when the mixture is pure fuel. The maximum value of ξ_{cons} corresponds to the maximum inlet mixture fraction. The Favre-filtered scalar transport equations for these mixture fractions are

$$\frac{\partial}{\partial t}(\bar{\rho}\tilde{\xi}_{tot}) + \frac{\partial}{\partial x_j}(\bar{\rho}\tilde{u}_j\tilde{\xi}_{tot}) = -\frac{\partial\overline{J_{tot,j}}}{\partial x_j} - \frac{\partial J_{tot,j}^{sgs}}{\partial x_j} + \bar{\xi}, \quad (8.1)$$

$$\frac{\partial}{\partial t}(\bar{\rho}\tilde{\xi}_{cons}) + \frac{\partial}{\partial x_j}(\bar{\rho}\tilde{u}_j\tilde{\xi}_{cons}) = -\frac{\partial\overline{J_{cons,j}}}{\partial x_j} - \frac{\partial J_{cons,j}^{sgs}}{\partial x_j}. \quad (8.2)$$

The CMC equations usually assume that the conditional fluctuations within the flow are relatively small. However, in practice, the conditional fluctuations can be very large for spray flames, and it might be impractical to represent the properties by only one conditional moment as discussed in Sec. 8.1. Therefore, two sets of conditional moments conditioned on ξ_{cons} and ξ_{tot} are solved simultaneously, and the solution is obtained by interpolation between the two conditional moments as presented later. Based on Eqn. 4.11, the CMC equations for moments conditioned on the total mixture fraction can be written as

$$\begin{aligned} \frac{\partial}{\partial t}Q_{\alpha,tot} &+ \frac{1}{\bar{\rho}_{\eta,tot}\tilde{P}_{\eta,tot}}\nabla\cdot[\bar{\rho}_{\eta,tot}\tilde{P}_{\eta,tot}(U_{\eta,tot}Q_{\alpha,tot} - D_{t,\eta,tot}\nabla Q_{\alpha,tot})] \\ &= \tilde{\omega}_{\eta,\alpha,tot} + N_{\eta,tot}\frac{\partial^2 Q_{\alpha,tot}}{\partial\eta^2} + \frac{Q_{\alpha,tot}}{\bar{\rho}_{\eta,tot}\tilde{P}_{\eta,tot}}\nabla\cdot(\bar{\rho}_{\eta,tot}\tilde{P}_{\eta,tot}U_{\eta,tot}) \\ &+ \left[Q_{1,\alpha} - Q_{\alpha,tot} - (1-\eta)\frac{\partial}{\partial\eta}Q_{\alpha,tot}\right]\Pi_{\eta}, \end{aligned} \quad (8.3)$$

where the subscript $-tot-$ indicates conditioning on the random variable ξ_{tot} and all conditional properties in Eqn. 8.3 are conditioned on ξ_{tot} . Similarly, the CMC

equations for moments conditioned on the conservative mixture fraction is

$$\begin{aligned} \frac{\partial}{\partial t} Q_{\alpha,cons} &+ \frac{1}{\bar{\rho}_{\eta,cons} \tilde{P}_{\eta,cons}} \nabla \cdot [\bar{\rho}_{\eta,cons} \tilde{P}_{\eta,cons} (U_{\eta,cons} Q_{\alpha,cons} - D_{t,\eta,cons} \nabla Q_{\alpha,cons})] \\ &= \tilde{\omega}_{\eta,\alpha,cons} + N_{\eta,cons} \frac{\partial^2 Q_{\alpha,cons}}{\partial \eta^2} + \frac{Q_{\alpha,cons}}{\bar{\rho}_{\eta,cons} \tilde{P}_{\eta,cons}} \nabla \cdot (\bar{\rho}_{\eta,cons} \tilde{P}_{\eta,cons} U_{\eta,cons}), \end{aligned} \quad (8.4)$$

where the subscript $-cons-$ means conditioning on the random variable ξ_{cons} . Note that since the transport equations of ξ_{cons} does not have a spray evaporation term (Eqn. 8.2), no CMC spray source term is included in Eqn. 8.4. The conditionally averaged enthalpy equations are given by (see Eqn. 4.12)

$$\begin{aligned} \frac{\partial}{\partial t} Q_{h,tot} &+ \frac{1}{\bar{\rho}_{\eta,tot} \tilde{P}_{\eta,tot}} \nabla \cdot [\bar{\rho}_{\eta,tot} \tilde{P}_{\eta,tot} (U_{\eta,tot} Q_{h,tot} - D_{t,\eta,tot} \nabla Q_{h,tot})] \\ &= N_{\eta,tot} \frac{\partial^2 Q_{h,tot}}{\partial \eta^2} + \frac{Q_{h,tot}}{\bar{\rho}_{\eta,tot} \tilde{P}_{\eta,tot}} \nabla \cdot (\bar{\rho}_{\eta,tot} \tilde{P}_{\eta,tot} U_{\eta,tot}) \\ &+ e_{rad,\eta,tot} + \left[Q_{1,h} - Q_{h,tot} - (1 - \eta) \frac{\partial}{\partial \eta} Q_{h,tot} \right] \Pi_{\eta} + \Psi_{\eta}, \end{aligned} \quad (8.5)$$

and

$$\begin{aligned} \frac{\partial}{\partial t} Q_{h,cons} &+ \frac{1}{\bar{\rho}_{\eta,cons} \tilde{P}_{\eta,cons}} \nabla \cdot [\bar{\rho}_{\eta,cons} \tilde{P}_{\eta,cons} (U_{\eta,cons} Q_{h,cons} - D_{t,\eta,cons} \nabla Q_{h,cons})] \\ &= N_{\eta,cons} \frac{\partial^2 Q_{h,cons}}{\partial \eta^2} + \frac{Q_{h,cons}}{\bar{\rho}_{\eta,cons} \tilde{P}_{\eta,cons}} \nabla \cdot (\bar{\rho}_{\eta,cons} \tilde{P}_{\eta,cons} U_{\eta,cons}) + e_{rad,\eta,cons}. \end{aligned} \quad (8.6)$$

The closures for the conditionally averaged quantities are explained and discussed in Chapter 4, and the current study considers that these terms are identical for both the formulations of Q_{tot} and Q_{cons} . The terms $\tilde{\omega}_{\eta,\alpha}$ and $e_{rad,\eta}$ are functions of each conditional moment, (e.g. $\tilde{\omega}_{\eta,\alpha,tot} = f(Q_{\alpha,\eta,tot}, T_{\eta,tot})$), so that $\tilde{\omega}_{\eta,\alpha,tot} \neq \tilde{\omega}_{\eta,\alpha,cons}$ and $e_{rad,\eta,tot} \neq e_{rad,\eta,cons}$.

8.1.2 LES Representations in Mixture Fraction Space

The evaporation within the domain can increase ξ_{tot} beyond ξ_{jet} , and the minimum ξ_{Δ} to reach a certain ξ_{tot} can be estimated. The effects of the evaporation ξ_{tot} , ξ_{Δ} and ρ are given as

$$\rho^{n+1}\xi_{tot}^{n+1} = \rho^n\xi_{tot}^n + \Delta\dot{\rho}, \quad (8.7)$$

$$\rho^{n+1}\xi_{\Delta}^{n+1} = \rho^n\xi_{\Delta}^n + \Delta\dot{\rho}, \quad (8.8)$$

$$\rho^{n+1} = \rho^n + \Delta\dot{\rho}. \quad (8.9)$$

where $\Delta\dot{\rho}$ refers the amount of the evaporation within the time step, Δt , found as $\Delta\dot{\rho} = \Delta t\dot{\rho}$ the superscript refers the time step. Assuming that the conditions at time step n are the jet inlet condition ($\xi_{tot} = \xi_{jet}$ and $\xi_{\Delta} = 0$), Eqns. 8.7 and 8.8 can be written as

$$\rho^{n+1}\xi_{tot}^{n+1} = \rho^n\xi_{jet} + \Delta\dot{\rho}, \quad (8.10)$$

$$\rho^{n+1}\xi_{\Delta}^{n+1} = \Delta\dot{\rho}. \quad (8.11)$$

Using Eqns. 8.9, 8.10 and 8.11, ξ_{Δ} can be given as (by omitting the superscript)

$$\xi_{\Delta} = \frac{\xi_{tot} - \xi_{jet}}{1 - \xi_{jet}}, \quad (8.12)$$

and it indicates the ‘‘minimum’’ ξ_{Δ} necessary to reach a certain ξ_{tot} . More generally, a base mixture fraction ξ_{base} is defined as the minimum amount of vapour emitted from the droplets, i.e.,

$$\begin{cases} \xi_{base} = 0 & \text{if } \xi_{tot} < \xi_{jet} \\ \xi_{base} = \frac{\xi_{tot} - \xi_{jet}}{1 - \xi_{jet}} & \text{if } \xi_{tot} \geq \xi_{jet} \end{cases}. \quad (8.13)$$

In other words, fluid originating from the jet and vapour originating from the liquid fuel exist along ξ_{base} for $\xi_{tot} \geq \xi_{jet}$, and mixing with the surrounding fluid (e.g. from the pilot or co-flow) has not yet occurred. These relationships are illustrated with the configuration of AcF 3 in Fig. 8.1, and it shows the mixture fraction originating from the droplets in the domain for two different CMC cells. Since there is no

mixing with the surrounding material, ξ_Δ within the jet core clusters near ξ_{base} , and the conditional fluctuation is relatively small. However, the samples from the CMC cell containing the jet core and the pilot show a wide distribution of ξ_Δ around $\xi_{tot} \approx 0.16$. It is obvious that a simple first order closure is not forthcoming with only one conditional moment since realizations along the base line must represent cold (or non-reacting) solutions but those with large ξ_Δ can be hot and thus, conditional fluctuations will not be negligible.

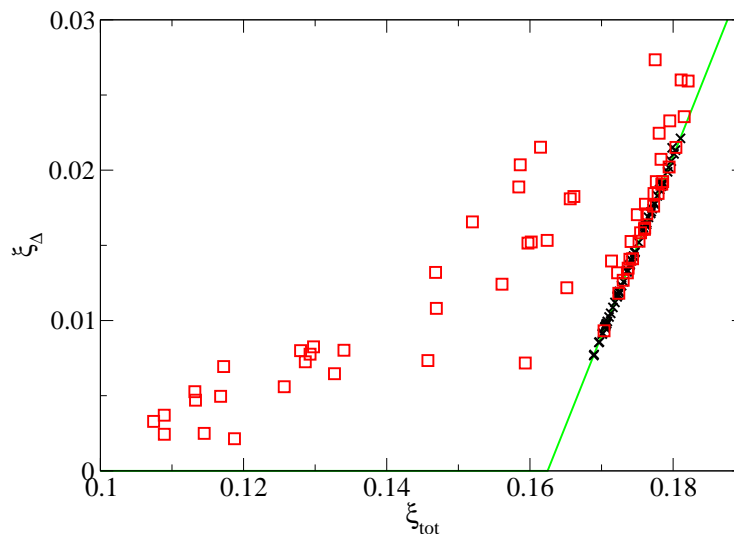


Figure 8.1: Realizations of $\tilde{\xi}_\Delta$ within a CMC cell that lies within the jet core (black) and a CMC cell at the interface of the jet core and the pilot (red). The green line is ξ_{base} (Eqn. 8.13). The condition is based on AcF 3 (Table 5.1).

8.1.3 Selection of Upper Mixture Fraction Boundary

The definition of the upper mixture fraction boundary has not been fully justified. Two possible characteristics (macro- and microscopic) of the boundary conditions are discussed in Secs. 7.1.3 and 7.1.4, and a compromise has been made to choose the jet mixture fraction as the boundary ($\xi_{UL} = \xi_{jet}$) in the previous chapter. Here, a new methodology is presented to determine ξ_{UL} from LES-filtered quantities. In a single phase flow, a non-reacting scalar mixes linearly between fuel and oxidizer in mixture fraction space. Thus, if a quantity of the conserved scalar, ϕ , at a certain

mixture fraction is known, the value of ϕ at the upper boundary, ϕ_{UL} , is given by

$$\phi_{UL} = \frac{\xi_{UL}}{\xi} \phi, \quad (8.14)$$

and the slope is denoted as a mixing line. Using a single phase flow as an analogy, ξ_{UL} must be unmixed with the surroundings. In other words, the solution must lie on the unmixed limit which is denoted as ξ_{base} in Eqn. 8.13. Thus, the current study proposes a new selection method of ξ_{UL} with the combination of the base mixture fraction and the mixing line as shown in Fig. 8.2. From the base mixture fraction (Eqn. 8.13), an amount of ξ_{Δ} at ξ_{UL} can be determined as

$$\xi_{\Delta, @ \xi_{UL}} = \frac{\xi_{UL} - \xi_{jet}}{1 - \xi_{jet}}, \quad (8.15)$$

and the linear mixing line as in Eqn. 8.14, (with $\phi_{UL} = \xi_{\Delta, @ \xi_{UL}}$ and $\phi = \tilde{\xi}_{\Delta}$) can be deduced,

$$\xi_{\Delta, @ \xi_{UL}} = \frac{\xi_{UL}}{\tilde{\xi}_{tot}} \tilde{\xi}_{\Delta}. \quad (8.16)$$

Thus, the upper mixture boundary in mixture fraction space, ξ_{UL} , is obtained as a pseudo-unmixed material and can be written as

$$\xi_{UL} = \frac{\xi_{jet}}{1 - \frac{\tilde{\xi}_{\Delta}}{\tilde{\xi}_{tot}} + \frac{\tilde{\xi}_{\Delta}}{\tilde{\xi}_{tot}} \xi_{jet}}. \quad (8.17)$$

8.1.4 Interpolation Method

The conditional moments in each LES cell, $Q_{\alpha, \eta}$, are needed to calculate the LES-filtered quantities, and they are estimated by interpolation between $Q_{\alpha, tot}$ and $Q_{\alpha, cons}$ depending on the amount of $\tilde{\xi}_{\Delta}$. It can be said that $Q_{\alpha, cons}$ is the solution along ξ_{base} , and $Q_{\alpha, tot}$ is approximately the solution along the conditional mean of the evaporated fuel $\langle \xi_{\Delta} | \eta \rangle$. Thus, when $\tilde{\xi}_{\Delta}$ is close to ξ_{base} , the solution must be close to $Q_{\alpha, cons}$, and large amounts of $\tilde{\xi}_{\Delta}$ should weight the solution towards $Q_{\alpha, tot}$ as shown

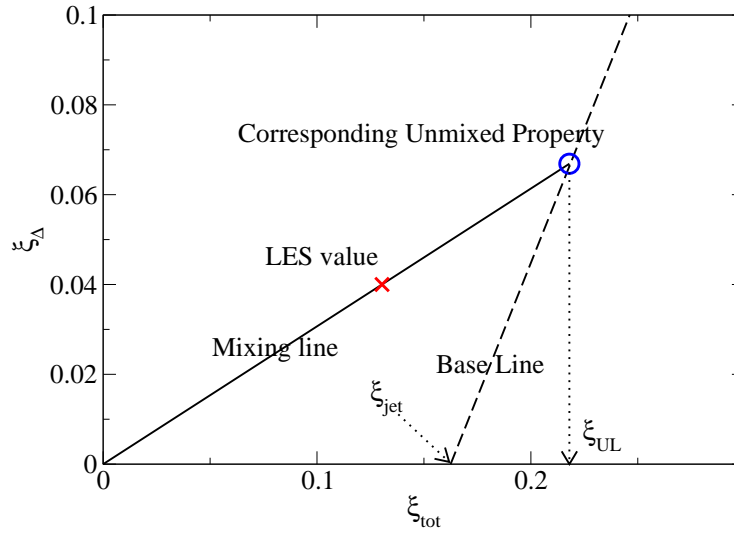


Figure 8.2: Estimation of ξ_{UL} . Cross - actual quantity in a LES cell ($\tilde{\xi}_{tot}$, $\tilde{\xi}_{\Delta}$), circle - (imaginary) unmixed property corresponding to the LES cell (ξ_{UL} , $\xi_{\Delta, @\xi_{UL}}$), solid line - mixing line, dashed line - ξ_{base} .

in Fig. 8.3. The weighting factor θ is given by

$$Q_{\alpha, \eta} = \theta Q_{\alpha, \eta, tot} + (1 - \theta) Q_{\alpha, \eta, cons}, \quad (8.18)$$

with

$$\begin{cases} \theta = \frac{\tilde{\xi}_{\Delta} - \xi_{base}}{\langle \xi_{\Delta} | \eta \rangle - \xi_{base}} & \text{if } \xi_{base} < \tilde{\xi}_{\Delta} < \langle \xi_{\Delta} | \eta \rangle \\ \theta = 1.0 & \text{if } \tilde{\xi}_{\Delta} > \langle \xi_{\Delta} | \eta \rangle \end{cases}. \quad (8.19)$$

As in the previous chapters, the unconditional moment is found by integrating the conditional moment across mixture fraction space using an assumed FDF (Eqn. 4.33). A β -function is often utilized as an assumed FDF (Eqn. 4.35) of the mixing field. However, considering that there is an upper bound of the mixture fraction space, a bounded β -FDF (Eqn. 4.38) is used to compute the LES-filtered quantities by using ξ_{UL} from Eqn. 8.17

$$\tilde{Y}_{\alpha} = \int_0^{\xi_{UL}} Q_{\alpha, \eta} P(\eta) d\eta. \quad (8.20)$$

by setting $\xi_{LL} = 0.0$. where $P(\eta)$ is the assumed FDF based on a bounded β -function. In an earlier study, Ge and Gutheil [62] have proposed the bounded β -

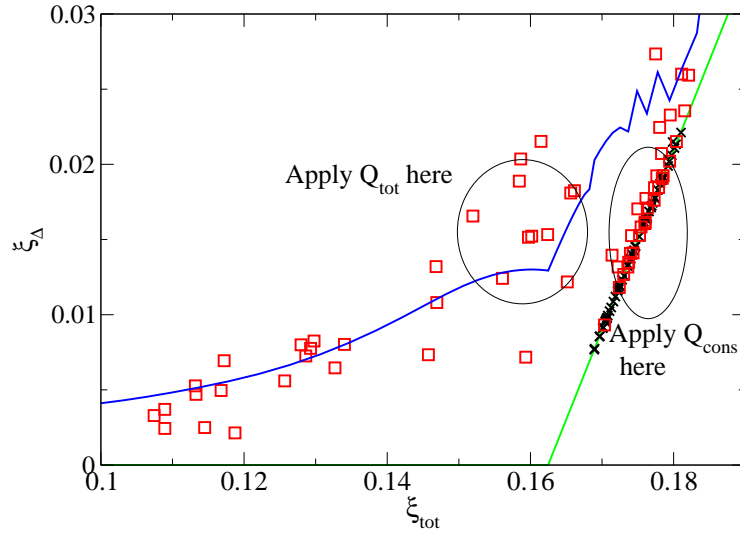


Figure 8.3: Realization of $\tilde{\xi}_\Delta$ in the CMC cell over the core (black crosses) and the pilot (red square) with $\langle \xi_\Delta | \eta \rangle$ (blue line). The green line is the base mixture fraction (Eqn. 8.13).

FDF, but the drawback is that the clear definition of ξ_{UL} and ξ_{LL} were not specified, but rather selected to fit the profile.

Currently, $P(\eta)$ is assumed to be based on ξ_{tot} instead of ξ_{cons} by considering two limiting cases of θ in Eqn. 8.18. Firstly, if $\theta = 1.0$, $Q_{\alpha,\eta}$ is only based on $Q_{\alpha,\eta,tot}$, and ξ_{tot} is an appropriate choice to obtain $P(\eta)$. Secondly, if $\theta = 0.0$, $Q_{\alpha,\eta}$ is only based on $Q_{\alpha,\eta,cons}$, and the $P(\eta)$ should be rather based on ξ_{cons} . However, when $\theta = 0.0$, $\xi_\Delta = 0$ as in Eqn. 8.19 so that $\xi_{tot} = \xi_{cons}$, and ξ_{tot} would be a good choice for $P(\eta)$. Since $P(\eta)$ can be correctly modelled by ξ_{tot} in these two limiting cases, an intermediate solution is assumed to follow $P(\eta)$ based on ξ_{tot} .

8.1.5 Comparisons of CMC and LES Solutions

This two-conditional moment approach is validated by comparing CMC solutions with the LES results for a non-reacting case as in Sec. 7.1.5. Here, an additional transport equation of Y_{ace} is solved to obtain LES-filtered solutions as in Sec. 7.1.5. The CMC solution is given by integrating the conditional moments as in Eqn. 8.20. Even though LES and CMC solutions are obtained by different methods, Fig. 8.4

shows that the distributions of Y_{ace} within a CMC cell seem to agree very well. It indicates that the two-conditional moment approach is capable of modelling an evaporating spray with pre-evaporated fuel. If only one set of conditional moments is used, the LES solution cannot be reproduced.

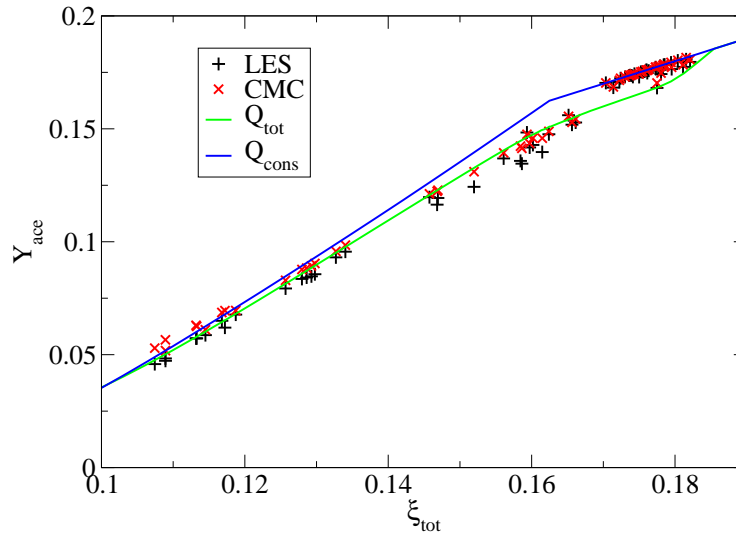


Figure 8.4: Realization Y_{ace} of LES (black plus symbol) and CMC (red X symbol) solutions over profiles of $Q_{ace,tot}$ (green line) and $Q_{ace,cons}$ (blue line).

8.1.6 Implementation of the Two-Conditional Moment Approach

The overall flowchart of the two-conditional moment approach is shown in Fig. 8.5. It is basically similar to Fig. 7.4, but there are a few improvements. First, the FDF is computed by using the bounded β -function, instead of the conventional β -function. Secondly, two sets of CMC equations are solved instead of only one. Then, finally, the conditional moments are computed by interpolating two conditional moments for each LES cell by using the weighting factor to obtain the unconditional quantities integrating along the subgrid FDF.

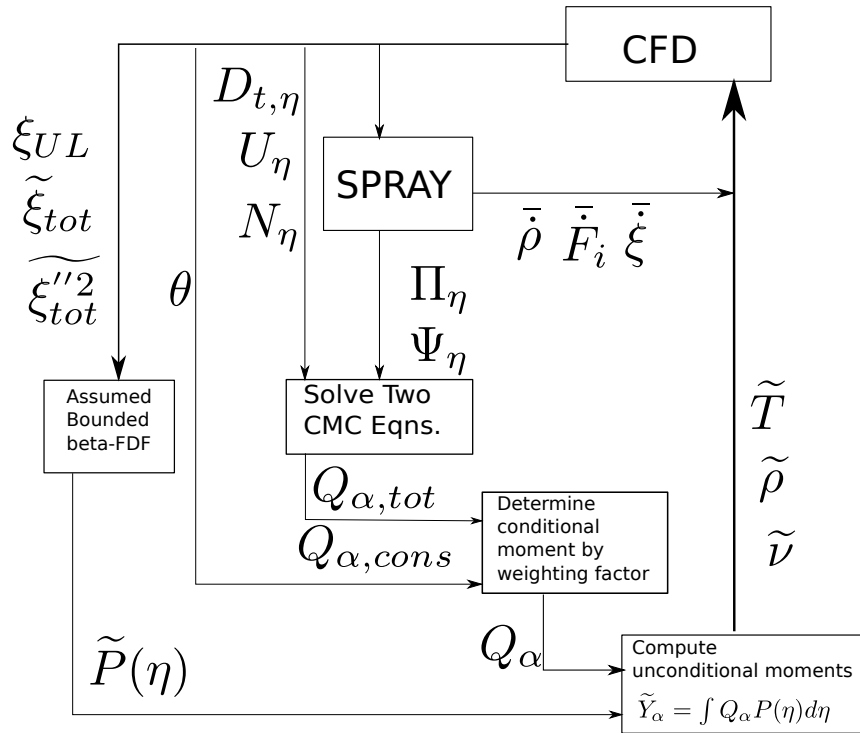


Figure 8.5: Flowchart of the two-conditional moment approach.

8.2 Results and Discussion

In this section, the two-conditional moment approach is tested for the four spray flame cases: AcF 1, 2, 3, and 5 introduced in Table 5.1, and the computational configurations are explained in Sec. 5.3. The results of conditional moment profiles, unconditional moments and spray statistics are discussed.

8.2.1 Conditional Moment

The conditional moments of acetone and OH for different locations in flame AcF 3 are shown in Fig. 8.6. It is apparent that the upper bound of $Q_{ace,cons}$ is fixed at the value determined by the amount of pre-evaporation at the nozzle exit. In contrast, the upper bound of $Q_{ace,tot}$ moves towards higher values due to the evaporation of the droplets within the domain. The movement can be quite large in regions with high evaporation rates. However, note that the particle-source in cell model is implied, and the upper limit is determined by an LES averaged value, but not

by the maximum mixture fraction found at the (unresolved) surface of the droplet. While clear differences can be observed between $Q_{ace,tot}$ and $Q_{ace,cons}$, the differences between $Q_{OH,tot}$ and $Q_{OH,cons}$ are much less pronounced. This is due to an effective upper boundary of conditional OH close to 0.16 where OH mass fractions tend to zero, and any change beyond this value does not affect the conditional moment. The reaction zone is hardly affected by the moving boundary. However, diffusion in mixture fraction space is, and this will be discussed further below. Also, OH profiles are noticeably affected if the amount of pre-evaporation is lowered. Clear differences can be seen in Fig. 8.7 for AcF 5 where the amount of pre-evaporation is relatively low restricting the width of the reaction zone for the conditional moments conditioned on the conserved mixture fraction.

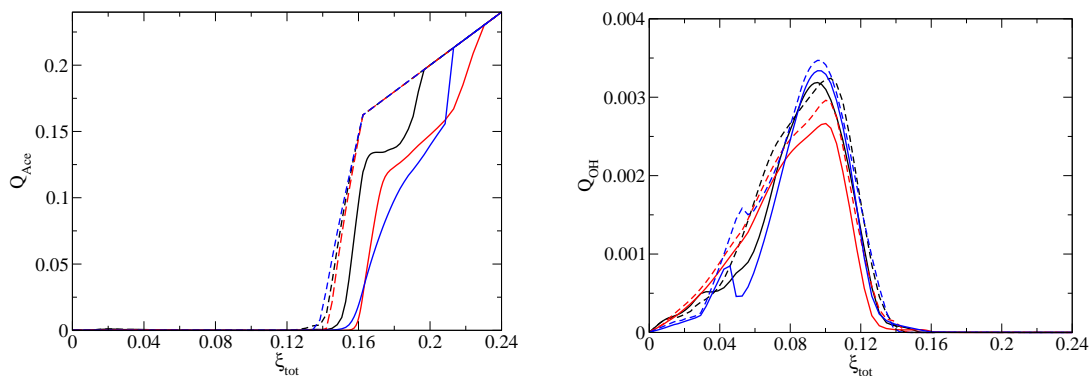


Figure 8.6: Instantaneous conditionally averaged mass fractions of acetone (left) and OH (right) in flame AcF 3. The center of each CMC cell is located ($r/D=0$, $z/D=10$) - black, ($r/D=0$, $z/D=20$)- red and ($r/D=0.8$, $z/D=20$) -blue. Solid line - Q_{tot} , dashed line - Q_{cons} .

Fig. 8.8(a) compares the distribution of $(\tilde{\xi}_{\Delta} - \xi_{base})$ (on the LES grid) and $(\langle \xi_{\Delta} | \eta \rangle - \xi_{base})$ (on the CMC grid) to determine the effect of the weighting factor as introduced in Eqn. 8.19. The corresponding temperature profiles are shown in Fig. 8.8(b). Since some of the fluid elements from the jet remain unmixed at ($r/D=0$, $z/D=10$), the difference $(\tilde{\xi}_{\Delta} - \xi_{base})$ equals zero around ξ_{jet} and consequently, some of the LES temperature solutions are found to lie on $T_{\eta,cons}$. However, solutions along $T_{\eta,tot}$ also exist within the same CMC cell and the majority of LES realizations (crosses) lie between these two values. It is therefore important to dis-

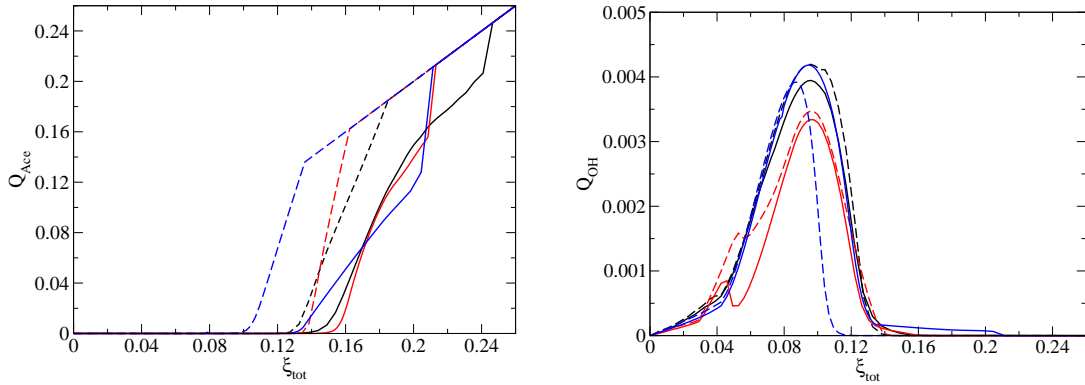


Figure 8.7: Instantaneous conditionally averaged mass fraction of acetone (left) and OH (right) at $(r/D=0.8, z/D=20)$ for the different flames. Black - AcF 2, red - AcF 3 and blue - AcF 5. Solid line - Q_{tot} , dashed line - Q_{cons} .

tinguish between the two CMC solutions and to obtain an accurate LES-filtered value by using an appropriate weighting factor θ for Q_α which is then used in Eqn. 8.20. More mixing with the surrounding fluid elements occurs further downstream, and no unmixed elements can be found at $(r/D=0, z/D=20)$. Despite the mixing, however, large fluctuations of $(\tilde{\xi}_\Delta - \xi_{base})$ can be observed leading to large conditional fluctuations in the temperature profiles. At the position $(r/D=0.8, z/D=20)$ a relatively wide range of mixture fraction values can be seen due to the mixing of jet and pilot and continuous evaporation of the fuel. The conditional fluctuations around $(\langle \xi_\Delta | \eta \rangle - \xi_{base})$ are, however, small such that the temperature profiles can be well approximated by one conditional moment $T_{\eta,tot}$ only. Note that $(\langle \xi_\Delta | \eta \rangle - \xi_{base})$ can be non-zero for certain mixture fraction values even if none of the LES realizations provides this value of $\tilde{\xi}_{tot}$ within the CMC cell. This is due to the subgrid fluctuations of mixture fraction that are included via weighting with the β -FDF when computing $\langle \xi_\Delta | \eta \rangle$ (see also [132]).

8.2.2 Unconditional Moment

Computed profiles of the unconditionally averaged temperature are compared with experiments in Fig. 8.9. The comparisons of the two-conditional moment approach and the conventional one-moment (or “conventional”) approach used in Chapter 7

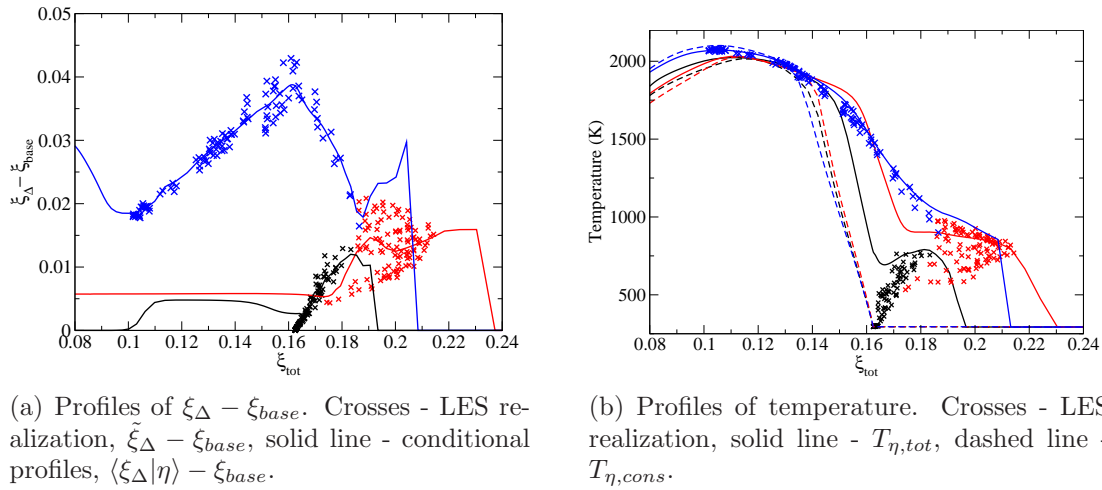


Figure 8.8: Instantaneous LES values and conditional moments plotted over mixture fraction for different CMC cells in flame AcF 3. The centers of the CMC cells are located at $(r/D=0, z/D=10)$ – black; $(r/D=0, z/D=20)$ – red; $(r/D=0.8, z/D=20)$ – blue.

are shown for AcF 3. Very low temperatures are observed near the centerline when using one moment only as similarly observed in the previous Chapter (Fig. 7.7), since the upper mixture fraction bound was fixed at ξ_{jet} and the temperature rise in rich mixtures along the centerline cannot possibly be predicted. The two-conditional moment approach predicts the increase of centerline temperature successfully. Similarly, AcF 1 shows good agreement at all three positions. AcF 2 follows the experiments relatively well, except a continuous under- and overprediction of temperature at the centerline. It may be possible to improve the predictions somewhat by tuning of the LES inflow and boundary conditions, but this is not attempted here (see also discussion in Sec. 8.2.3). Computations of AcF 5 also show rather good agreement with the experimental results. A large offset is seen close to the centerline at $z/D=10$, but the accuracy of the measurements may be questioned here since the steep slope at $r/D \approx 0.2$ does not seem physical. The numerical predictions generally agree well with the experimental results, but slight overpredictions of temperature are consistently found especially at downstream positions. It is noted, however, that the predictions presented here are very competitive in terms of quantitative agreement with experiments when compared with predictions of these and similar flames

presented in the literature [38, 37, 77, 46].

Figure 8.10 shows instantaneous snapshots of AcF 3. It is seen that ξ_{tot} increases due to evaporation at the centerline. Also, the largest ξ_{tot} found within the domain is 0.2587 whereas the largest ξ by the conventional CMC is only 0.167 (Fig. 7.8). On the other hand, ξ_{cons} does not have any source term, and it only decreases towards the outlet. Thus, relatively large ξ_{Δ} exists downstream, and the effect of the two-conditional moment approach becomes effective. The temperature increases where ξ_{Δ} is non-zero, whereas the conventional CMC yields low temperatures along the centerline down to the outflow boundary.

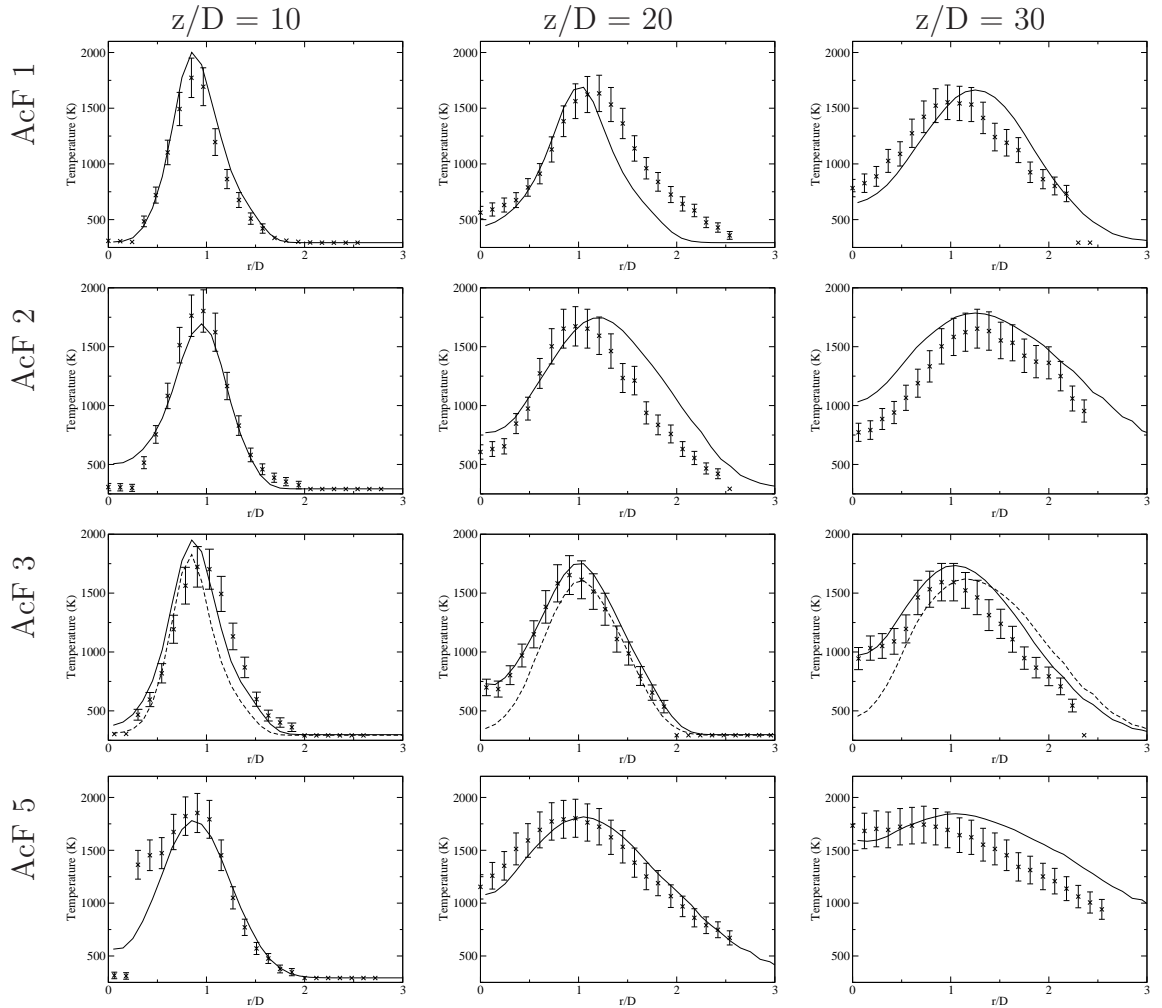


Figure 8.9: Radial profiles of mean temperature. Crosses - experiments [113], solid line - the two-conditional moment approach, dashed line - one-conditional moment approach.

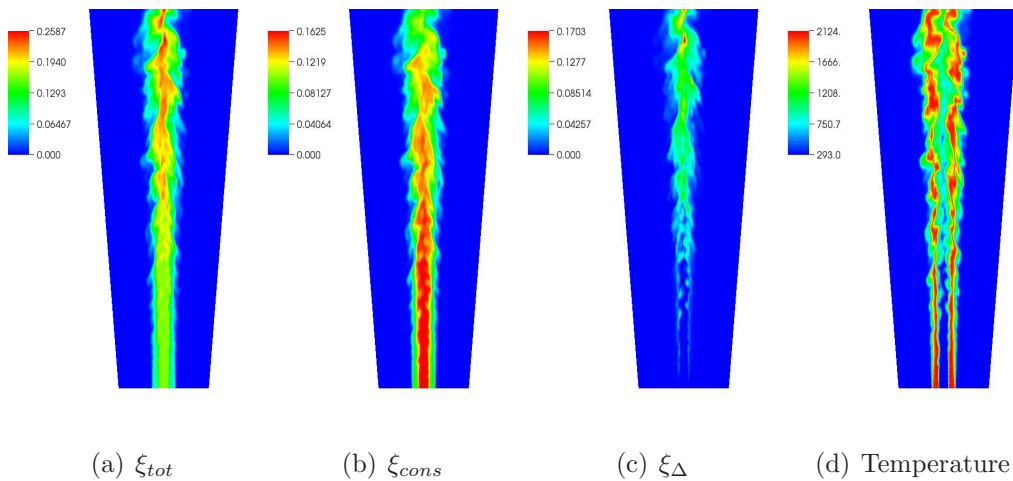


Figure 8.10: Instantaneous Contour plot of AcF3 with the two-conditional moment approach.

8.2.3 Spray velocity statistics

The computed spray axial velocity statistics are compared with measurements in Fig. 8.11. AcF 3 shows that the conventional one-moment approach leads to lower velocities, whereas the two-conditional moment approach markedly improves the predictions. This is due to the improved temperature prediction: the increased temperature along the centerline leads to thermal expansion and increased droplet velocities. Both AcF 1 and 3 show good prediction of the mean spray velocity at all locations. AcF 2 shows good predictions at the outer radii, but lower centerline velocity is predicted. This may be due to early jet break-up and would be consistent with the overprediction of the centerline temperature reported above. AcF 5 shows very good agreement except the slight underprediction on the centerline at $z/D=30$. The variances of the axial velocity profiles are compared in Fig. 8.12. The numerical predictions show acceptable agreement near the centerline, but predicted rms remains rather constant whereas all the experimental results indicate the rms to increase towards outer radii. It is emphasized here that the computations seem to present a more consistent picture if it is assumed that fluctuations are primarily induced by the velocity gradient. As example may serve here the measurements of the mean velocity profile of AcF 3 at $z/D=30$ as shown in Fig. 8.11. The velocity

gradient is relatively constant, leading –in theory– to relatively constant rms independent of the radial position, and the experimentally observed rms increase towards outer radii can therefore not easily be explained.

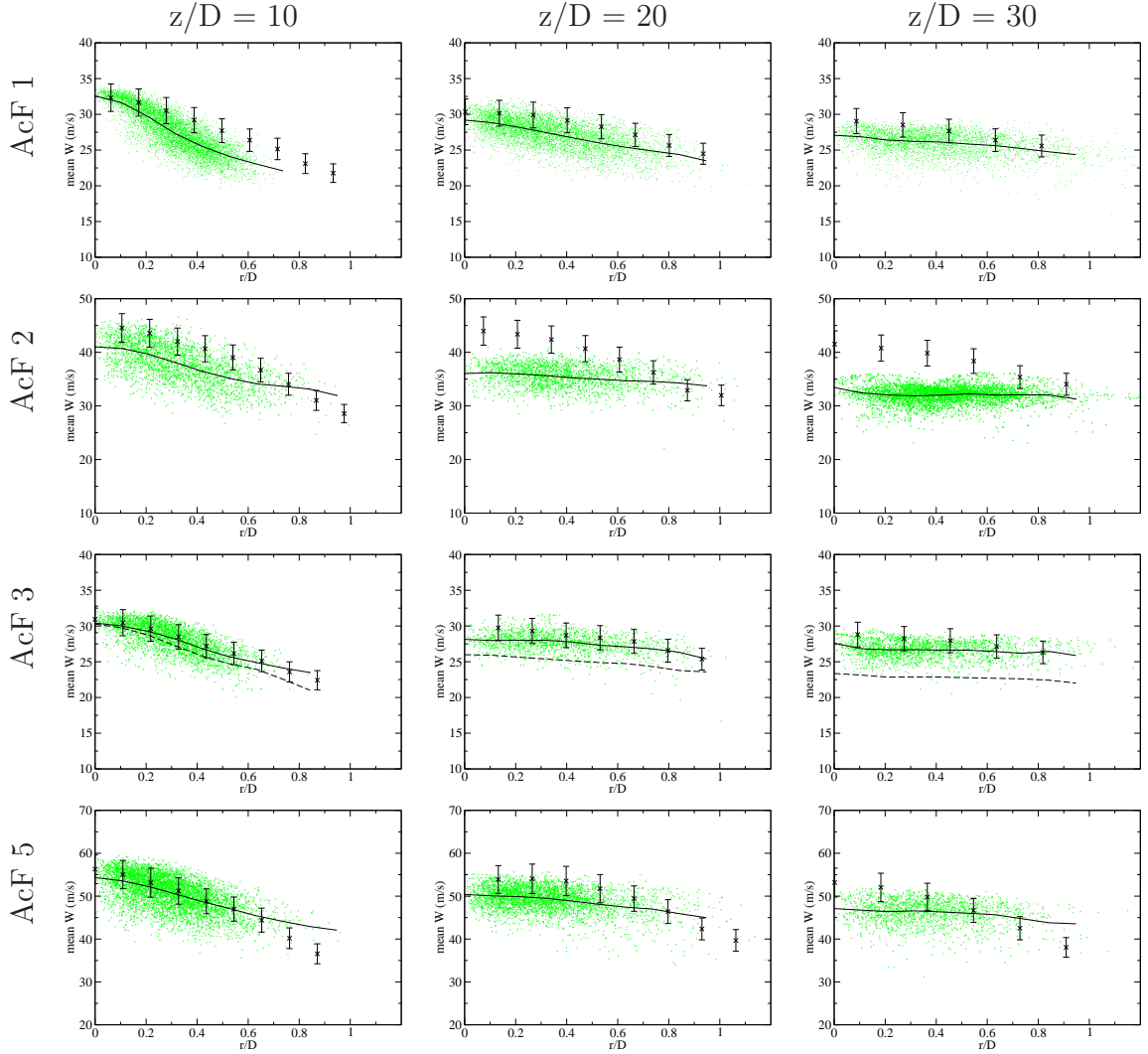


Figure 8.11: Mean axial droplet velocity profiles for the diameter range $20\text{--}30\ \mu\text{m}$. Crosses - experiments [113], scatter points - single realization of a simulated droplet, solid line - the two-conditional moment approach, dashed line - one-conditional moment approach.

8.3 Summary

The previous chapter showed limited capabilities of a conventional CMC approach to predict spray flames with pre-evaporation. In contrast, this study develops a

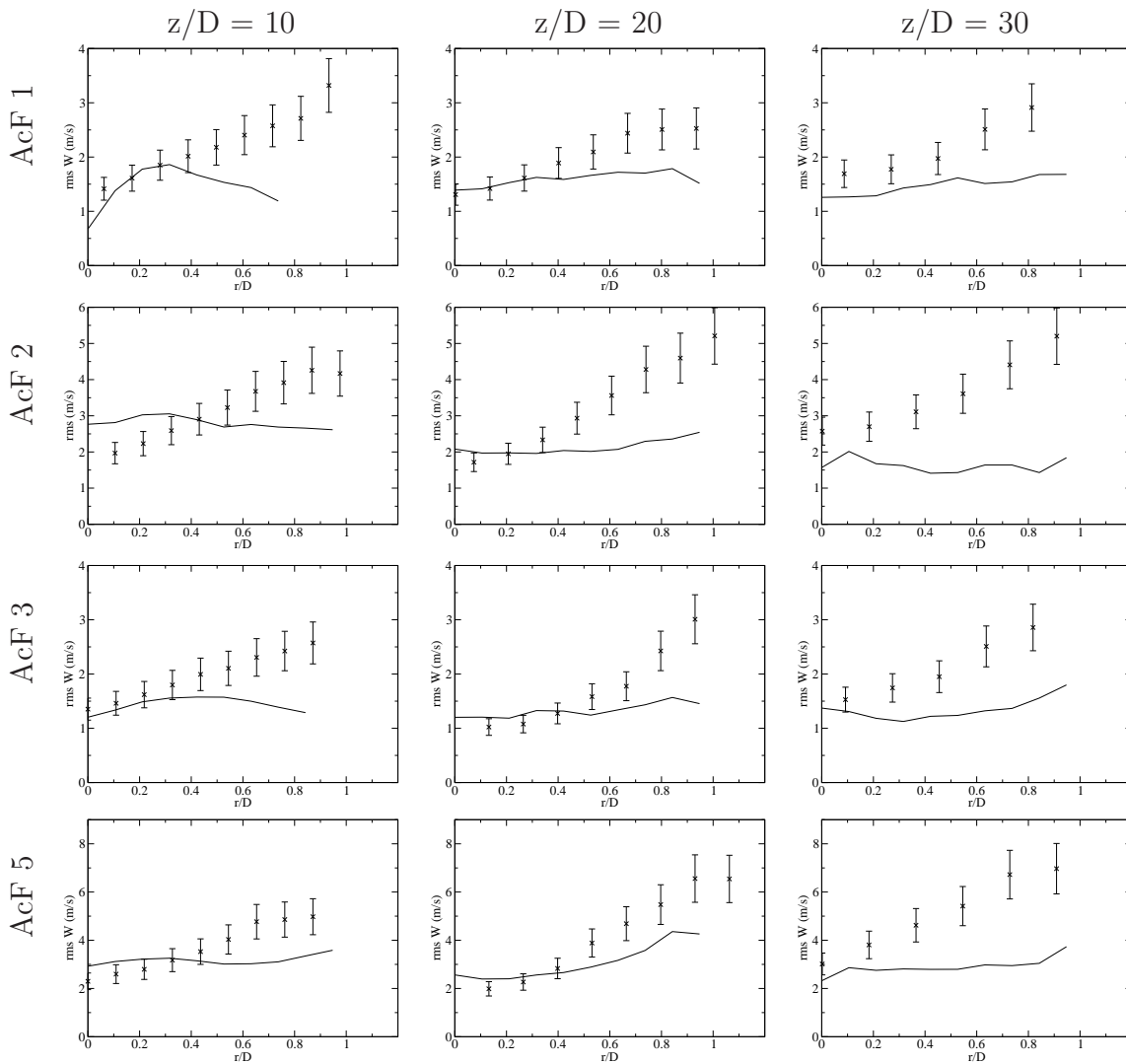


Figure 8.12: rms of axial droplet velocity profiles for the diameter range 20-30 μm . Crosses - experiments [113], solid line - the two-conditional moment approach.

two-conditional moment approach to extend the applicability of CMC. The two-conditional moment approach solves two conditional moments based on the total mixture fraction and the conserved mixture fraction to account for the shift of the upper limit of mixture fraction due to the evaporation process. A new method to select the upper boundary is also proposed, and the two-conditional moment is tested and validated using a non-reacting test case. Then, the methodology is validated by its application to a wide range of flames with different degrees of pre-evaporation (and Reynolds numbers). Four cases have been selected from the series of acetone flame experiments [113]. The conditional moment profiles clearly demonstrate the

effects of the two-conditional moment approach. The conditional moment based on ξ_{tot} becomes very important when non-reacting and reacting solutions co-exist within one CMC cell. Using the correct weighting between the two moments leads to significant improvements of the predicted radial temperature profiles, particularly near the centerline. It is also shown that the new model is robust enough to predict a flame series with varying degrees of pre-evaporation as long as the equivalence ratio of the fuel vapour exiting the jet does not allow for a flame burning largely in the premixed mode. Predictions of the spray mean velocity have also been improved. The mean velocity profiles show good agreement, but a slight underestimation is consistently found downstream. The predictions of the axial velocity rms are acceptable along the centerline, but the experimental trend of an increase of the rms at the outer radii is not captured.

Chapter 9

CMC with tabulated chemistry

A new methodology called two-conditional moment approach has been proposed to describe the dynamic shift of ξ_{UL} in time and space and quantify conditional fluctuations of properties by the amount of vapour originating from the liquid fuel after leaving the nozzle. The predictions of the flame have been greatly improved by the two-conditional moment approach. However, it might not be easily extendable to other flame configurations, since only the conditional fluctuations caused by droplet evaporation are modelled with the current methodology. Therefore, for example, the same methodology is not directly applicable to simulate a high Reynolds number flame with local extinction and reignition effects such as Sandia Flame F [101]. Therefore, a more robust methodology that can be applied to wider ranges of flame configurations would be beneficial, and a coupling of CMC and tabulated chemistry is proposed.

Tabulated chemistry is one of the most popular methods to simulate various turbulent flame configurations including spray flames. There are various methodologies to generate tabulated chemistry such as ILDM [110], REDIM [27, 115], FPI [66] and FGM [135, 38, 46]. A main advantage of the tabulated chemistry is its easy adaptivity to different flow and flame conditions, the flexibility to introduce additional (characteristic, conditioning) parameters, and the subsequent relatively low computational requirements for their use. A mixture fraction and a reaction progress variable are often chosen as parameters that allow for the characterization

of a relatively wide range of flame conditions [79]. However, the introduction of a second conditioning variable in the CMC context increases computational demands significantly and raises other closure issues [99]. The tabulated chemistry approach conventionally uses only one set of a chemical table (as opposed to CMC with its spatial and temporal variation of the composition space), and unsteady slow chemistry effects cannot be captured [168, 90]. Also, the method to construct the chemical table must be carefully chosen and is dependent on the target flame configurations. Of particular relevance are recent studies [60, 136] that indicate classical models that assume premixed or non-premixed configurations to be potentially inappropriate for spray flames.

Thus, this chapter discusses a new methodology that couples CMC and tabulated chemistry to enhance the modelling capabilities [177]. Some earlier studies [102, 101] have applied a chemical table to model the conditional chemical source terms in the CMC equation. The method has been applied to RANS predictions of flames with moderate to significant local extinction leading to large fluctuations around the conditional mean. The objective of this chapter is to establish a methodology that combines CMC and tabulated chemistry for spray combustion in LES. Sec. 9.1 discusses formulations and the new coupling approach of CMC and tabulated chemistry. Then, the results of the spray flame analysis is given in Sec. 9.2.

9.1 Coupling of CMC and Tabulated Chemistry

The spray flames with the amount of pre-evaporation investigated here cause some premixing and deviations of the typical non-premixed flame structure that could be solely parameterized by mixture fraction. A progress variable is introduced to capture different types of flame structures and conditional fluctuations. The reader is reminded here that in general the CMC cells are quite large in comparison with the LES cells (see e.g. [132]). The LES (in contrast to the singly conditioned CMC) resolves most of the fluctuations, and the LES-filtered progress variable can provide a local estimate of the reaction progress and hence of the deviations from

the conditional mean if –and only if– the chemical source term in Eqn. (9.1) can be modelled accurately. For the latter, this study introduces tabulated chemistry where the composition field is scaled for consistency with the CMC solution. This method is called *extended* CMC (CMCe), and a similar procedure had been introduced for gaseous flames with significant extinction in [101].

9.1.1 Formulations

The mass, momentum, mixture fraction (both ξ_{tot} and ξ_{cons}) and progress variable transport equations are solved (Eqns. 2.18, 2.19, 2.31 and 2.37). Note that the mixture fraction used in this chapter is equivalent to ξ_{tot} (see Sec. 8.1.1), and ξ_{cons} is still necessary to estimate ξ_{UL} . The progress variable is defined by $c = Y_{CO_2} + Y_{CO} + Y_{H_2O} + Y_{H_2}$ as in [78]. Since the progress does not include the liquid fuel composition, Eqn. 2.37 can be written as

$$\frac{\partial}{\partial t}(\bar{\rho}\tilde{c}) + \frac{\partial}{\partial x_i}(\bar{\rho}\tilde{u}_i\tilde{c}) = -\frac{\partial \overline{J_{c,j}}}{\partial x_i} - \frac{\partial J_{c,j}^{sgs}}{\partial x_i} + \bar{\rho}\tilde{\omega}_c, \quad (9.1)$$

where $\tilde{\omega}_c$ is a summation of reaction rates of all four species, $\tilde{\omega}_c = \tilde{\omega}_{CO_2} + \tilde{\omega}_{CO} + \tilde{\omega}_{H_2O} + \tilde{\omega}_{H_2}$. The CMC equation with spray source term (Eqn. 4.11) is solved using the boundary conditions in mixture fraction space as introduced in Sec. 8.1. The Lagrangian approach is used to solve the transport of the droplet, and the stochastic dispersion and evaporation models are applied.

9.1.2 Tabulation of the Composition Space

A two-dimensional table that lists the chemical compositions, the chemical source terms and the thermodynamic properties are generated as functions of the mixture fraction and the progress variable. A flamelet generated manifold method is utilized to compute the table as described in [38] with the only exception that the 0-dimensional unsteady CMC equations is used for its generation

$$\frac{\partial Q_\alpha}{\partial t} = N_\eta \frac{\partial^2 Q_\alpha}{\partial \eta^2} + \omega_{\eta,\alpha}, \quad (9.2)$$

where N_η is approximated by the AMC method (Eqn. 4.17). The conditionally averaged reactive species – and thus the conditionally averaged reaction progress – is varied by varying N_η . For N_η larger than the extinction value, unsteady solutions are used for the table which is equivalent to the procedure outlined in [38].

9.1.3 Scaling of the Tabulated Composition Space

The tabulated composition space, $Q^0(\eta, \zeta)$, is invariant in space and time while the CMC solution can account for finite rate chemistry effects, so that in general

$$Q_\alpha(\eta) \neq \int Q_\alpha^0(\eta, \zeta) P(\zeta | \eta) d\zeta. \quad (9.3)$$

Here, ζ is the sample space of the reaction progress variable. To ensure consistency between the table and the CMC solution, a rescaling procedure presented in [101] for gaseous combustion is implemented. The table needs to be rescaled by a scaling factor

$$g_\alpha(\eta) = \frac{Q_\alpha(\eta)}{\int Q_\alpha^0(\eta, \zeta) P(\zeta | \eta) d\zeta}, \quad (9.4)$$

and the scaled field for the computation of the chemical source term is obtained from

$$Q_\alpha^{0,sc}(\eta, \zeta) = g_\alpha(\eta) Q_\alpha^0(\eta, \zeta). \quad (9.5)$$

Subsequent normalizations are performed at each table cell to maintain a certain criteria. First, the summation of the mass fractions is unity as

$$\sum_{\alpha=1}^{N_{sp}} Q_\alpha^{0,sc}(\eta, \zeta) = 1.0. \quad (9.6)$$

Also, the progress variable of the tabulated chemistry cannot be modified by the scaling, so that the reference space in the progress variable given as

$$Q_{CO_2}^{0,sc}(\eta, \zeta) + Q_{CO}^{0,sc}(\eta, \zeta) + Q_{H_2O}^{0,sc}(\eta, \zeta) + Q_{H_2}^{0,sc}(\eta, \zeta) = \zeta. \quad (9.7)$$

The chemical source terms of the CMC equation (Eqn. (4.11)) and of the LES-

filtered reaction progress variable (Eqn. (9.1)) are computed by

$$\omega_{\eta,\alpha} = \int \omega_{\alpha}(Q_1^{0,sc}, \dots, Q_{N_s}^{0,sc}, Q_h^{0,sc}) P_{CMC}(\zeta | \eta) d\zeta, \quad (9.8)$$

and

$$\tilde{\omega}_c = \iint \omega_c(Q_1^{0,sc}, \dots, Q_{N_s}^{0,sc}, Q_h^{0,sc}) P_{LES}(\eta, \zeta) d\zeta d\eta, \quad (9.9)$$

where $P_{CMC}(\eta, \zeta)$ and $P_{LES}(\eta, \zeta)$ denote the Favre-filtered density functions of the CMC cells and the LES cells, respectively.

9.1.4 FDFs and the Integration of Conditional Moments

Similar to the filtered source terms, any LES-filtered reactive species can be computed from

$$\tilde{Y}_{\alpha} = \iint Q_{\alpha}^{0,sc}(\eta, \zeta) P_{LES}(\eta, \zeta) d\zeta d\eta. \quad (9.10)$$

Any joint FDF can be expressed by the marginal FDF and the conditional FDF,

$$P(\eta, \zeta)_{LES} = P(\eta)_{LES} \cdot P(\zeta|\eta)_{LES}, \quad (9.11)$$

and each part is modelled separately. On the CMC and LES grids, $P(\eta)$ is given by a bounded β -FDF to account for the dynamic changes of ξ_{UL} [62]. In absence of any more convincing model and for simplicity, most studies using two-dimensional flamelet generated manifolds assume statistical independence between mixture fraction and the reaction progress, i.e. $P(\zeta|\eta)_{LES} = P(\zeta)$ [38, 144]. Often, a δ -FDF is assumed, yielding

$$P_{LES}(\eta, \zeta) \approx P(\eta)_{LES} \cdot \delta(\tilde{c} - \zeta). \quad (9.12)$$

However, the validity of this assumption is more than questionable since the reaction progress will correlate with mixture fraction. This is certainly true close to the nozzle where the pilot should be associated with a normalized reaction progress variable close to unity while reaction progress should be close to zero elsewhere. Information

from the CMC equation for the modelling of $P(\zeta | \eta)$ is employed, viz.

$$P_{CMC}(\zeta | \xi) \approx \delta(Q_c(\eta) - \zeta), \quad (9.13)$$

$$P_{LES}(\zeta | \xi) \approx \delta(\langle c | \eta \rangle_{LES}^* - \zeta), \quad (9.14)$$

where $Q_c(\eta) = Q_{CO_2} + Q_{CO} + Q_{H_2O} + Q_{H_2}$ refers to the conditional moment of the progress variable, and $\langle c | \eta \rangle_{LES}^*$ is the conditionally averaged progress variable on an individual LES grid which needs to be modelled. Note that the LES-filtered progress variable, \tilde{c} , evolves by Eqn. (9.1) and largely independently of $Q_c(\eta)$ that evolves by Eqn. (4.11). It follows that

$$\tilde{c}_{cmc} = \int_0^1 Q_c(\eta) P_{LES}(\eta) d\eta, \quad (9.15)$$

and \tilde{c}_{cmc} is not necessarily equals \tilde{c} . Consistency requires modelling of $\langle c | \eta \rangle_{LES}^*$ by

$$\langle c | \eta \rangle_{LES}^* = \frac{\tilde{c}}{\tilde{c}_{cmc}} Q_c(\eta). \quad (9.16)$$

Any LES property that is dependent on the mixture composition can then be obtained from

$$\tilde{\phi} = \int \int \phi^{0,sc}(\eta, \zeta) P(\eta) \cdot \delta(\langle c | \eta \rangle_{LES}^* - \zeta) d\zeta d\eta. \quad (9.17)$$

A further comment refers to the relationship between P_{CMC} and P_{LES} and differences to corresponding RANS-based studies. Kronenburg and Kostka [101] solved a separate transport equation for the conditionally averaged variance of c and modelled $P_{CMC}(\zeta | \eta)$ assuming a β -shape of the distribution. In LES-CMC, this may not be necessary, because the conditional variance could be approximated by conditional sampling of the LES values, \tilde{c} , within one larger CMC cell. This procedure would be similar to the modelling of the conditional dissipation and the conditional velocity where LES sgs-correlations are neglected. However, currently the equality of \tilde{c} and \tilde{c}_{cmc} is not enforced (see above), since differences in the mean value prevent the

use of the modelling of $P_{CMC}(\zeta | \eta)$ by LES quantities, and some inconsistencies between P_{CMC} and P_{LES} need to be accepted. Eqns. (9.13) and (9.14) are used instead and future studies will investigate possibilities to enforce closeness of \tilde{c} and \tilde{c}_{cmc} .

Difference between Eqns. 9.12 and 9.14 are illustrated in Fig. 9.1. If Eqn. 9.12 was applied, the LES quantities are integrated using tabulated values for a constant reaction progress variable values as indicated by the orange line. If the integration is simply using Q_c , the corresponding LES-filtered values \tilde{c}_{cmc} , is underestimated (cross) compared to the LES solution, \tilde{c} . Therefore, the rescaled profiles, $\langle c | \eta \rangle_{LES}^*$, is needed to make the integrated solution and LES solution consistent, and Eqn. 9.14 uses the values from the purple dashed profile $P(\zeta | \eta = \xi) = \delta(\langle c | \eta \rangle_{LES}^* - \zeta)$, that is closely correlated with the CMC solution. If the quantities are highly non-linear (e.g. reaction rates), the integration method can lead to large differences, and comparisons are shown in the next section.

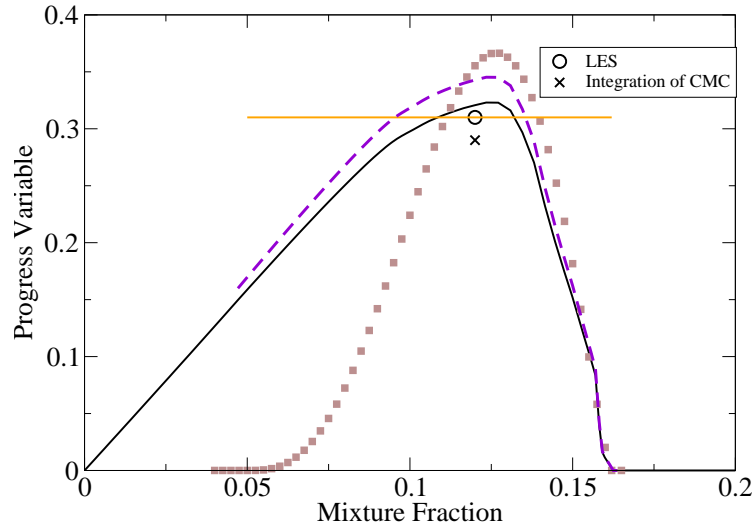


Figure 9.1: Diagram of the joint FDF structures. Black solid line - Q_c , purple dashed line - $\langle c | \eta \rangle_{LES}^*$, brown square dotted line - $P(\eta)$ constructed by assuming a β -FDF with $\tilde{\xi} = 0.12$, $\tilde{\xi}''^2 = 0.004$ and $\xi_{UL} = 0.162$, circle - $(\tilde{\xi}, \tilde{c})$, cross - $(\tilde{\xi}, \tilde{c}_{cmc})$.

9.1.5 Implementation of CMC with Tabulated Chemistry

The flowchart with CMC with tabulated chemistry is shown in Fig. 9.2. It additionally includes the scaling of tabulated chemistry, and modelling of the subgrid joint-FDF by scaling with \tilde{c} and \tilde{c}_{cmc} . Also, the transport equation of the progress variable is solved, and the LES-filtered reaction rate must be obtained properly by integration over the rescaled tabulated chemistry.

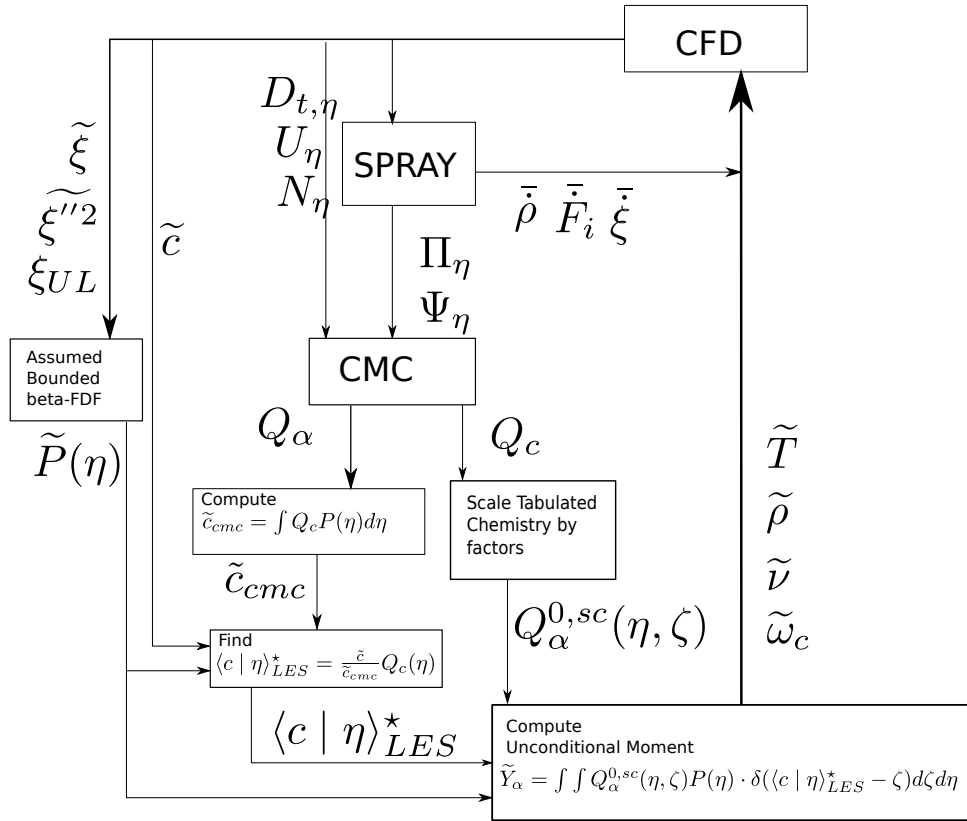


Figure 9.2: Flowchart of CMC coupled with LES using tabulated chemistry (CMCe).

9.2 Results and Discussion

The validity of CMCE is first discussed by analyzing the solutions of the progress variable. Then, the statistics obtained by CMCE and the conventional CMC approach are compared to experimental results, and the improvements by the CMCE are highlighted. AcF 1 and 3 are chosen as test cases, and their parameters are

given in Table 5.1 and details of the numerical configurations are given in Sec. 5.3.

9.2.1 Conditional Moment

In the current approach, the progress variable is computed by two different equations: the Favre-filtered transport equation (Eqn. (9.1)) and the CMC equations (Eqn. (4.11)). Both equations are closely correlated [96], however, the solutions may differ due to different degrees of modelling involved which is necessitated by the large differences in cell size. However, the two solutions should stay “close” to ensure reasonable scaling by Eqn. (9.5). Fig. 9.3 shows a comparison of the progress variables for both test flames at different downstream positions. The LES solutions do not fluctuate around a conditional mean and agree with Q_c for both cases on the lean side and at every position in the domain. This is because the evaporation process hardly affects the lean side and cannot generate any deviations from a conditional mean there. Large conditional fluctuations of the LES solutions are, however, observed on the rich side. These are triggered by the spray evaporation processes since evaporation randomly changes the cell mixture fraction but leaves the reactive species composition largely unchanged. At $z/D=10$, the LES solution averaged within one CMC cell, $\langle c | \eta \rangle \approx \langle \tilde{c} | \tilde{\xi} = \eta \rangle$, shows a sharp discontinuity around ξ_{jet} for AcF 1 and AcF 3. There, a high probability of finding unmixed fluid originating from the jet exists. In contrast, the CMC solution shows a much smoother profile due to the existence of the dissipation term in Eqn. (4.11). Such a sharp gradient cannot be captured by CMC. At this position, AcF 3 is influenced more strongly by the evaporation effects due to the lower amount of pre-evaporation, i.e. lower ξ_{jet} . Further downstream, the CMC solutions agree well with the averaged LES solution, despite relatively large fluctuations around the conditional mean as indicated by the strong variation of the LES-filtered solutions. Closeness of $\langle c | \eta \rangle$ and $Q_c(\eta)$ results in reasonable scaling of the tabulated chemistry values and it seems that no further external forcing is needed to drive $Q_c(\eta)$ towards $\langle c | \eta \rangle$. Differences between these two expressions for the conditionally averaged reaction progress are larger for larger mixture fraction values. This is due to some

uncertainty in the modelling of suitable boundary conditions for the reactive scalars at the upper mixture fraction bound (remember, the correct boundary values would be known at the droplet surface, but droplets are unresolved here as is common in Euler-Lagrange computations for spray flames). The FDF plotted in the same figure shows, however, that the probability for these high mixture fraction values is low, and that discrepancies will not unduly affect the solution.

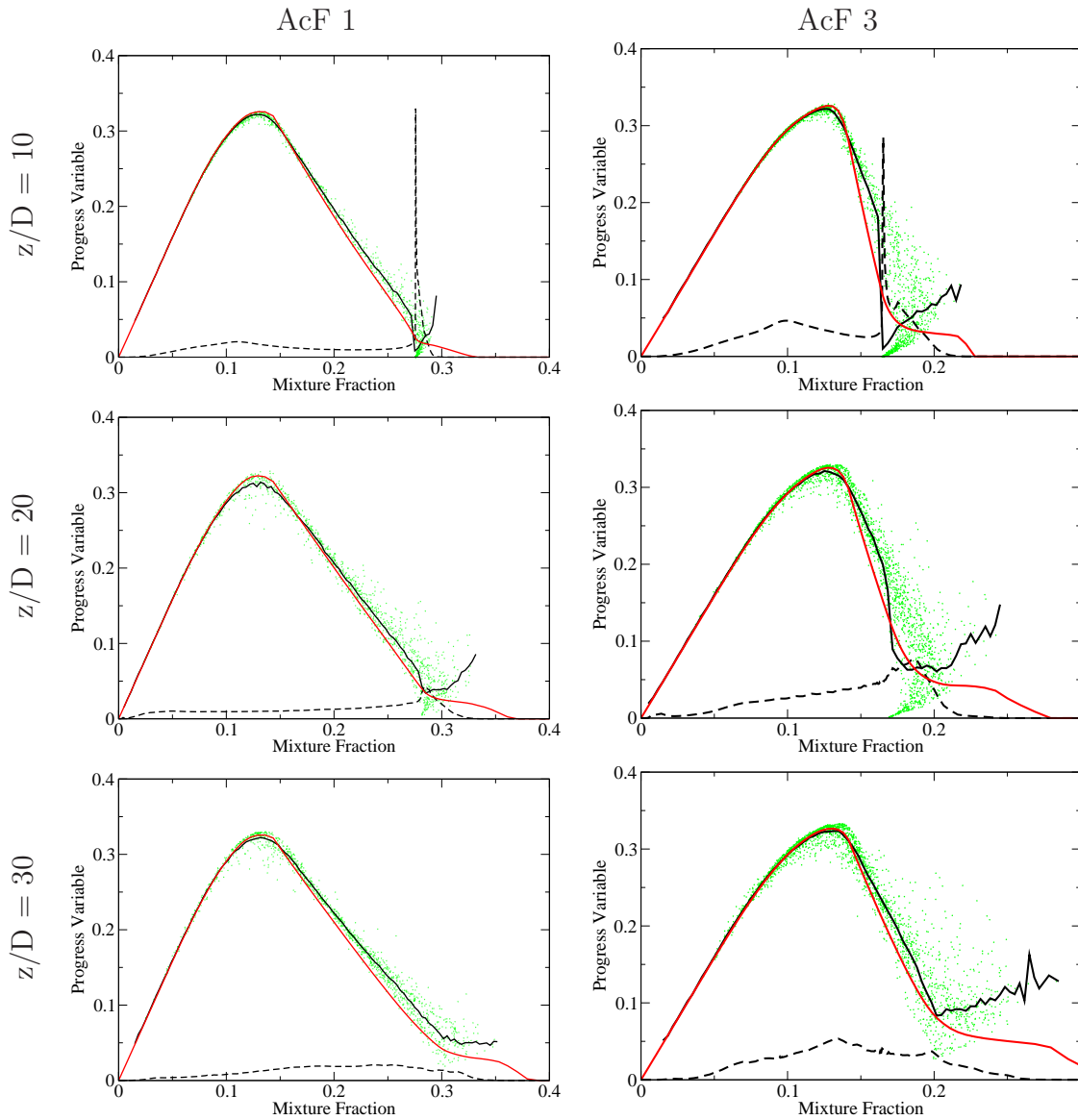


Figure 9.3: Progress variable comparisons. Green dots - LES-filtered values; Black solid line - conditionally averaged LES-filtered values $\langle c | \eta \rangle$; Red solid line - CMC solution Q_c ; dashed line - $P_{CMC}(\eta)$ within the corresponding CMC cell.

The effect of the modelling of the joint FDF (Eqns. (9.12) and (9.14)) is examined

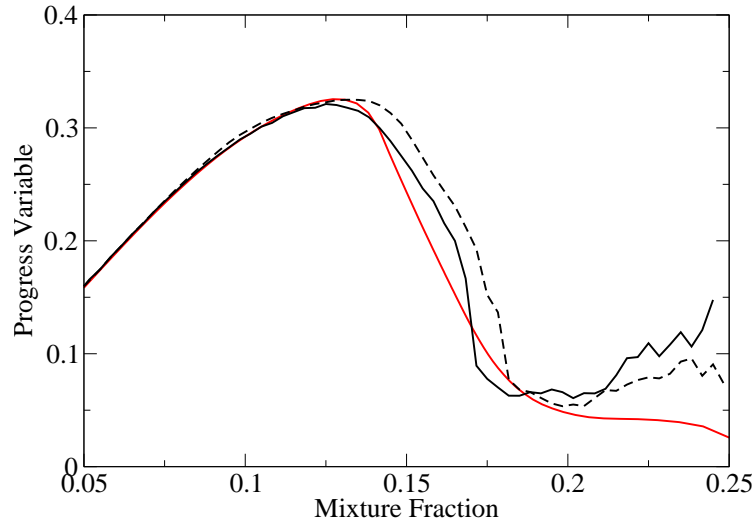


Figure 9.4: Effects of joint FDF modelling on progress variable at $z/D=20$ in flame AcF 3. Solid line - $\langle c | \eta \rangle$ using the correlated joint FDF (Eqn. (9.14)); dashed line - $\langle c | \eta \rangle$ using the statistically independent joint FDF Eqn. (9.12); red line - Q_c .

in Fig. 9.4. Using the statistically independent joint FDF (Eqn. (9.12)), the peak of $\langle c | \eta \rangle$ is shifted towards the rich-side, and a relatively large offset from Q_c is observed. In contrast, the correlated FDF (Eqn. (9.14)) provides better agreement with Q_c , and a more realistic approximation of the physical value is to be expected here. The modelling of $P_{LES}(\eta, \zeta)$ does not affect Q_c directly, since indirect effects through modified density and velocity fields are very small, so that only one solution for Q_c is shown here.

Fig. 9.5 compares the CMC solution and the unscaled tabulated values ($\int Q_\alpha^0(\eta, \zeta) P_{LES}(\zeta | \eta) d\zeta$) of two of the chemical species that constitute the reaction progress variable. The solutions for the species H_2O agree very well everywhere in the domain. However, a noticeable difference appears for CO , correctly indicating finite rate effects of the CMC solution due to the relatively slow conversion from CO to CO_2 .

9.2.2 Unconditional Moment

Chapter 7 predicted the measured temperature profiles quite well with the notable exception of significant underprediction of the temperature along the centerline. The

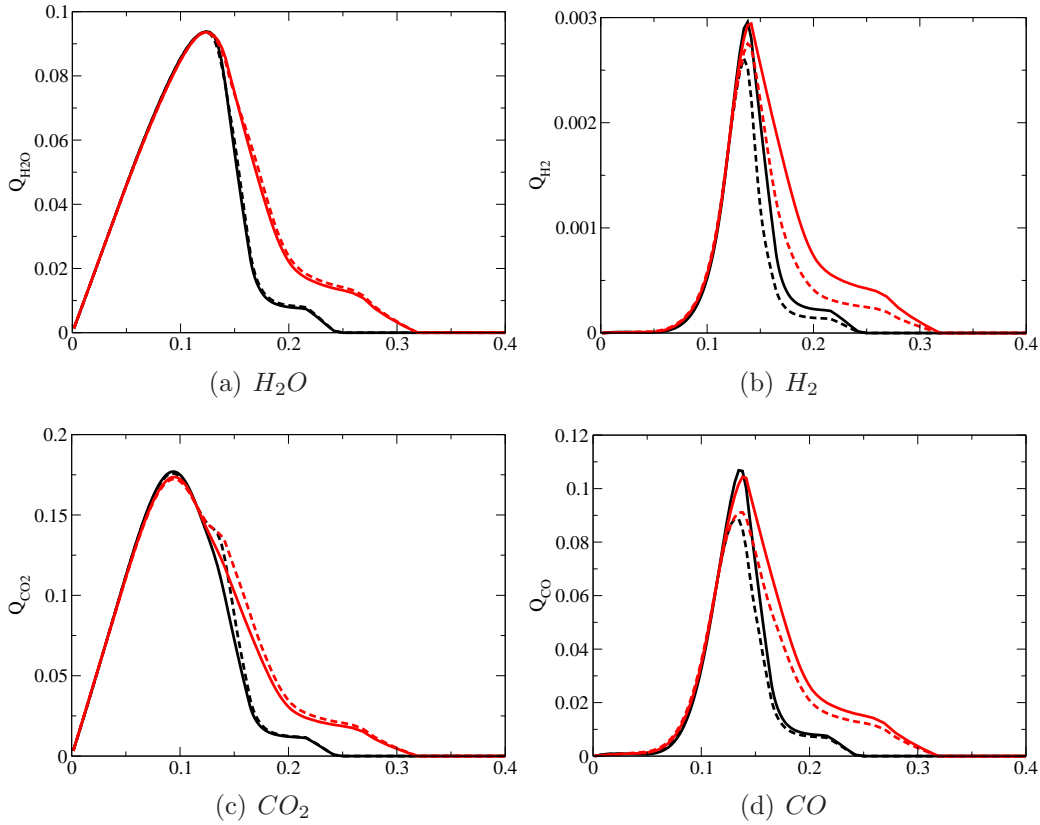


Figure 9.5: Conditional averages of four species constituting the progress variable: comparison of the CMC solution ($Q_\alpha(\eta)$ – solid line), with the respective values from unscaled chemistry table ($\int Q_\alpha^0(\eta, \zeta) P_{LES}(\zeta | \eta) d\zeta$ – dashed line). Black lines - $z/D=10$, red lines - $z/D=30$.

underprediction originated from the CMC solution that did not allow for a variation of the reaction progress on the LES grid for a similar mixture fraction distribution. However, large variations exist (see Fig. 9.3), and CMCE can now account for these fluctuations on the LES grid. A direct comparison of conventional CMC and CMCE is shown for flame AcF 3 in Fig. 9.6. The new implementation is clearly capable of approximating the variation of the filtered temperature along the centerline much better than previous implementations. Also, the temperature profiles of AcF 1 show reasonably good agreement with the experiments and compare very favorably with all other predictions of this flame published in the literature [38, 37]. The instantaneous mixture fraction and temperature fields of AcF3 are shown in Fig. 9.7. The temperature along the centerline increases towards the downstream part of

the domain, and it is not correctly captured when using the conventional CMC (Fig. 7.8). Also, the progress variable profile is very similar to the temperature profile as expected. It is shown from the conditional plots in Fig. 9.3 that most of the LES cells have non-zero progress variables. More fuel evaporates due to the temperature increase, and a much higher increase in mixture fraction values can be seen when compared to the conventional CMC where $\tilde{\xi}$ did not significantly surpass ξ_{jet} in the entire domain.

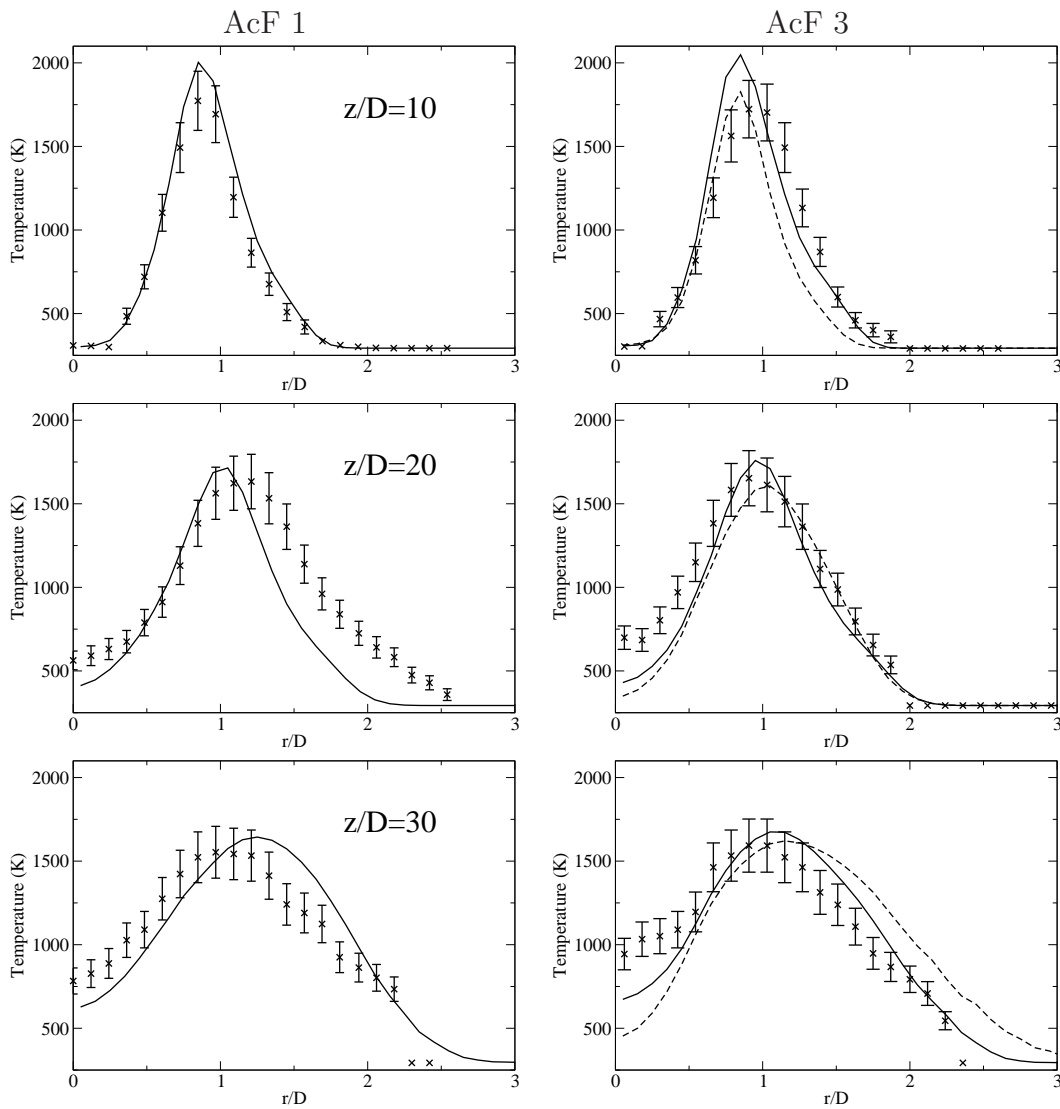


Figure 9.6: Mean temperature profiles. Solid lines - CMCe, dashed lines - conventional CMC without spray source term in CMC equations, X - experiment with error bars.

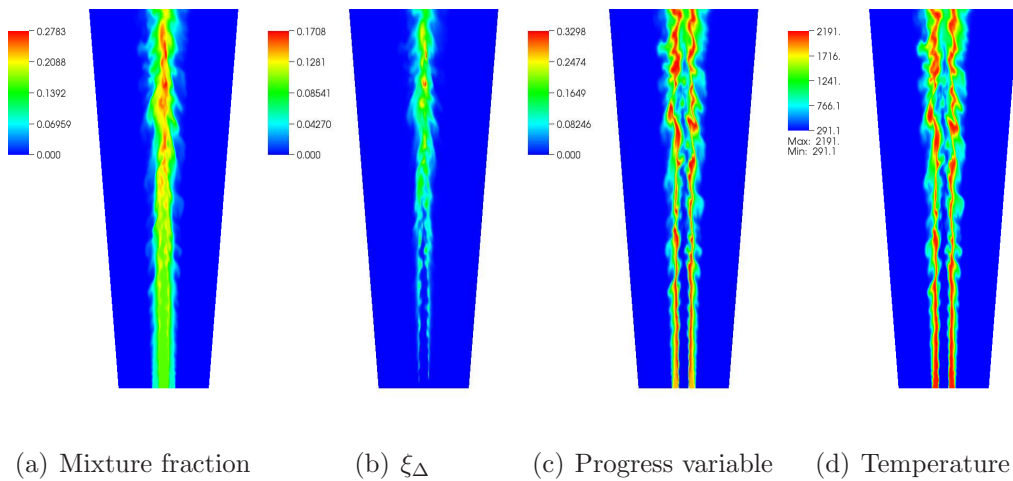


Figure 9.7: Instantaneous contour plot of AcF3 with CMCE.

9.2.3 Spray Statistics

The mean axial spray velocity profiles are compared in Fig. 9.8. Conventional CMC in AcF 3 predicts lower velocities due to the significant underprediction of temperature (and consequently, the underprediction of thermal expansion) close to the centerline, especially at downstream positions beyond $z/D = 10$. Results improve markedly when CMCE is applied and the accurate modelling by CMCE is corroborated by the good agreement of velocity data for flame AcF 1. The rms of the spray also shows acceptable agreement at $z/D = 10$, and $z/D = 20$ in Fig. 9.9 along the centerline. However, it is still found that rms at outer radii is underpredicted as discussed in Secs. 7.2.3 and 8.2.3

9.2.4 Model Comparisons

In Chapter 7, the conventional CMC with spray source terms has been investigated, Chapter 8 has introduced a two-conditional moment approaches, and this chapter proposes another model, CMC with tabulated chemistry. Figure 9.10 shows all three modelling approaches on temperature and droplet velocity predictions. The temperature profile clearly indicates that new approaches improve the prediction along the centerline. No significant difference at outer radii is found since the most of the evaporation processes occurs at the jet-pilot interface as seen in Figs. 8.10

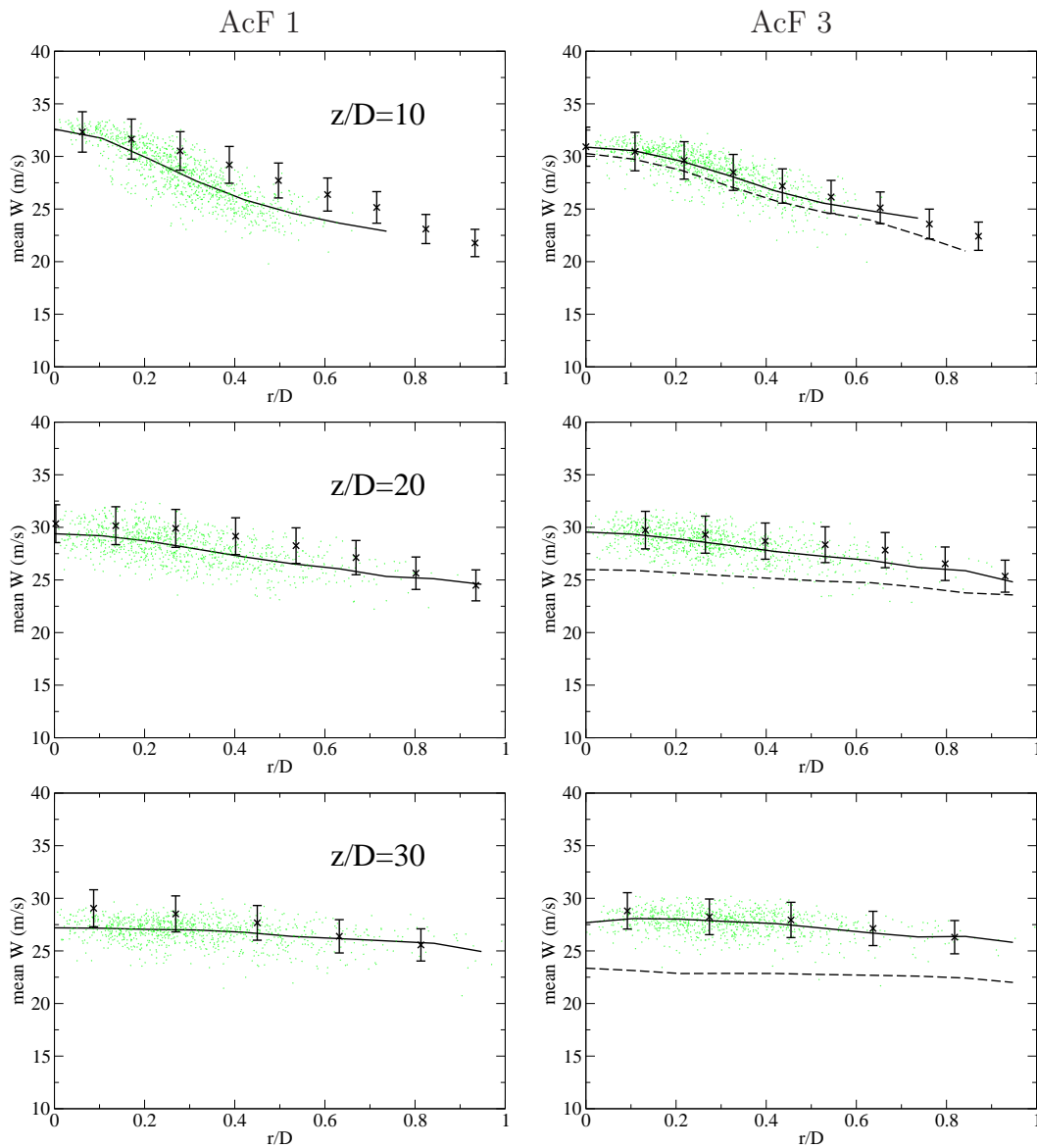


Figure 9.8: Radial profiles of the mean axial droplet velocities for the droplet diameter range $20\text{-}30\ \mu\text{m}$. Solid line - CMCe, scattered green points - single realization of a simulated droplet, dashed line - conventional CMC without spray source term in CMC equations, X - experiment with error bars.

and 9.7. Remarkable improvements of the mean velocity profiles are achieved by both new methodologies due to the better predictions of the temperature profiles that lead to larger thermal expansion.

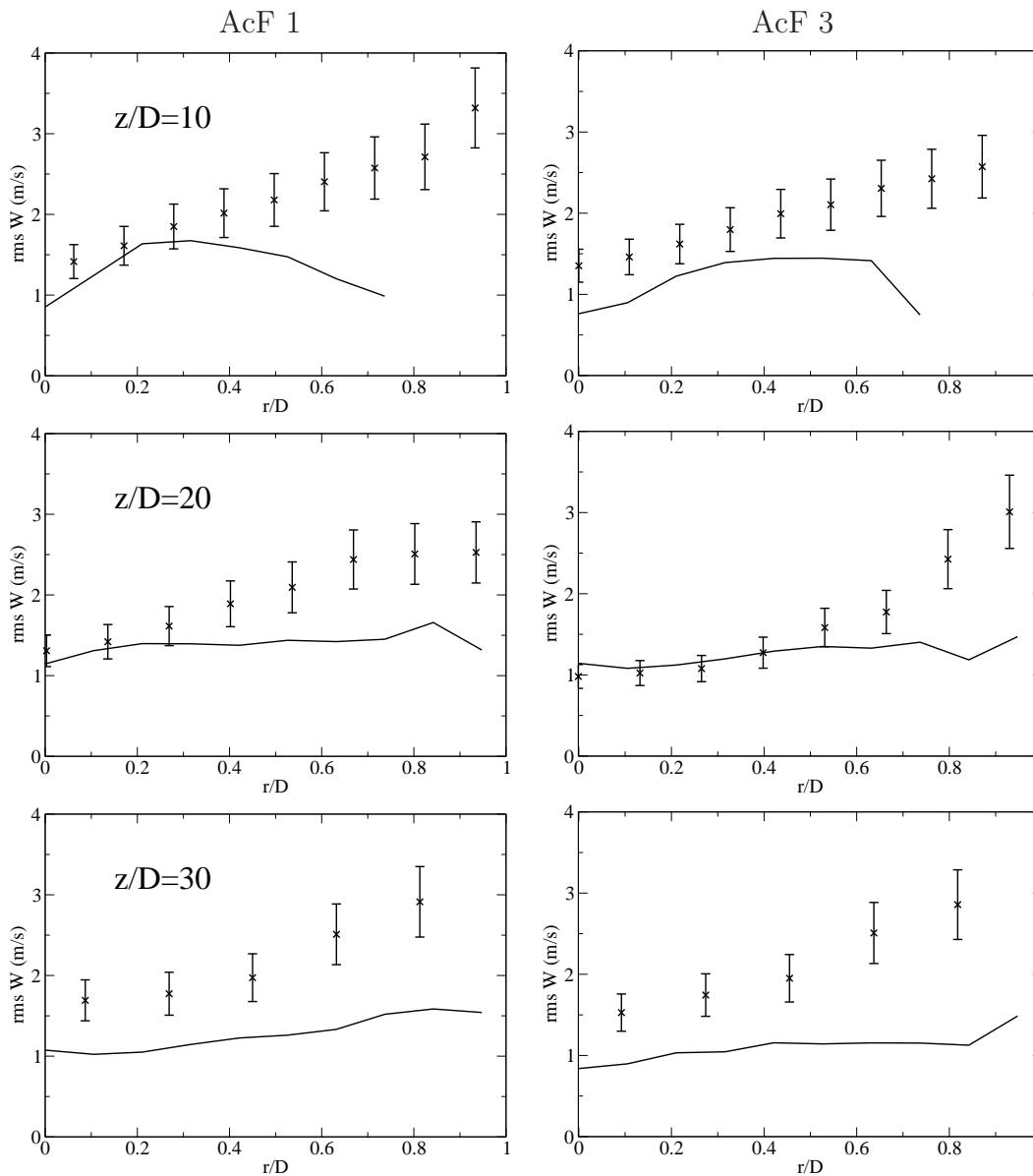


Figure 9.9: Radial profiles of rms of the axial droplet velocity for the diameter range 20-30 μm of AcF 3. Solid line - CMCE, X - experiment with error bars.

9.3 Summary

A new methodology to couple CMC with tabulated chemistry has been introduced. The CMC solution is used to scale the tabulated composition space, and LES properties are computed by integration over the scaled composition space using a joint FDF that uses a correlation between the progress variable and mixture fraction derived from the CMC solution. CMCE is validated by comparison with experiments

from two acetone spray flames. The conditional profiles indicate that the CMC and LES solutions are well correlated, and their solutions do not diverge. CMCe results in improved temperature predictions and mean spray profiles when compared to the conventional CMC modelling, and overall good agreement is observed for both flame configurations.

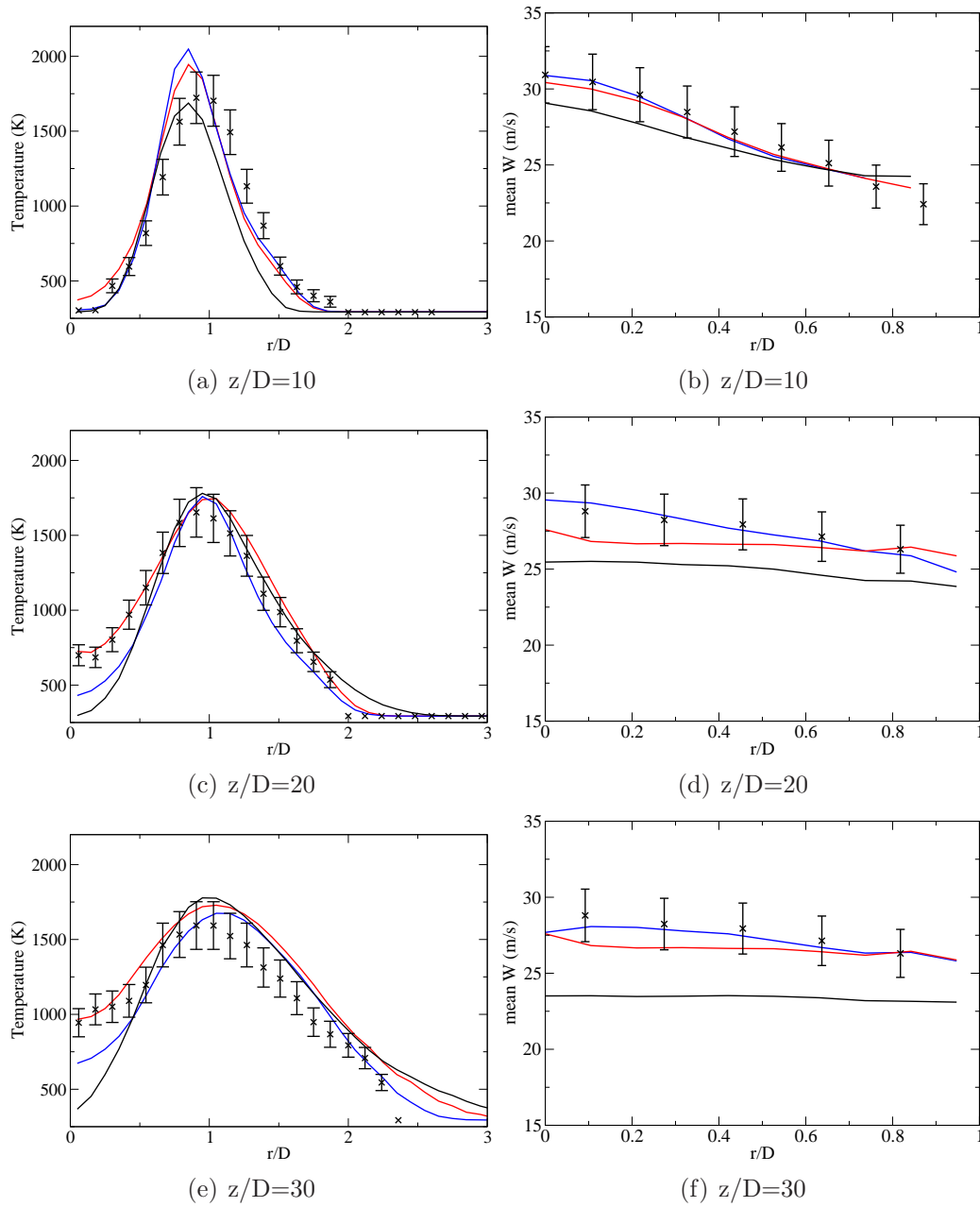


Figure 9.10: Left - radial profiles of mean temperature, right - radial profiles of the mean axial droplet velocities for the droplet diameter range $20\text{-}30\ \mu\text{m}$. Crosses - experiments, black solid line - conventional CMC with spray source terms (Chapter 7), red line - the two conditional moment approach (Chapter 8), blue line - CMC with tabulated chemistry (This Chapter).

Chapter 10

Conclusions and Future Work

10.1 Conclusions

The scope of the thesis is to establish a methodology to improve the modelling of turbulent spray flames. Due to its multi-scale nature, small scale physics must be modelled appropriately. Large eddy simulation (LES), a Lagrangian approach with stochastic particle dispersion and evaporation and conditional moment closure (CMC) have been coupled, and new closures and modelling approaches within the CMC context have been derived and discussed.

First, simulations of an evaporating spray jet have been performed by LES and the Lagrangian tracking scheme with and without the stochastic subgrid model. The numerical predictions have agreed with the mean axial velocity profile in axial and radial directions. Also, the rms profiles of axial velocity have been well predicted. However, the mean and rms profiles of the radial velocities have been underpredicted by about 20 %. Effects of subgrid scales on velocity statistics have found not to be very important, probably due to the moderate turbulence levels of the spray jet investigated here. Subgrid scale effects, however, have been important for the accurate prediction of the droplet evaporation rates and might have strong effects on the combustion regimes and turbulent spray flames.

The analysis has been then extended to an evaporating spray flame. The LES-CMC methodology has been first applied, and unclosed terms of the spray source

terms in the CMC equations have been analyzed and discussed. Also, several implementations of the boundary condition in mixture fraction space have been discussed. The macroscopic view has been identified as the possibly more feasible implementation, so that the boundary conditions have been defined by LES-filtered quantities (macroscopic) rather than the surface droplet quantities (microscopic view). The modified implementation of the CMC spray terms has been first validated by comparison of an LES-filtered solution for acetone with the CMC solution for a non-reacting jet. Then, the computations of the acetone spray flames have been performed, and it has showed that the CMC spray source terms shift the reacting solution to higher mixture fraction values, and inclusion of the CMC spray sources should not be neglected. The consistent CMC model has given very good agreement of predicted and measured temperatures, with the only exception of some locations near the centerline. The predictions of the mean and rms axial velocity distribution have been good, while some discrepancies could have been explained by small temperature deviations.

The underprediction of temperature have been observed in conventional LES-CMC is due to limitations of the chosen boundary condition at the upper mixture fraction limit. The upper mixture fraction boundary is set to the jet condition in conventional non-premixed flame configurations, and dependent quantities are fixed and equal to the fuel conditions. However, in the evaporating spray flames, it is possible to have large evaporation which leads to local mixture fractions larger than the jet values. Therefore, new methodologies that allow for freely moving upper boundaries have been developed. This study has proposed two different methods: a two-conditional moment approach and CMC with tabulated chemistry.

First, the two-conditional moment approach has been proposed to take account for the shift of the upper mixture fraction boundary caused by the evaporation process. It solves two conditional moments based on the total mixture fraction and the conserved mixture fraction, and a new method to select the upper boundary has been proposed. The LES quantities are computed by integrating the conditional moments estimated by interpolating two conditional moments by the weighting factor.

The two-conditional moment approach has been applied to a wide range of flames with different degrees of pre-evaporation (and Reynolds numbers). The effects of the two-conditional moment approach has been demonstrated when analyzing the scattering of ξ_Δ within a CMC cell. Using the correct weighting between the two moments has led to significant improvements of the predicted radial temperature profiles, particularly near the centerline. It has been also shown that the new model is robust enough to predict a flame series with varying degrees of pre-evaporation as long as the equivalence ratio of the fuel vapour exiting the jet does not allow for a flame burning largely in the premixed mode. Predictions of the spray mean velocity have also been improved. The mean velocity profiles have shown good agreement, but a slight underestimation have been consistently found downstream. The predictions of the axial velocity rms have been found to be acceptable along the centerline, but the experimental trend of an increase of the rms at outer radii have not been captured.

Another methodology called CMCe which is equivalent with CMC using tabulated chemistry has been developed. The CMC solution is used to scale the tabulated composition space, and LES properties are computed by integration over the scaled composition space using a joint FDF that uses a correlation between the progress variable and mixture fraction derived from the CMC solution. CMCe has been validated by comparison with experiments from two acetone spray flames. The conditional profiles have indicated that the CMC and LES solutions have been well correlated, and their solutions have not diverged. CMCe have resulted in improved temperature predictions and mean spray profiles when compared to the conventional CMC modelling, and overall good agreement have been observed for both flame configurations.

As a summary, this thesis has constructed new methodologies to simulate turbulent spray flames. The accurate implementation of LES-CMC of two-phase flows has been analyzed in detail, and two novel CMC approaches have been proposed and validated. Since this study has mainly focused on fuel rich spray flames, the two-conditional moment approach has been sufficient. However, since CMCe is

more generic approach, it is possible to be extended to simulate other complex flow configurations.

10.2 Recommendations for Future Work

There are some suggestions towards future developments. Even though the new approaches have improved on the rather strict limitation of the upper boundary conditions, non-premixed configurations were still assumed. Therefore, they are most likely not applicable to some of the spray flame configurations investigated in [113, 69] that have small mixture fraction values in the jet at the nozzle exit due to low amounts of pre-evaporation and that form premixed (or partially premixed) flame structures. It would be beneficial to develop a novel CMC approach that can simulate non-premixed and premixed type flames at the same time. Perhaps, recent premixed CMC studies [169, 4, 3] might provide a hint to add a premixed flame feature to the approaches developed in this thesis. Especially with the combination with CMCe, it might be able to establish a new CMC methodology that can simulate all regimes ranging from non-premixed and partially premixed flame with evaporating sprays.

In addition, CMC coupled with a microscopic view would aid the development of more accurate boundary conditions in mixture fraction space. The current CMC configurations are based on a macroscopic view which used LES-filtered quantities. However, within a spray flame, there are many micro structures near the droplets [96, 194] that are not fully considered in this study. Therefore, it might be beneficial to establish a new subgrid model based a on microscopic approach that can account for details of mixing between the droplet surface and the LES-filtered mean.

Bibliography

- [1] A. H. Abdelsamie and C. Lee. Decaying versus stationary turbulence in particle-laden isotropic turbulence: Turbulence modulation mechanism. *Physics of Fluids*, 24(1):015106, 2012.
- [2] B. Abramzon and W. A. Sirignano. Droplet vaporization model for spray combustion calculations. *International Journal of Heat and Mass Transfer*, 32:1605 – 1618, 1989.
- [3] S. Amzin and N. Swaminathan. Computations of turbulent lean premixed combustion using conditional moment closure. *Combustion Theory and Modelling*, 17(6):1125–1153, 2013.
- [4] S. Amzin, N. Swaminathan, J. W. Rogerson, and J. H. Kent. Conditional moment closure for turbulent premixed flames. *Combustion Science and Technology*, 184(10-11):1743–1767, 2012.
- [5] S. V. Apte, K. Mahesh, and P. Moin. Large-eddy simulation of evaporating spray in a coaxial combustor. *Proceedings of the Combustion Institute*, 32(2):2247 – 2256, 2009.
- [6] S. Balachandar. A scaling analysis for point-particle approaches to turbulent multiphase flow. *International Journal of Multiphase Flow*, 35:801–810, 2009.
- [7] S. Balachandar and J. K. Eaton. Turbulent dispersed multiphase flow. *Annual Review of Fluid Mechanics*, 42(1):111–133, 2010.

-
- [8] K. Balakrishnan, S. Ukai, and S. Menon. Clustering and combustion of dilute aluminum particle clouds in a post-detonation flow field. *Proceedings of the Combustion Institute*, 33(2):2255 – 2263, 2011.
- [9] R. S. Barlow, A. N. Karpetis, J. H. Frank, and J.-Y. Chen. Scalar profiles and NO formation in laminar opposed-flow partially premixed methane/air flames. *Combustion and Flame*, 127(3):2102 – 2118, 2001.
- [10] R. W. Bilger. Conditional moment closure for turbulent reacting flow. *Physics of Fluids A*, 5(2):436–444, 1993.
- [11] R. W. Bilger. Some aspects of scalar dissipation. *Flow, Turbulence and Combustion*, 72:93–114, 2004.
- [12] R. W. Bilger. A mixture fraction framework for the theory and modeling of droplets and sprays. *Combustion and Flame*, 158(2):191 – 202, 2011.
- [13] R. W. Bilger, S. B. Pope, K. N. C. Bray, and J. F. Driscoll. Paradigms in turbulent combustion research. *Proceedings of the Combustion Institute*, 30(1):21 – 42, 2005.
- [14] M. Bini. *Large Eddy Simulation of particle and droplet laden flows with stochastic modelling of subfilter scales*. PhD thesis, Imperial College, London, UK, 2006.
- [15] M. Bini and W. P. Jones. Particle acceleration in turbulent flows: A class of nonlinear stochastic models for intermittency. *Physics of Fluids*, 19:035104, 2007.
- [16] M. Bini and W. P. Jones. Large-eddy simulation of particle-laden turbulent flows. *Journal of Fluid Mechanics*, 614:207–252, 2008.
- [17] M. Bini and W. P. Jones. Large eddy simulation of an evaporating acetone spray. *International Journal of Heat Fluid Flow*, 30:471–480, 2009.

- [18] T. L. Bocksell and E. Loth. Stochastic modeling of particle diffusion in a turbulent boundary layer. *International Journal of Multiphase Flow*, 32(10-11):1234 – 1253, 2006.
- [19] G. Borghesi, E. Mastorakos, and R. S. Cant. Complex chemistry DNS of n-heptane spray autoignition at high pressure and intermediate temperature conditions. *Combustion and Flame*, 160(7):1254 – 1275, 2013.
- [20] G. Borghesi, E. Mastorakos, C. B. Devaud, and R. W. Bilger. Modeling evaporation effects in conditional moment closure for spray autoignition. *Combustion Theory and Modelling*, 15(5):725–752, 2011.
- [21] F. Bottone, A. Kronenburg, D. Gosman, and A. Marquis. The numerical simulation of diesel spray combustion with LES-CMC. *Flow, Turbulence and Combustion*, 89(4):651–673, 2012.
- [22] N. Branley. *Large Eddy Simulation of a Turbulent Non-premixed Flame*. PhD thesis, Imperial College, London, UK, 1999.
- [23] N. Branley and W. P. Jones. Large eddy simulation of a turbulent non-premixed flame. *Combustion and Flame*, 127:1914–1934, 2001.
- [24] A. J. M. Buckrell and C. B. Devaud. Investigation of mixing models and conditional moment closure applied to autoignition of hydrogen jets. *Flow, Turbulence and Combustion*, 90(3):621–644, 2013.
- [25] W. K. Bushe. Conditional source-term estimation, <http://kbspc.mech.ubc.ca/cse.html>.
- [26] W. K. Bushe and H. Steiner. Laminar flamelet decomposition for conditional source-term estimation. *Physics of Fluids*, 15(6):1564–1575, 2003.
- [27] V. Bykov and U. Maas. The extension of the ILDM concept to reaction-diffusion manifolds. *Combustion Theory and Modelling*, 11(6):839–862, 2007.

-
- [28] R. S. Cant and E. Mastorakos. *An introduction to turbulent reacting flows*. Imperial College Press, 2008.
- [29] X. Chai and K. Mahesh. Dynamic k -equation model for large-eddy simulation of compressible flows. *Journal of Fluid Mechanics*, 699:385–413, 2012.
- [30] N. Chakraborty, H. Kolla, R. Sankaran, E. R. Hawkes, J. H. Chen, and N. Swaminathan. Determination of three-dimensional quantities related to scalar dissipation rate and its transport from two-dimensional measurements: Direct Numerical Simulation based validation. *Proceedings of the Combustion Institute*, 34(1):1151 – 1162, 2013.
- [31] V. K. Chakravarthy and S. Menon. Subgrid modeling of turbulent premixed flames in the flamelet regime. *Flow, Turbulence and Combustion*, 65:133–161, 2000.
- [32] Y.-C. Chen, S. H. Stårner, and A. R. Masri. A detailed experimental investigation of well-defined, turbulent evaporating spray jets of acetone. *International Journal of Multiphase flow*, 32:389–412, 2006.
- [33] H. H. Chiu. Mesoscale structures of turbulent sprays. *Proceedings of the Combustion Institute*, 28(1):1095 – 1102, 2000.
- [34] H. H. Chiu, H. Y. Kim, and E. J. Croke. Internal group combustion of liquid droplets. *Symposium (International) on Combustion*, 19(1):971 – 980, 1982.
- [35] H. H. Chiu and T. M. Liu. Group combustion of liquid droplets. *Combustion Science and Technology*, 17(3-4):127–142, 1977.
- [36] C. Chong and S. Hochgreb. Measurements of laminar flame speeds of acetone/methane/air mixtures. *Combustion and Flame*, 158(8):490–500, 2011.
- [37] M. Chrigui, J. Gounder, A. Sadiki, J. Janicka, and A. R. Masri. Acetone droplet behavior in reacting and non reacting turbulent flow. *Flow, Turbulence and Combustion*, 90(2):419–447, 2013.

-
- [38] M. Chrigui, J. Gounder, A. Sadiki, A. R. Masri, and J. Janicka. Partially premixed reacting acetone spray using LES and FGM tabulated chemistry. *Combustion and Flame*, 159(8):2718 – 2741, 2012.
- [39] M. J. Cleary. *CMC Modelling of Enclosure Fires*. PhD thesis, University of Sydney, Sydney, Australia, 2004.
- [40] M. J. Cleary and J. H. Kent. Modelling of species in hood fires by conditional moment closure. *Combustion and Flame*, 143(4):357 – 368, 2005.
- [41] M. J. Cleary and A. Y. Klimenko. A detailed quantitative analysis of sparse-Lagrangian filtered density function simulations in constant and variable density reacting jet flows. *Physics of Fluids*, 23(11):115102, 2011.
- [42] P. J. Colucci, F. A. Jaber, P. Givi, and S. B. Pope. Filtered density function for large eddy simulation of turbulent reacting flows. *Physics of Fluids*, 10(2):499–515, 1998.
- [43] C. Crowe, M. Sommerfeld, and Y. Tsuji. *Multiphase flows with droplets and particles*. CRC Press, 1998.
- [44] C. T. Crowe, T. R. Troutt, and J. N. Chung. Numerical models for two-phase turbulent flows. *Annual Review of Fluid Mechanics*, 28(1):11–43, 1996.
- [45] P. A. Davidson. *Turbulence: An Introduction for Scientists and Engineers*. Oxford University Press, 2004.
- [46] S. De and S. H. Kim. Large eddy simulation of dilute reacting sprays: Droplet evaporation and scalar mixing. *Combustion and Flame*, 160(10):2048 – 2066, 2013.
- [47] S. De, K. N. Lakshmisha, and R. W. Bilger. Modeling of nonreacting and reacting turbulent spray jets using a fully stochastic separated flow approach. *Combustion and Flame*, 158(10):1992 – 2008, 2011.

- [48] C. B. Devaud, R. W. Bilger, and T. Liu. A new method of modeling the conditional scalar dissipation rate. *Physics of Fluids*, 16(6):2004–2011, 2004.
- [49] C. B. Devaud, I. Stanković, and B. Merci. Deterministic multiple mapping conditioning (MMC) applied to a turbulent flame in large eddy simulation (LES). *Proceedings of the Combustion Institute*, 34(1):1213 – 1221, 2013.
- [50] F. di Mare. *Large Eddy Simulation of Reacting and Non-reacting Turbulent Flows*. PhD thesis, Imperial College, London, UK, 2002.
- [51] D. Dietzel, D. Messig, F. Piscaglia, A. Montorfano, G. Olenik, O. T. Stein, A. Kronenburg, A. Onorati, and C. Hasse. Evaluation of scale resolving turbulence generation methods for Large Eddy Simulation of turbulent flows. *Computers & Fluids*, 93(0):116 – 128, 2014.
- [52] B. Duret, G. Luret, J. Réveillon, T. Menard, A. Berlemont, and F. X. Demoulin. DNS analysis of turbulent mixing in two-phase flows. *International Journal of Multiphase Flow*, 40(0):93 – 105, 2012.
- [53] V. R. Dushin, A. V. Kulchitskiy, V. A. Nerchenko, V. F. Nikitin, E. S. Osadchaya, Y. G. Phylippov, and N. N. Smirnov. Mathematical simulation for non-equilibrium droplet evaporation. *Acta Astronautica*, 63(11-12):1360 – 1371, 2008.
- [54] T. Echekki, A. R. Kerstein, T. D. Dreeben, and J.-Y. Chen. One-dimensional turbulence simulation of turbulent jet diffusion flames: model formulation and illustrative applications. *Combustion and Flame*, 125(3):1083 – 1105, 2001.
- [55] T. Echekki and E. Mastorakos. *Turbulent Combustion Modeling*. Springer, 2011.
- [56] J. R. Fessler, J. D. Kulick, and J. K. Eaton. Preferential concentration of heavy particles in a turbulent channel flow. *Physics of Fluids*, 6(11):3742, 1994.

-
- [57] R. O. Fox. *Computational Models for Turbulent Reacting Flows*. Cambridge University Press, 2003.
- [58] R. O. Fox. Large-eddy-simulation tools for multiphase flows. *Annual Review of Fluid Mechanics*, 44(1):47–76, 2012.
- [59] R. O. Fox, F. Laurent, and M. Massot. Numerical simulation of spray coalescence in an Eulerian framework: Direct quadrature method of moments and multi-fluid method. *Journal of Computational Physics*, 227(6):3058 – 3088, 2008.
- [60] B. Franzelli, B. Fiorina, and N. Darabiha. A tabulated chemistry method for spray combustion. *Proceedings of the Combustion Institute*, 34(1):1659 – 1666, 2013.
- [61] A. Garmory and E. Mastorakos. Capturing localised extinction in Sandia Flame F with LES-CMC. *Proceedings of the Combustion Institute*, 33(1):1673 – 1680, 2011.
- [62] H.-W. Ge and E. Gutheil. Probability density function (PDF) simulation of turbulent spray flows. *Atomization and Sprays*, 16(5):531–542, 2006.
- [63] Y. Ge, M. J. Cleary, and A. Y. Klimenko. A comparative study of Sandia flame series (D-F) using sparse-Lagrangian MMC modelling. *Proceedings of the Combustion Institute*, 34(1):1325 – 1332, 2013.
- [64] F. Génin and S. Menon. Studies of shock/turbulent shear layer interaction using Large-Eddy Simulation. *Computers & Fluids*, 39(5):800 – 819, 2010.
- [65] M. Germano, U. Piomelli, P. Moin, and W. H. Cabot. A dynamic subgrid-scale eddy viscosity model. *Physics of Fluids A*, 3(7):1760–1765, 1991.
- [66] O. Gicquel, N. Darabiha, and D. Thvenin. Laminar premixed hydrogen/air counterflow flame simulations using flame prolongation of ILDM with differential diffusion. *Proceedings of the Combustion Institute*, 28(2):1901 – 1908, 2000.

- [67] S. S. Girimaji. Assumed β -pdf model for turbulent mixing: Validation and extension to multiple scalar mixing. *Combustion Science and Technology*, 78(4-6):177–196, 1991.
- [68] S. S. Girimaji. On the modeling of scalar diffusion in isotropic turbulence. *Physics of Fluids A*, 4(11):2529–2537, 1992.
- [69] J. D. Gounder. *An experimental investigation of non-reacting and reacting spray jet*. PhD thesis, The University of Sydney, Sydney, Australia, 2009.
- [70] J. D. Gounder, A. Kourmatzis, and A. R. Masri. Turbulent piloted dilute spray flames: Flow fields and droplet dynamics. *Combustion and Flame*, 159(11):3372 – 3397, 2012.
- [71] D. W. Green and R. H. Perry. *Perry’s Chemical Engineers’ Handbook*. McGraw-Hill, New York, US, 8 th edition, 2008.
- [72] GRI-Mech Home Page. <http://www.me.berkeley.edu/gri-mech/>.
- [73] P. Gualtieri, F. Picano, G. Sardina, and C. M. Casciola. Clustering and turbulence modulation in particle laden shear flows. *Journal of Physics: Conference Series*, 333(1):012007, 2011.
- [74] C. Hasse. *A Two-Dimensional Flamelet Model for Multiple Injections in Diesel Engines*. PhD thesis, RWTH Aachen, Aachen, Germany, 2004.
- [75] D. C. Haworth. Progress in probability density function methods for turbulent reacting flows. *Progress in Energy and Combustion Science*, 36(2):168 – 259, 2010.
- [76] O. Herbinet, W. J. Pitz, and C. K. Westbrook. Detailed chemical kinetic oxidation mechanism for a biodiesel surrogate. *Combustion and Flame*, 154(3):507 – 528, 2008.

- [77] C. Heye, V. Raman, and A. R. Masri. LES/probability density function approach for the simulation of an ethanol spray flame. *Proceedings of the Combustion Institute*, 34(1):1633 – 1641, 2013.
- [78] M. Ihme and H. Pitsch. Modeling of radiation and nitric oxide formation in turbulent nonpremixed flames using a flamelet/progress variable formulation. *Physics of Fluids*, 20:055110, 2008.
- [79] M. Ihme and H. Pitsch. Prediction of extinction and reignition in nonpremixed turbulent flames using a flamelet/progress variable model: 2. Application in LES of Sandia flames D and E. *Combustion and Flame*, 155(1-2):90 – 107, 2008.
- [80] R. T. Imaoka and W. A. Sirignano. Transient vaporization and burning in dense droplet arrays. *International Journal of Heat and Mass Transfer*, 48(21-22):4354 – 4366, 2005.
- [81] R. T. Imaoka and W. A. Sirignano. Vaporization and combustion in three-dimensional droplet arrays. *Proceedings of the Combustion Institute*, 30(2):1981 – 1989, 2005.
- [82] P. Jenny, D. Roekaerts, and N. Beishuizen. Modeling of turbulent dilute spray combustion. *Progress in Energy and Combustion Science*, 38(6):846 – 887, 2012.
- [83] W. P. Jones, F. di Mare, and A. J. Marquis. *LES-BOFFIN: User's Guide*. 2002.
- [84] W. P. Jones, S. Lyra, and S. Navarro-Martinez. Numerical investigation of swirling kerosene spray flames using large eddy simulation. *Combustion and Flame*, 159(4):1539 – 1561, 2012.
- [85] W. P. Jones, A. J. Marquis, and K. Vogiatzaki. Large-eddy simulation of spray combustion in a gas turbine combustor. *Combustion and Flame*, 161(1):222 – 239, 2014.

- [86] W. P. Jones and V. N. Prasad. Large eddy simulation of the Sandia flame series (D-F) using the Eulerian stochastic field method. *Combustion and Flame*, 157(9):1621 – 1636, 2010.
- [87] I. Kataoka. Local instant formulation of two-phase flow. *International Journal of Multiphase Flow*, 12(5):745 – 758, 1986.
- [88] C. M. Kaul, V. Raman, E. Knudsen, E. S. Richardson, and J. H. Chen. Large eddy simulation of a lifted ethylene flame using a dynamic nonequilibrium model for subfilter scalar variance and dissipation rate. *Proceedings of the Combustion Institute*, 34(1):1289 – 1297, 2013.
- [89] A. Kempf, H. Forkel, J.-Y. Chen, A. Sadiki, and J. Janicka. Large-eddy simulation of a counterflow configuration with and without combustion. *Proceedings of the Combustion Institute*, 28(1):35 – 40, 2000.
- [90] G. Kim, S. Kang, Y. Kim, R. W. Bilger, and M. J. Cleary. Conditional moment closure and transient flamelet modelling for detailed structure and NO_x formation characteristics of turbulent nonpremixed jet and recirculating flames. *Combustion Theory and Modelling*, 11(4):527–552, 2007.
- [91] W. T. Kim and K. Y. Huh. Numerical simulation of spray autoignition by the first-order conditional moment closure model. *Proceedings of the Combustion Institute*, 29:569–576, 2002.
- [92] W.-W. Kim and S. Menon. An unsteady incompressible Navier-Stokes solver for large eddy simulation of turbulent flows. *International Journal for Numerical Methods in Fluids*, 31(6):983–1017, 1999.
- [93] T. Kitano, J. Nishio, R. Kurose, and S. Komori. Effects of ambient pressure, gas temperature and combustion reaction on droplet evaporation. *Combustion and Flame*, 161(2):551 – 564, 2014.

-
- [94] M. Klein, A. Sadiki, and J. Janicka. A digital filter based generation of in-flow data for spatially developing direct numerical or large eddy simulations. *Journal of Computational Physics*, 186(2):652 – 665, 2003.
- [95] A. Y. Klimenko. Multicomponent diffusion of various admixtures in turbulent flow. *Fluid Dynamics*, 25(3):327–334, 1990.
- [96] A. Y. Klimenko and R. W. Bilger. Conditional moment closure for turbulent combustion. *Progress in Energy and Combustion Science*, 25:595–687, 1999.
- [97] A. Y. Klimenko and S. B. Pope. The modeling of turbulent reactive flows based on multiple mapping conditioning. *Physics of Fluids*, 15(7):1907–1925, 2003.
- [98] D. I. Kolaitis and M. A. Founti. A comparative study of numerical models for Eulerian-Lagrangian simulations of turbulent evaporating sprays. *International Journal of Heat and Fluid Flow*, 27(3):424 – 435, 2006.
- [99] A. Kronenburg. Double conditioning of reactive scalar transport equations in turbulent non-premixed flames. *Physics of Fluids*, 16:7:2640–2648, 2004.
- [100] A. Kronenburg, R. W. Bilger, and J. H. Kent. Computation of conditional average scalar dissipation in turbulent jet diffusion flames. *Flow, Turbulence and Combustion*, 64:145–159, 2000.
- [101] A. Kronenburg and M. Kostka. Modeling extinction and reignition in turbulent flames. *Combustion and Flame*, 143(4):342 – 356, 2005.
- [102] A. Kronenburg and A. E. Papoutsakis. Conditional moment closure modeling of extinction and re-ignition in turbulent non-premixed flames. *Proceedings of the Combustion Institute*, 30(1):759 – 766, 2005.
- [103] J. W. Labahn and C. B. Devaud. Investigation of conditional source-term estimation applied to a non-premixed turbulent flame. *Combustion Theory and Modelling*, 17(5):960–982, 2013.

-
- [104] C. K. Law. Combustion at a crossroads: Status and prospects. *Proceedings of the Combustion Institute*, 31(1):1 – 29, 2007.
- [105] P. C. Le Clercq and J. Bellan. Direct numerical simulation of gaseous mixing layers laden with multicomponent-liquid drops: liquid-specific effects. *Journal of Fluid Mechanics*, 533:57–94, 6 2005.
- [106] D. K. Lilly. A proposed modification of the Germano subgrid-scale closure method. *Physics of Fluids A*, 4(3):633–635, 1992.
- [107] E. Loth. Numerical approaches for motion of dispersed particles, droplets and bubbles. *Progress in energy and combustion science*, 26:161–223, 2000.
- [108] T. Lu and C. K. Law. Toward accommodating realistic fuel chemistry in large-scale computations. *Progress in Energy and Combustion Science*, 35(2):192 – 215, 2009.
- [109] K. Luo, H. Pitsch, M. G. Pai, and O. Desjardins. Direct numerical simulations and analysis of three-dimensional n-heptane spray flames in a model swirl combustor. *Proceedings of the Combustion Institute*, 33(2):2143 – 2152, 2011.
- [110] U. Maas and S. Pope. Simplifying chemical kinetics: Intrinsic low-dimensional manifolds in composition space. *Combustion and Flame*, 88(3-4):239 – 264, 1992.
- [111] A. Mahashabde, P. Wolfe, A. Ashok, C. Dorbian, Q. He, A. Fan, S. Lukachko, A. Mozdzanowska, C. Wollersheim, S. R. Barrett, M. Locke, and I. A. Waitz. Assessing the environmental impacts of aircraft noise and emissions. *Progress in Aerospace Sciences*, 47(1):15 – 52, 2011.
- [112] A. R. Masri. private communication, 2012.
- [113] A. R. Masri and J. D. Gounder. Turbulent spray flames of acetone and ethanol approaching extinction. *Combustion Science and Technology*, 182(4):702–715, 2010.

-
- [114] M. R. Maxey and J. J. Riley. Equation of motion for a small rigid sphere in a nonuniform flow. *Physics of Fluids*, 26(4):883–889, 1983.
- [115] R. D. Meester, B. Naud, U. Maas, and B. Merci. Transported scalar PDF calculations of a swirling bluff body flame (‘SM1’) with a reaction diffusion manifold. *Combustion and Flame*, 159(7):2415 – 2429, 2012.
- [116] C. Meneveau and J. Katz. Scale-invariance and turbulence models for large-eddy simulation. *Annual Review of Fluid Mechanics*, 32(1):1–32, 2000.
- [117] S. Menon and N. Patel. Subgrid modeling for simulation of spray combustion in large-scale combustors. *AIAA Journal*, 44:709–723, 2006.
- [118] B. Merci, D. Roekaerts, and A. Sadiki. *Experiments and Numerical Simulations of Diluted Spray Turbulent Combustion*. Springer, 2011.
- [119] K. Miki and S. Menon. Localized dynamic subgrid closure for simulation of magnetohydrodynamic turbulence. *Physics of Plasmas*, 15:072306, 2008.
- [120] A. Milford and C. B. Devaud. Investigation of an inhomogeneous turbulent mixing model for conditional moment closure applied to autoignition. *Combustion and Flame*, 157(8):1467 – 1483, 2010.
- [121] R. S. Miller, S. H. Frankel, C. K. Madnia, and P. Givi. Johnson-edgeworth translation for probability modeling of binary scalar mixing in turbulent flows. *Combustion Science and Technology*, 91(1-3):21–52, 1993.
- [122] R. S. Miller, K. Harstad, and J. Bellan. Evaluation of equilibrium and non-equilibrium evaporation models for many-droplet gas-liquid flow simulations. *International Journal of Multiphase Flow*, 24:1025–1055, 1998.
- [123] P. Moin and S. V. Apte. Large-eddy simulation of realistic gas turbine combustors. *AIAA Journal*, 44:698–708, 2006.

-
- [124] R. Monchaux, M. Bourgoïn, and A. Cartellier. Analyzing preferential concentration and clustering of inertial particles in turbulence. *International Journal of Multiphase Flow*, 40:1 – 18, 2012.
- [125] M. Mortensen. Consistent modeling of scalar mixing for presumed, multiple parameter probability density functions. *Physics of Fluids*, 17(1):018106, 2005.
- [126] M. Mortensen and R. Bilger. Derivation of the conditional moment closure equations for spray combustion. *Combustion and Flame*, 156(1):62 – 72, 2009.
- [127] M. Mortensen and S. M. de Bruyn Kops. Conditional velocity statistics in the double scalar mixing layer - A mapping closure approach. *Combustion Theory and Modelling*, 12(5):929–941, 2008.
- [128] M. Nakamura, F. Akamatsu, R. Kurose, and M. Katsuki. Combustion mechanism of liquid fuel spray in a gaseous flame. *Physics of Fluids*, 17(12):123301, 2005.
- [129] S. Navarro-Martinez and A. Kronenburg. LES-CMC simulations of a turbulent bluff-body flame. *Proceedings of the Combustion Institute*, 31:1721–1728, 2007.
- [130] S. Navarro-Martinez and A. Kronenburg. LES-CMC simulations of a turbulent a lifted methane flame. *Proceedings of the Combustion Institute*, 32:1509–1516, 2009.
- [131] S. Navarro-Martinez and A. Kronenburg. Flame stabilization mechanisms in lifted flames. *Flow, Turbulence and Combustion*, 87:377–406, 2011.
- [132] S. Navarro-Martinez, A. Kronenburg, and F. di Mare. Conditional moment closure for large eddy simulations. *Flow, Turbulence and Combustion*, 75:245–274, 2005.
- [133] Y.-S. Niu, L. Vervisch, and P. D. Tao. An optimization-based approach to detailed chemistry tabulation: Automated progress variable definition. *Combustion and Flame*, 160(4):776 – 785, 2013.

- [134] E. E. O'Brien and T.-L. Jiang. The conditional dissipation rate of an initially binary scalar in homogeneous turbulence. *Physics of Fluids A*, 3(12):3121–3123, 1991.
- [135] J. A. V. Oijen and L. P. H. D. Goey. Modelling of premixed laminar flames using flamelet-generated manifolds. *Combustion Science and Technology*, 161(1):113–137, 2000.
- [136] H. Olguin and E. Gutheil. Influence of evaporation on spray flamelet structures. *Combustion and Flame*, 161(4):987–996, 2013.
- [137] S. S. Patwardhan, S. De, K. N. Lakshmisha, and B. N. Raghunandan. CMC simulations of lifted turbulent jet flame in a vitiated coflow. *Proceedings of the Combustion Institute*, 32(2):1705 – 1712, 2009.
- [138] C. Pera, J. Réveillon, L. Vervisch, and P. Domingo. Modeling subgrid scale mixture fraction variance in LES of evaporating spray. *Combustion and Flame*, 146:635–648, 2006.
- [139] I. Pasmazoglou, A. M. Kempf, and S. Navarro-Martinez. A dynamic model for the Lagrangian stochastic dispersion coefficient. *Physics of Fluids*, 25(12):125108, 2013.
- [140] N. Peters. *Turbulent Combustion*. Cambridge University Press, Cambridge, UK, 2000.
- [141] N. Peters. Multiscale combustion and turbulence. *Proceedings of the Combustion Institute*, 32(1):1 – 25, 2009.
- [142] S. Pichon, G. Black, N. Chaumeix, M. Yahyaoui, J. M. Simmie, H. J. Curran, and R. Donohue. The combustion chemistry of a fuel tracer: Measured flame speeds and ignition delays and a detailed chemical kinetic model for the oxidation of acetone. *Combustion and Flame*, 156(2):494 – 504, 2009.

-
- [143] C. D. Pierce and P. Moin. A dynamic model for subgrid-scale variance and dissipation rate of a conserved scalar. *Physics of Fluids*, 10(12):3041–3044, 1998.
- [144] C. D. Pierce and P. Moin. Progress-variable approach for large-eddy simulation of non-premixed turbulent combustion. *Journal of Fluid Mechanics*, 504:73–97, 4 2004.
- [145] H. Pitsch. Large-eddy simulation of turbulent combustion. *Annual Review of Fluid Mechanics*, 38(1):453–482, 2006.
- [146] T. Poinsot and D. Veynante. *Theoretical Numerical Combustion*. Edwards, Philadelphia, USA, 2005.
- [147] S. B. Pope. PDF methods for turbulent reactive flows. *Progress in Energy and Combustion Science*, 11:119–192, 1985.
- [148] S. B. Pope. *Turbulent Flows*. Cambridge University Press, Cambridge, UK, 2001.
- [149] S. B. Pope. Small scales, many species and the manifold challenges of turbulent combustion. *Proceedings of the Combustion Institute*, 34(1):1 – 31, 2013.
- [150] J. Pozorski and S. V. Apte. Filtered particle tracking in isotropic turbulence and stochastic modeling of subgrid-scale dispersion. *International Journal of Multiphase Flow*, 35(2):118 – 128, 2009.
- [151] J. Réveillon and F. X. Demoulin. Evaporating droplets in turbulent reacting flows. *Proceedings of the Combustion Institute*, 31(2):2319 – 2326, 2007.
- [152] J. Réveillon and L. Vervisch. Spray vaporization in nonpremixed turbulent combustion modeling: a single droplet model. *Combustion and Flame*, 121(1-2):75 – 90, 2000.

- [153] J. Réveillon and L. Vervisch. Analysis of weakly turbulent dilute-spray flames and spray combustion regimes. *Journal of Fluid Mechanics*, 537:317–347, 8 2005.
- [154] J. W. Rogerson, J. H. Kent, and R. W. Bilger. Conditional moment closure in a bagasse-fired boiler. *Proceedings of the Combustion Institute*, 31(2):2805 – 2811, 2007.
- [155] S. Russo and A. Gomez. Structure of laminar coflow spray flames at different pressures. *Proceedings of the Combustion Institute*, 29(1):601 – 608, 2002.
- [156] J. Shinjo and A. Umemura. Simulation of liquid jet primary breakup: Dynamics of ligament and droplet formation. *International Journal of Multiphase Flow*, 36(7):513 – 532, 2010.
- [157] B. Shotorban and S. Balachandar. A Eulerian model for large-eddy simulation of concentration of particles with small Stokes numbers. *Physics of Fluids*, 19(11):118107, 2007.
- [158] W. A. Sirignano. *Fluid Dynamics and Transport of Droplets and Sprays*. Cambridge University Press, 1999.
- [159] P. Siwaborworn. *Conservative LES-CMC Modelling for Turbulent Jet Flames*. PhD thesis, Universität Stuttgart, Stuttgart, Germany, 2013.
- [160] P. Siwaborworn and A. Kronenburg. Conservative implementation of LES-CMC for turbulent jet flames. In W. E. Nagel, D. H. Köner, and M. M. Resch, editors, *High Performance Computing in Science and Engineering '12*, pages 159–173. Springer, 2013.
- [161] J. Smagorinsky. General circulation experiments with the primitive equations I. The basic experiment. *American Meteorological Society*, 91:99–164, 1963.
- [162] L. D. Smoot and P. J. Smoth. *Coal Combustion and Gasification*. Plenum Press, New York, USA, 1985.

- [163] R. J. Sornek and R. Dobashi. Effect of turbulence on spatial distribution and group behavior of droplet in a spray flame. *Combustion Science and Technology*, 161(1):191–211, 2000.
- [164] S. Sreedhara, Y. Lee, K. Y. Huh, and D. H. Ahn. Comparison of submodels for conditional velocity and scalar dissipation in CMC simulation of piloted jet and bluff-body flames. *Combustion and Flame*, 152(1-2):282 – 286, 2008.
- [165] I. Stanković, E. Mastorakos, and B. Merci. LES-CMC simulations of different auto-ignition regimes of hydrogen in a hot turbulent air co-flow. *Flow, Turbulence and Combustion*, 90(3):583–604, 2013.
- [166] R. Stauch and U. Maas. The ignition of methanol droplets in a laminar convective environment. *Combustion and Flame*, 153(1-2):45 – 57, 2008.
- [167] H. Steiner and W. K. Bushe. Large eddy simulation of a turbulent reacting jet with conditional source-term estimation. *Physics of Fluids*, 13(3):754–796, 2001.
- [168] N. Swaminathan and R. W. Bilger. Assessment of combustion submodels for turbulent nonpremixed hydrocarbon flames. *Combustion and Flame*, 116(4):519 – 545, 1999.
- [169] B. Thornber, R. W. Bilger, A. R. Masri, and E. R. Hawkes. An algorithm for LES of premixed compressible flows using the conditional moment closure model. *Journal of Computational Physics*, 230(20):7687 – 7705, 2011.
- [170] TNF Workshop. <http://www.sandia.gov/tnf/abstract.html>.
- [171] S. R. Turns. *An introduction to combustion*. McGraw-Hill, University Park, USA, 2000.
- [172] A. Tyliczszak, E. Cavaliere, Davide, and E. Mastorakos. LES/CMC of blow-off in a liquid fueled swirl burner. *Flow, Turbulence and Combustion*, 92(1-2):237–267, 2013.

- [173] S. Ukai, K. Balakrishnan, and S. Menon. On Richtmyer–Meshkov instability in dilute gas-particle mixtures. *Physics of Fluids*, 22(10):104103, 2010.
- [174] S. Ukai, A. Kronenburg, and O. T. Stein. Large eddy simulation of turbulent evaporating acetone spray jets. Cardiff, 2011. Proceedings of 5th European Combustion Meeting.
- [175] S. Ukai, A. Kronenburg, and O. T. Stein. LES-CMC of a dilute acetone spray flame. *Proceedings of the Combustion Institute*, 34(1):1643 – 1650, 2013.
- [176] S. Ukai, A. Kronenburg, and O. T. Stein. Simulation of dilute acetone spray flames with LES-CMC using two conditional moments. *Flow, Turbulence and Combustion*, 93(3):405–423, 2014.
- [177] S. Ukai, A. Kronenburg, and O. T. Stein. Large eddy simulation of dilute acetone spray flames using CMC coupled with tabulated chemistry. *Proceedings of the Combustion Institute*, 35(2):1667 – 1674, 2015.
- [178] A. Umemura and S. Takamori. Percolation theory for flame propagation in non- or less-volatile fuel spray: A conceptual analysis to group combustion excitation mechanism. *Combustion and Flame*, 141(4):336 – 349, 2005.
- [179] U.S. Energy Information Administration. International energy outlook 2013.
- [180] U.S. Energy Information Administration. January 2014 monthly energy review.
- [181] L. Vervisch. Using numerics to help the understanding of non-premixed turbulent flames. *Proceedings of the Combustion Institute*, 28(1):11 – 24, 2000.
- [182] K. Vogiatzaki. *Stochastic and deterministic multiple mapping conditioning for turbulent reacting jets*. PhD thesis, Imperial College, London, UK, 2009.
- [183] K. Vogiatzaki, M. J. Cleary, A. Kronenburg, and J. H. Kent. Modeling of scalar mixing in turbulent jet flames by multiple mapping conditioning. *Physics of Fluids*, 21(2):025105, 2009.

- [184] K. Vogiatzaki, A. Kronenburg, M. J. Cleary, and J. H. Kent. Multiple mapping conditioning of turbulent jet diffusion flames. *Proceedings of the Combustion Institute*, 32(2):1679 – 1685, 2009.
- [185] K. Vogiatzaki, A. Kronenburg, S. Navarro-Martinez, and W. P. Jones. Stochastic multiple mapping conditioning for a piloted, turbulent jet diffusion flame. *Proceedings of the Combustion Institute*, 33(1):1523 – 1531, 2011.
- [186] A. W. Vreman, B. A. Albrecht, J. A. van Oijen, L. P. H. de Goey, and R. Bastiaans. Premixed and nonpremixed generated manifolds in large-eddy simulation of Sandia flame D and F. *Combustion and Flame*, 153(3):394 – 416, 2008.
- [187] A. P. Wandel, N. Chakraborty, and E. Mastorakos. Direct numerical simulations of turbulent flame expansion in fine sprays. *Proceedings of the Combustion Institute*, 32(2):2283 – 2290, 2009.
- [188] H. Watanabe, R. Kurose, S. Komori, and H. Pitsch. Effects of radiation on spray flame characteristics and soot formation. *Combustion and Flame*, 152(1-2):2 – 13, 2008.
- [189] M. Wille. *Large eddy simulation of jets in cross flows*. PhD thesis, Imperial College, London, UK, 1997.
- [190] Y. Wright, O.-N. Margari, K. Boulouchos, G. De Paola, and E. Mastorakos. Experiments and simulations of n-heptane spray auto-ignition in a closed combustion chamber at diesel engine conditions. *Flow Turbulence and Combustion*, 84:49–78, 2010.
- [191] Y. M. Wright, G. D. Paola, K. Boulouchos, and E. Mastorakos. Simulations of spray autoignition and flame establishment with two-dimensional CMC. *Combustion and Flame*, 143(4):402 – 419, 2005.
- [192] H. Yoshimoto and S. Goto. Self-similar clustering of inertial particles in homogeneous turbulence. *Journal of Fluid Mechanics*, 577:275–286, 4 2007.

-
- [193] M. R. G. Zoby, S. Navarro-Martinez, A. Kronenburg, and A. J. Marquis. Evaporation rates of droplet arrays in turbulent reacting flows. *Proceedings of the Combustion Institute*, 33(2):2117 – 2125, 2011.
- [194] M. R. G. Zoby, S. Navarro-Martinez, A. Kronenburg, and A. J. Marquis. Turbulent mixing in three-dimensional droplet arrays. *International Journal of Heat and Fluid Flow*, 32:499–509, 2011.

Appendix A

Conditional Scalar Dissipation in Two-Phase Flows

The accurate prediction of conditional scalar dissipation rates is of primary importance for CMC simulations. Approaches developed in past studies can be mainly sorted into two categories: macroscopic and microscopic. Here, a macroscopic approach is defined as the methodology where subgrid model are a function of filtered quantities, and a microscopic approach is understood as an approach to construct subgrid (or micro-sized) structures in detail at or around the droplets. This appendix briefly reviews both approaches.

A.1 Macroscopic Approach

In the macroscopic approach, the conditional scalar dissipation rate is constructed taking samples from the LES cells as discussed in Sec. 4.3.2. Therefore, the modelling of the filtered subgrid scalar dissipation, \widetilde{N}_{sgs} , plays an important role. The scalar dissipation rate is closely connected with the mixture fraction variance, $\widetilde{\xi''^2}$, as often modelled as

$$\widetilde{N}_{sgs} = \frac{1}{2} \frac{\mu_t}{Sc_t \Delta^2 C_\xi} \widetilde{\xi''^2}. \quad (\text{A.1})$$

One of the simplest models to estimate the mixture fraction variance is an algebraic model that is based on local mixture fraction gradients as

$$\widetilde{\xi''^2} = C_\xi \Delta^2 \left(\frac{\partial \tilde{\xi}}{\partial x_j} \right)^2, \quad (\text{A.2})$$

where C_ξ is usually set to equal $C_\xi = 0.09$ [132]. Another approach is to solve a transport equation of the mixture fraction variance for two-phase flow written as

$$\frac{\partial}{\partial t} (\bar{\rho} \widetilde{\xi''^2}) + \frac{\partial}{\partial x_j} (\bar{\rho} \widetilde{u_j \xi''^2}) = \frac{\partial}{\partial x_j} \left[\left(\bar{\rho} D + \frac{\mu_t}{S_{c_t}} \right) \frac{\partial \widetilde{\xi''^2}}{\partial x_j} \right] - 2\bar{\rho} \widetilde{N}_{sgs} + 2 \frac{\mu_t}{S_{c_t}} \left(\frac{\partial \tilde{\xi}}{\partial x_j} \right)^2 + \sigma_s, \quad (\text{A.3})$$

where σ_s is the source term associated with the evaporation process are given by

$$\sigma_s = 2\bar{\rho} (\widetilde{\xi \Pi} - \widetilde{\xi} \widetilde{\Pi}) + \bar{\rho} (\widetilde{\xi^2 \Pi} - \widetilde{\xi}^2 \widetilde{\Pi}), \quad (\text{A.4})$$

and three different closures were suggested as listed in Table A.1. Model 1 was developed by Pera et al. [138] and is fully based on the local quantities within the cell. Model 2 is used by Borghesi et al. [20], and it computes filtered terms by summing up the droplet evaporation given by the Lagrangian particle tracking method. Then, Model 3 was proposed by Revillon and Vervisch [152] and couples the subgrid scale spray evaporation with filtered quantities. These models are tested by simulating the spray flames with conditional moments obtained a priori by using the algebraic model (see Chapter 7). The transport equations are solved with the respective closures, and results are compared to the algebraic model. Note that the conditional moments are unchanged during the simulation to focus on the analysis of $\widetilde{\xi''^2}$ excluding the coupling by N_η in the CMC equations.

Fig. A.1 shows the mixture fraction variances computed by each approach, and it becomes immediately apparent that notable differences exist. Not only the magnitude of the variance is different, but also the profile shapes. For example, the algebraic model and Model 1 show small $\widetilde{\xi''^2}$ at the center of the jet near the inlet, but Models 2 and 3 predict large $\widetilde{\xi''^2}$ at the same location. Also, the maximum value

Table A.1: Closures of σ_s based on the variance transport equation. $\widetilde{\Pi}$ is the volume expansion rate per unit volume, $\widetilde{\Pi} = \frac{1}{\rho V} \sum_{i=1}^{N_d} \dot{m}_i$, \dot{m}_i is the mass evaporation rate of i -th droplet, N_d is the number of the droplets per LES cell, V is the cell volume, and ξ_{surf} is the mixture fraction at each droplet surface.

Model 1 [138]	$\sigma_s = \alpha \bar{\rho} \widetilde{\xi''^2} (\widetilde{\Pi} / \widetilde{\xi})$ $\alpha = 0.5$
Model 2 [20]	$\sigma_s = 2\bar{\rho}(\widetilde{\xi\Pi} - \widetilde{\xi\Pi}) + \bar{\rho}(\widetilde{\xi^2\Pi} - \widetilde{\xi^2\Pi})$ $\widetilde{\xi\Pi} = \frac{1}{\rho V} \sum_{i=1}^{N_d} \xi_{s,i} \dot{m}_i, \quad \widetilde{\xi^2\Pi} = \frac{1}{\rho V} \sum_{i=1}^{N_d} \xi_{s,i}^2 \dot{m}_i$
Model 3 [152]	$\sigma_s = 2\bar{\rho} \widetilde{\xi''^2} \Pi (1 - \widetilde{\xi}) - \bar{\rho} \widetilde{\xi''^2} \Pi$ $\widetilde{\xi''^2} \Pi = \frac{1}{\rho V} \sum_{i=1}^{N_d} \sqrt{\xi''^2} \dot{m}_i, \quad \widetilde{\xi''^2} \Pi = \frac{1}{\rho V} \sum_{i=1}^{N_d} \xi''^2 \dot{m}_i$

in Model 2 is found to be 5×10^{-4} whereas the algebraic model and Model 1 predict peak values almost two orders of magnitude lower. This implies the variance source term estimated by Model 2 is at least two orders of magnitude larger than the shear production term (third term in Eqn. A.3). Such a large $\widetilde{\xi''^2}$ might lead to a large scalar dissipation rate (Eqn. A.1) that can extinguish flames. Therefore, the current study is based on the algebraic model, and the scalar dissipation rates is estimated with the correction factor (see Sec. 2.4).

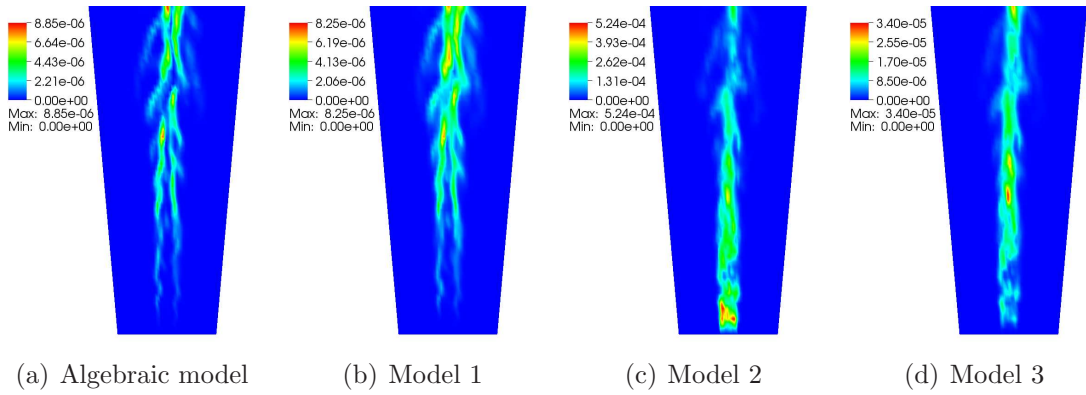


Figure A.1: Comparisons of the mixture fraction variances.

A.2 Microscopic Approach

While the macroscopic approach provides scalar dissipation as a function of other filtered quantities, a microscopic approach attempts to obtain detailed information around small scale structures. However, there is no simple model applicable to general flow fields. Fully resolved DNS is currently the only approach to obtain all the necessary statistics, but it is not computationally tractable. Therefore, this section introduces two methodologies investigated in the past literature: conditioning on droplet surface quantities and a single droplet stationary flow assumption.

A.2.1 Conditioning on Droplet Surface

Borghesi et al. [20] have discussed the scalar dissipation and PDF on the spray surface. They applied the surface density, Σ_s , and the gradient as

$$P(\xi_{surf}) \langle |\nabla \xi| | \xi_{surf} \rangle = \Sigma_s. \quad (\text{A.5})$$

Since the surface density and the gradient of mixture fraction at the surface can be given as

$$\Sigma_s = \frac{1}{V} \sum_{i=1}^{N_{d,\xi_{surf}}} 4\pi r_i^2, \quad (\text{A.6})$$

$$\langle |\nabla \xi| | \xi_{surf} \rangle = \ln[1 + B_{m,v}] Sh \frac{1 - \xi_{surf}}{2r}, \quad (\text{A.7})$$

where $N_{d,\xi_{surf}}$ is the number density with the specific surface mixture fraction, $B_{m,v}$ is the Spalding number for the vapour, r is the radius of the droplet, and Sh is the Sherwood number. Then, the PDF of the surface condition can be given as

$$P(\xi_{surf}) = \frac{\Sigma_s}{\langle |\nabla \xi| | \xi_{surf} \rangle} = \frac{N_{d,\xi_{surf}}}{V} \frac{\sum_{i=1}^{N_{d,\xi_{surf}}} 4\pi r_i^2}{\sum_{i=1}^{N_{d,\xi_{surf}}} \ln[1 + B_{m,v}] Sh \frac{1 - \xi_{surf}}{2r}}. \quad (\text{A.8})$$

Also, conditional scalar dissipation on the droplet surface can be estimated based on the local gradient as

$$\langle N|\xi_{surf}\rangle = D \langle \nabla \xi^2|\xi_{surf}\rangle = \frac{D}{N_{d,\xi_{surf}}} \sum_{i=1}^{N_{d,\xi_{surf}}} \left(\ln[1 + B_{m,v}] Sh \frac{1 - \xi_{surf}}{2r} \right)^2. \quad (\text{A.9})$$

They have also carried extra validation of the model based on the transported PDF model as discussed by Kronenburg et al. [100]. The two-phase PDF transport equation obtained by Mortensen and Bilger [126] is given by

$$\begin{aligned} & \frac{\partial \rho(\eta) P_\eta}{\partial t} + \nabla \cdot (\langle \rho u|\eta \rangle P_\eta) + \frac{\partial^2}{\partial \eta^2} (\langle \rho N|\eta \rangle P_\eta) \\ & = \nabla \cdot (\langle \rho D|\eta \rangle P_\eta) - \frac{\partial \rho(1 - \eta) \langle \pi|\eta \rangle P_\eta}{\partial \eta} + \rho \langle \pi|\eta \rangle P_\eta. \end{aligned} \quad (\text{A.10})$$

In stationary environments, Eqn. A.10 can be re-written as [20]

$$\rho \langle N|\xi_{surf}\rangle P(\xi_{surf}) = \rho \int_{\xi_{surf}}^1 (1 - \xi_{surf}) \langle \pi \rangle P(\eta^o) d\eta^o. \quad (\text{A.11})$$

Then, it is shown that the equation is satisfied when using the models presented in Eqns. A.8 and A.9.

The advantages of the approach are that the model can be valid even in a complex flow field, and it can also handle polydispersed droplet clouds at the same time. However, the PDF and the conditional scalar dissipation rate of the mixture fraction are given *only* at surface, but not for values between the filtered mean and at the surface ($\tilde{\xi}_{LES} < \xi < \xi_{surf}$). Therefore, it is difficult to establish a subgrid model applicable in an LES studies (also see Secs. 7.1.3 and 7.1.4).

A.2.2 Droplet in Stationary Flow

Bilger [12] has derived conditional scalar dissipation around a stationary spherical isolated droplet. As the results, the following expressions are given as

$$\langle N|\eta \rangle = \frac{D}{r_s^2} \frac{[\ln(1 - \eta)]^4}{[\ln(1 + B)]^2} (1 - \eta)^2, \quad (\text{A.12})$$

$$P(\eta) \equiv \frac{\Sigma_\eta}{\langle |\nabla \xi| |\eta \rangle} = 3f_v \frac{[\ln(1-B)]^3}{[\ln(1-\eta)]^4 (1-\eta)}, \quad (\text{A.13})$$

where r_s is the radius of the droplet, $B = \frac{\xi_{surf} - \xi_\infty}{1 - \xi_{surf}}$, f_v is the volume fraction of the droplets and Σ_η and $\langle |\nabla \xi| |\eta \rangle$ are defined as

$$\Sigma_\eta = \frac{3f_v [\ln(1+B)]^2}{r_s [\ln(1-\eta)]^2}, \quad (\text{A.14})$$

$$\langle |\nabla \xi| |\eta \rangle = \frac{[\ln(1-\eta)]^2 (1-\eta)}{[\ln(1+B)] r_s}. \quad (\text{A.15})$$

Note that $\frac{1}{1-\eta}$ in Eqn. A.13 is missing in the original paper.

The advantage of Bilger's model is that it can model the PDF and N_η between the far field and ξ_{surf} . Bilger only considered far field condition as $\xi_\infty = 0.0$, and it should be generalized for variable ξ_∞ . In the LES context, ξ_∞ can be selected as a filtered cell value, $\xi_\infty = \tilde{\xi}_{LES}$, and models (Eqns. A.12 - A.15) are modified as

$$\langle N|\eta \rangle = \frac{D}{r_s^2} \frac{\left[\ln \left(\frac{1-\eta}{1-\tilde{\xi}_{LES}} \right) \right]^4}{[\ln(1+B)]^2} (1-\eta)^2, \quad (\text{A.16})$$

$$P(\eta) \equiv \frac{\Sigma_\eta}{\langle |\nabla \xi| |\eta \rangle} = 3f_v \frac{[\ln(1-B)]^3}{\left[\ln \left(\frac{1-\eta}{1-\tilde{\xi}_{LES}} \right) \right]^4 (1-\eta)}, \quad (\text{A.17})$$

$$\Sigma_\eta = \frac{3f_v [\ln(1+B)]^2}{r_s \left[\ln \left(\frac{1-\eta}{1-\tilde{\xi}_{LES}} \right) \right]^2}, \quad (\text{A.18})$$

$$\langle |\nabla \xi| |\eta \rangle = \frac{\left[\ln \left(\frac{1-\eta}{1-\tilde{\xi}_{LES}} \right) \right]^2}{[\ln(1+B)] r_s} (1-\eta). \quad (\text{A.19})$$

The scalar dissipation rates obtained by macroscopic and microscopic approaches are shown in Fig. A.2. The macroscopic approach (with Model 1) shows \tilde{N}_{sgs} in the order of 0.01 1/s, whereas the microscopic model results $\langle N|\eta \rangle$ near droplet surface (1000 1/s) that is several orders of magnitude greater than the filtered dissipation rates due to very sharp gradients near the droplet surface. Since the droplet size is assumed to be very small compared to the grid size, $\langle N|\eta \rangle$ near the droplet surface

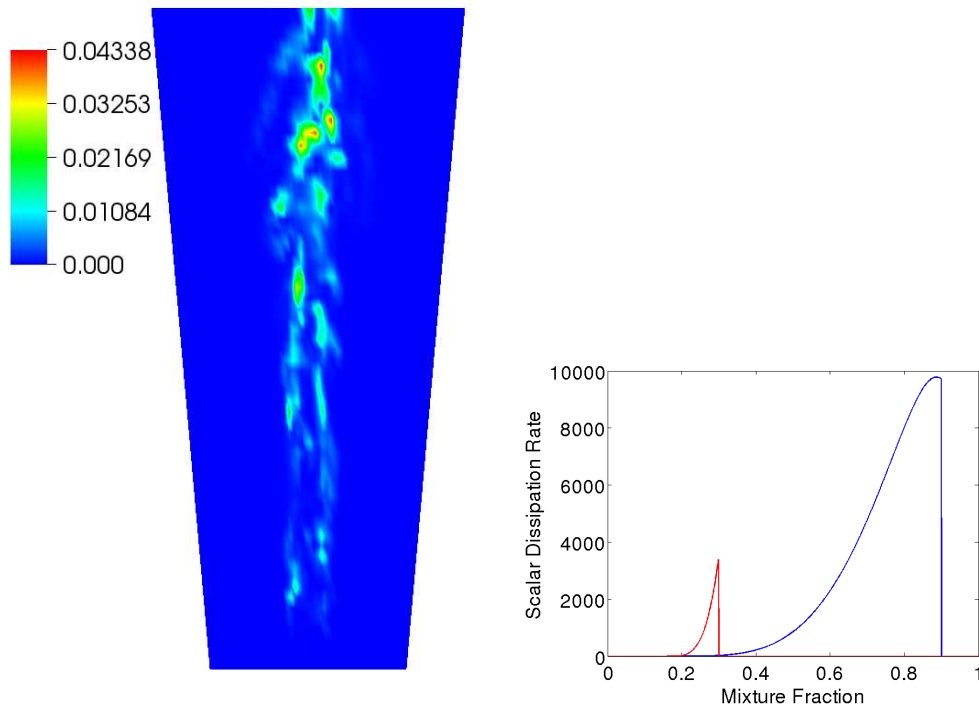
should always be larger than the filtered quantity. Such a large $\langle N|\eta \rangle$ implies that the time scale of vapour dissipation is very small and cannot be resolved within one CFD time step. In practical simulations, turbulence and shear flows increase the scalar dissipation rate further, so it might be adequate to assume fast mixing between $\tilde{\xi}$ and ξ_{surf} . Thus, a linear relation such as

$$Q_\alpha(\eta) = Q_\alpha(\tilde{\xi}_{LES}) + \frac{\eta - \tilde{\xi}_{LES}}{\xi_S - \tilde{\xi}_{LES}} [Q_\alpha(\xi_{surf}) - Q_\alpha(\tilde{\xi}_{LES})] \quad (\text{A.20})$$

can be assumed. However, there are still some difficulties to apply such models. One example is estimation of the probability ($P(\eta)$) between $\tilde{\xi}$ and ξ_{surf} where the relative motion to the surrounding gas is non-zero. Also, if the particle cloud is polydispersed, multiple conditional moments exist whereas only one solution is usually available in a CMC solution. It might be possible to have an ensemble average within the LES cell, but a numerical procedure to compute the PDF around every particle would be expensive.

A.3 Discussion and Summary

In this appendix, two different approaches are reviewed and analyzed to include the effects of evaporation in the subgrid scalar dissipation modelling. Both macro- and microscopic approaches are essentially modelling the same physics from the different approach, but results very different profiles. These are the questions and possible suggestions for the discrepancy. The spray source term in the $\widetilde{\xi''^2}$ transport equation assumes that the vapour stays unmixed during the LES time steps (Model 2 and 3). However, Bilger's model results very large scalar dissipation rate at high ξ , and it suggests that the diffusion time scale around spray is a lot smaller than the LES time step and cause very rapid mixing. Therefore, the assumption of very high scalar dissipation rate near droplets could lead to a quasi-steady equilibrium condition. It would be possible to develop a model to find $\widetilde{\xi''^2}$ by considering the quick diffusion. In fact, a two-phase LES with the Lagrangian scheme normally assumes all vapour is



(a) Contour plots of the filtered scalar dissipation rate with Model 1 (b) The conditional scalar dissipation rate around a droplet with $10 \mu m$ radius, for two different conditions (droplet temperatures) with $\tilde{\xi} = 0.16$ and $\xi_{surf} = 0.9$ (Blue line) or $\xi_{surf} = 0.3$ (Red line)

Figure A.2: Scalar dissipation rates in different physical scale.

equally distributed among LES cells. However, it is still not applicable to establish the subgrid model based on the microscopic approach yet. Therefore, the current study follows the macroscopic approach, and model the subgrid scalar dissipation by spray evaporation by simply multiplying with the factor. More detailed discussion is given in Sec. 2.4.

Appendix B

Spray Source Terms in Two-Phase CMC Equations

The closures of the spray source terms in CMC equations are proposed in Chapter 4, and this appendix attempts to clarify their discretization approaches. In theory, scalar transport equations (CFD) and CMC equations describe same physics from different approaches, and their solutions should be identical. Thus, the spray source terms in both approaches are compared to validate the closures and discretization for the CMC equations. Here, only to focus on the effects of the spray source terms, unsteady inviscid stationary (no convective velocity) assumptions are enforced. CFD cell quantities are given by following unsteady inviscid stationary (zero-velocity) transport equations as

$$\frac{\partial \rho}{\partial t} = \dot{\rho}, \quad (\text{B.1})$$

$$\frac{\partial \rho \xi}{\partial t} = \dot{\rho}, \quad (\text{B.2})$$

$$\frac{\partial \rho Y_\alpha}{\partial t} = \zeta_\alpha \dot{\rho}, \quad (\text{B.3})$$

where ζ_α is the mass fraction α -th species within liquid vapour, and $\dot{\rho}$ is the spray source term given as (see Sec. 3.3.3)

$$\dot{\rho} = \frac{1}{V} \sum_{n=1}^{N_s} n_{p,n} \dot{m}_{p,n}. \quad (\text{B.4})$$

Similarly, the CMC equation under same assumptions reads as

$$\frac{\partial Q_\alpha}{\partial t} = \left[\zeta_\alpha - Q_\alpha - (1 - \eta) \frac{\partial Q_\alpha}{\partial \eta} \right] \Pi_\eta, \quad (\text{B.5})$$

where Π_η the expansion rate by evaporation modelled in Sec. 4.3.3 as

$$\Pi_\eta = \frac{\tilde{\Pi} \delta(\eta - \tilde{\xi})}{\tilde{P}(\eta)}, \quad (\text{B.6})$$

with

$$\tilde{\Pi} = \frac{1}{\bar{\rho}V} \sum_{n=1}^{N_s} \dot{m}_{p,n} = \frac{\dot{\rho}}{\bar{\rho}}. \quad (\text{B.7})$$

Here, the former approach with the transport equations is referred as the ‘‘Lagrangian approach’’ as it describes the behavior of the CFD cell quantities in the mixture fraction space as a point, and the latter approach with CMC solution is denoted as the ‘‘Eulerian approach’’ that update the conditional quantities in mixture fraction bins. The Lagrangian approach is first analyzed to provide some insights how CMC solution should behave in Sec. B.1, and discretization schemes of the spray source terms are proposed and tested in Sec. B.2. Then, Sec. B.3 demonstrates that the Lagrangian approach and the Eulerian approach with the proposed discretization are equivalent. Finally, Sec. B.4 explains the implementation in the CMC solver.

B.1 Behavior of CFD Cell Quantities (Lagrangian Approach)

The evaporation process increases the mixture fraction and the fuel species mass fraction in each CFD cell, and the cell quantities of a CFD cell in mixture fraction space can be treated as a Lagrangian point. Eqns. B.1 - B.3 are discretized in time and re-written as

$$\rho^{n+1} = \rho^n + \Delta \dot{\rho}, \quad (\text{B.8})$$

$$\rho^{n+1}\xi^{n+1} = \rho^n\xi^n + \Delta\dot{\rho}, \quad (\text{B.9})$$

$$\rho^{n+1}Y_\alpha^{n+1} = \rho^nY_\alpha^n + \zeta_\alpha\Delta\dot{\rho}, \quad (\text{B.10})$$

where $\Delta\dot{\rho}$ is the source term emitted within the time step, Δt , shown as $\Delta\dot{\rho} = \Delta t\dot{\rho}$, and superscripts n and $n + 1$ denote the time step. At the time step n , the CFD quantities represents a Lagrangian point in mixture fraction space at (ξ^n, Y_α^n) , and after the evaporation process (at the time step $n + 1$), the Lagrangian point is shifted to a new location, $(\xi^{n+1}, Y_\alpha^{n+1})$. ξ^{n+1} and Y_α^{n+1} can be represented as:

$$\xi^{n+1} = \frac{\rho^{n+1}\xi^{n+1}}{\rho^{n+1}} = \frac{\rho^n\xi^n + \Delta\dot{\rho}}{\rho^n + \Delta\dot{\rho}} = \frac{\xi + \Delta\Pi}{1 + \Delta\Pi}, \quad (\text{B.11})$$

$$Y_\alpha^{n+1} = \frac{\rho^{n+1}Y_\alpha^{n+1}}{\rho^{n+1}} = \frac{\rho^nY_\alpha^n + \zeta_\alpha\Delta\dot{\rho}}{\rho^n + \Delta\dot{\rho}} = \frac{Y_\alpha^n + \zeta_\alpha\Delta\Pi}{1 + \Delta\Pi}, \quad (\text{B.12})$$

where $\Delta\Pi$ is the volume expansion by spray source defined as $\Delta\Pi = \frac{\Delta\dot{\rho}}{\rho}$. Then, the slope of the shift is given as

$$\frac{dY_\alpha}{d\xi} = \frac{Y_\alpha^{n+1} - Y_\alpha^n}{\xi^{n+1} - \xi^n} = \frac{\zeta_\alpha - Y_\alpha^n}{1 - \xi^n}. \quad (\text{B.13})$$

A sample study is performed to see how a Lagrangian point in mixture fraction space behaves. A profile of mass fraction of acetone, Y_{ace} , is correlated with mixture fraction, and a profile at time step n is given as following three segments:

$$\begin{aligned} Y_{ace} &= 0 & \text{if } \xi < 0.1, \\ Y_{ace} &= 2(\xi - 0.1) & \text{if } 0.1 \leq \xi < 0.2, \\ Y_{ace} &= \xi & \text{if } 0.2 \leq \xi, \end{aligned} \quad (\text{B.14})$$

and the liquid fuel is considered as pure acetone, so $\zeta_{ace} = 1.0$. Here, let us assume that the value of the spray source term is given as $\Delta\Pi = 0.04$ for every CFD cell, the profile after evaporations (at the time step $n + 1$) is obtained as in Fig. B.1. Evaporation acts differently in each of the three segments. In the first segment, ($\xi < 0.1$), the evaporation increases Y_{ace} . However, in the second segment, the addition of the spray source term to reduce the Y_{ace} profiles. It might be wrongly

assumed that the source term should increase Y_{ace} in the region, but the change of Y_{ace} by evaporation (Eqn. B.13) is actually weaker ($\frac{dY_\alpha}{d\xi} \approx 1$) than the gradient of $\frac{dY_\alpha}{d\xi}$ imposed at the time step n ($\frac{dY_\alpha}{d\xi} = 2$). This effect could be also viewed as that the evaporation carries low Y_{ace} mixture into higher mixture fraction space. In the third segment, the evaporation does not influence the slope at all since both of the slope of the profile initial profile and Eqn. B.13 are unity.

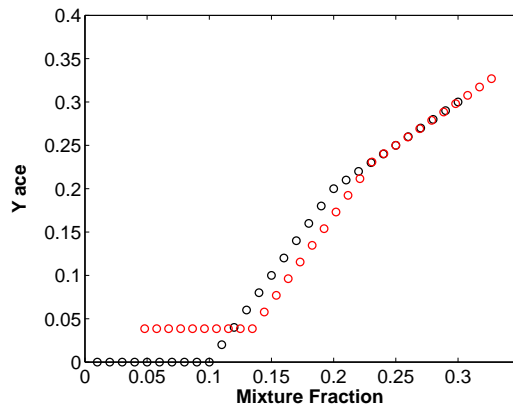


Figure B.1: Comparisons of Y_{ace} profiles between before and after the addition of the spray source term. Black circles - CFD cell quantities at the time step n , red circle - CFD cell quantities at the time step $n + 1$.

B.2 Behavior of Conditional Moments (Eulerian Approach)

The CMC equation describes the change of conditionally averaged quantity in each mixture fraction bin, and the solution should recover the same solution obtained by the Lagrangian approach as in Fig. B.1. Eqn. B.5 discretized in time gives,

$$\Delta Q_\alpha = Q_\alpha^{n+1} - Q_\alpha^n = \Delta t \left[\zeta_\alpha - Q_\alpha^n - (1 - \eta) \frac{\partial Q_\alpha}{\partial \eta} \right] \Pi_\eta, \quad (\text{B.15})$$

and the modelling approaches of $\frac{\partial Q_\alpha}{\partial \eta}$ and Π_η are discussed. First, intuitive discretization schemes (Model 1) are tested, and improved discretization schemes (Model 2) are suggested.

B.2.1 Intuitive Discretization Scheme (Model 1)

Model 1 is established by classical (or so to speak, intuitive) approaches. The discretization of the gradient term in Eqn. B.5, $\frac{\partial Q_\alpha}{\partial \eta}$, can be discretized by a finite difference method as

$$\frac{\partial Q_{\alpha,j}}{\partial \eta} = \frac{Q_{\alpha,j+1} - Q_{\alpha,j-1}}{\eta_{j+1} - \eta_{j-1}}, \quad (\text{B.16})$$

where j denotes the cell index in the mixture fraction space. Also, Π_η is simply modelled based in Eqns. B.6 and B.7 as

$$\Pi_\eta = \frac{\Pi \delta(\eta - \xi)}{P(\eta)} = \frac{\dot{\rho}}{\rho^n} \frac{\delta(\eta - \xi)}{P(\eta)}, \quad (\text{B.17})$$

by conditioning the spray source term on the mixture fraction in a CFD cell before the evaporation at the time step n .

A conditional moment at the time step $n+1$ is computed using the same condition (Eqn. B.14) compared to the Lagrangian solution in Fig. B.2(a). Large offsets from the Lagrangian solution are found where the curvature of the slope is non-zero, and it indicates that the discretization scheme of $\frac{\partial Q_\alpha}{\partial \eta}$ is not appropriate. Also, Fig. B.2(b) shows that a slight difference exists even within the first segment where $\frac{\partial Q_\alpha}{\partial \eta} = 0$, and it indicates that Π_η closed by Eqn. B.17 have overestimated by the conventional discretization. Thus, the discretization approaches should be improved to fix these deficiencies.

B.2.2 Improved Discretization Scheme (Model 2)

Since the Model 1 (or intuitive discretization approach) indicates large offset from the Lagrangian solution, the appropriate discretization for the gradient term, $\frac{\partial Q_\alpha}{\partial \eta}$ and the evaporation term, Π_η are necessary here. Two factors are considered here.

First, the CMC equations should be conditioned at ξ^{n+1} instead of ξ . Considering the Lagrangian approach, the source term added on a Lagrangian point (ξ^n, Y_α^n) moves the point onto $(\xi^{n+1}, Y_\alpha^{n+1})$. Therefore, the source term on ξ^n actually influence statistics at ξ^{n+1} . From the Eulerian (or CMC equation) point of view,

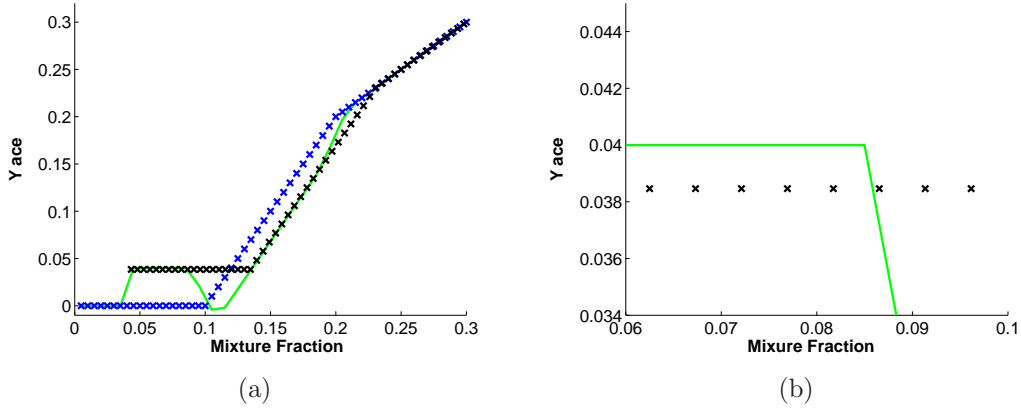


Figure B.2: Comparisons of acetone species profile: Green line - CMC solution with conventional discretization, Blue crosses - CFD cell solutions in the initial profile (at n), Black crosses - CFD cell solutions after the evaporation process (at $n + 1$).

the source term that influences the statistics at ξ^{n+1} should be conditioned by the properties at ξ^{n+1} as well. Therefore, the conditional spray source term can be slightly modified as

$$\Pi_\eta = \frac{\dot{\rho}}{\rho^{n+1}} \frac{\delta(\eta - \xi)}{P(\eta)} = \frac{\Pi' \delta(\eta - \xi)}{P(\eta)}, \quad (\text{B.18})$$

where Π' can be also described as,

$$\Pi' = \frac{\dot{\rho}}{\rho^{n+1}} = \frac{\dot{\rho}}{\rho^n(1 + \Delta\Pi)} = \frac{\Pi}{1 + \Delta\Pi}. \quad (\text{B.19})$$

Secondly, the gradient of Q_α should not be simply modelled by the neighboring mixture fraction bins. Considering the Lagrangian view, the gradient is characterized by two points (ξ^n, Y_α^n) and $(\xi^{n+1}, Y_\alpha^{n+1})$ shown as in Eqn. B.13. Similarly, the gradient of the conditional moment can be represented as

$$\frac{\partial Q_\alpha(\xi^{n+1})}{\partial \eta} = \frac{Q_\alpha^n(\xi^{n+1}) - Q_\alpha^n(\xi^n)}{\xi^{n+1} - \xi^n}, \quad (\text{B.20})$$

and ξ^{n+1} corresponds to the mixture fraction bin η . ξ^n are computed based on be computed by replacing $\xi^n = \xi^{n+1}(1 + \Delta\Pi) - \Delta\Pi$ (by modifying Eqn. B.11), and the corresponding conditional moment $Q_\alpha^n(\xi^n)$ is taken.

Figs. B.3(a) and B.3(b) show improvements of Model 2. The kinks near the

large curvatures have disappeared by introducing the new gradient model. Also, the small offset caused by the evaporation terms in Model 1 is correctly removed by the new evaporation term in Model 2.

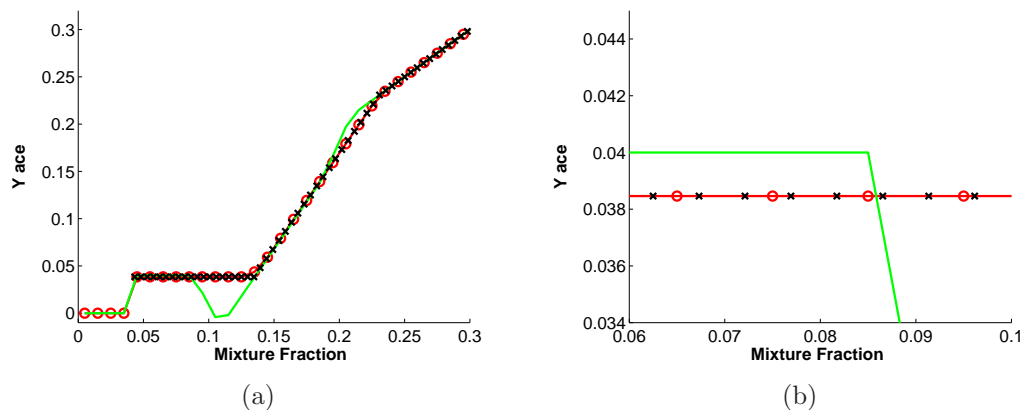


Figure B.3: Comparisons of acetone species profile with improved discretization approaches: Red line with circles - CMC solution with Model 2, Green line - CMC solution with Model 1, Black crosses - CFD cell solutions after the evaporation process.

The test case so far applies a uniform Π in the entire mixture fraction space, and conditional fluctuations of the solution are not included. Thus, another test case with a random evaporation source term is conducted. Π is taken as the random distribution ranged $[0, 0.04]$, and the CMC solutions are compared against the conditionally averaged solution, Q_{ave} , constructed by taking samples of Lagrangian solutions. Fig. B.4 demonstrates that the improved discretization (Model 2) successfully reconstruct Q_{ave} , whereas the intuitive discretization (Model 1) still produces the offsets as seen in the earlier test case (Fig. B.2(a)). Thus, Model 2 is shown to be applicable for general cases.

B.3 Lagrangian vs. Eulerian approaches

This section demonstrates that the discretization approaches in Model 2 in the CMC equation (or the Eulerian approach) is consistent to the CFD (or Lagrangian) solutions. If the Lagrangian and the Eulerian approaches are consistent, a following

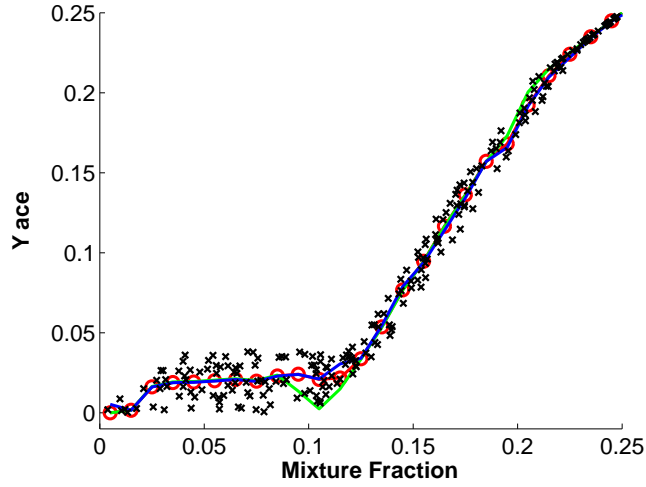


Figure B.4: Comparisons of acetone profiles. Red line with circles - the improved discretization, green line - the intuitive discretization, blue line - the averaged from the Lagrangian solutions, crosses - the analytical Lagrangian solution. Π is taken as the random uniform distribution ranged $[0, 0.04]$.

relation is valid:

$$Q_{\alpha}^{n+1}(\xi^{n+1}) = \Delta Q_{\alpha}(\xi^{n+1}) + Q_{\alpha}^n(\xi^{n+1}) = Y_{\alpha}^{n+1}. \quad (\text{B.21})$$

First, with Model 2, $\langle \Delta Q_{\alpha} | \xi^{n+1} \rangle$ is re-formulated manipulating the CMC equation (Eqn. B.5):

$$\begin{aligned} \Delta Q_{\alpha}(\xi^{n+1}) &= \Delta t \left[1.0 - Q_{\alpha}^n(\xi^{n+1}) - (1 - \xi^{n+1}) \frac{\partial Q_{\alpha}(\xi^{n+1})}{\partial \eta} \right] \Pi_{\eta} \\ &= \left[1.0 - Q_{\alpha}(\xi^{n+1}) - (1 - \xi^{n+1}) \frac{Q_{\alpha}^n(\xi^{n+1}) - Q_{\alpha}^n(\xi^n)}{\xi^{n+1} - \xi^n} \right] \frac{\Delta \Pi}{1 + \Delta \Pi}. \end{aligned} \quad (\text{B.22})$$

The profile of CFD and CMC profiles are consistent at the time step n , so that $Q_{\alpha}(\xi) = Y_{\alpha}$. Also, replacing ξ^n by $(\xi^{n+1}(1 + \Delta \Pi) - \Delta \Pi)$ (by modifying Eqn. B.11),

$$\xi^{n+1} - \xi^n = \xi^{n+1} - \xi^{n+1}(1 + \Delta \Pi) - \Delta \Pi = (1 - \xi^{n+1}) \Delta \Pi. \quad (\text{B.23})$$

Then, Eqn. B.22 is simplified as,

$$\begin{aligned}
& \left[1.0 - Q_\alpha^n(\xi^{n+1}) - (1 - \xi^{n+1}) \frac{Q_\alpha^n(\xi^{n+1}) - Q_\alpha^n(\xi^n)}{\xi^{n+1} - \xi^n} \right] \frac{\Delta\Pi}{1 + \Delta\Pi} \\
&= \left[1.0 - Q_\alpha^n(\xi^{n+1}) - (1 - \xi^{n+1}) \frac{Q_\alpha^n(\xi^{n+1}) - Y_\alpha^n}{(1 - \xi^{n+1}) \Delta\Pi} \right] \frac{\Delta\Pi}{1 + \Delta\Pi} \\
&= \left[1.0 - Q_\alpha^n(\xi^{n+1}) - \frac{Q_\alpha^n(\xi^{n+1}) - Y_\alpha^n}{\Delta\Pi} \right] \frac{\Delta\Pi}{1 + \Delta\Pi} \\
&= [\Delta\Pi - Q_\alpha^n(\xi^{n+1}) \Delta\Pi - Q_\alpha^n(\xi^{n+1}) + Y_\alpha^n] \frac{1}{1 + \Delta\Pi}.
\end{aligned} \tag{B.24}$$

Also, replace $Y_\alpha^n = Y_\alpha^{n+1}(1 + \Delta\Pi) - \Delta\Pi$ (from Eqn. B.12),

$$\begin{aligned}
& [\Delta\Pi - Q_\alpha^n(\xi^{n+1}) \Delta\Pi - Q_\alpha^n(\xi^{n+1}) + Y_\alpha^n] \frac{1}{1 + \Delta\Pi} \\
&= [\Delta\Pi - Q_\alpha^n(\xi^{n+1}) \Delta\Pi - Q_\alpha^n(\xi^{n+1}) + Y_\alpha^{n+1}(1 + \Delta\Pi) - \Delta\Pi] \frac{1}{1 + \Delta\Pi} \\
&= [-Q_\alpha^n(\xi^{n+1}) \Delta\Pi - Q_\alpha^n(\xi^{n+1}) + Y_\alpha^{n+1}(1 + \Delta\Pi)] \frac{1}{1 + \Delta\Pi} \\
&= [-(1 + \Delta\Pi)Q_\alpha^n(\xi^{n+1}) + Y_\alpha^{n+1}(1 + \Delta\Pi)] \frac{1}{1 + \Delta\Pi} \\
&= -Q_\alpha^n(\xi^{n+1}) + Y_\alpha^{n+1}.
\end{aligned} \tag{B.25}$$

Thus, Eqn. B.21 satisfies

$$\Delta Q_\alpha^n(\xi^{n+1}) + Q_\alpha^n(\xi^{n+1}) = -Q_\alpha^n(\xi^{n+1}) + Y_\alpha^{n+1} + Q_\alpha^n(\xi^{n+1}) = Y_\alpha^{n+1}. \tag{B.26}$$

and demonstrates that the discretization in the CMC equation are consistent to the Lagrangian solution.

B.4 Numerical Implementations in CMC Solver

In the previous sections, the closures of the spray source terms are discretized with two different time steps n and $n + 1$. However, during the simulation the conditions are only available at one time step only, and conditions at the other time step (n) must be modelled. Here, the discretization approaches implemented for CMC solver

are presented (see also, Sec. 4.4.2). Π_η is simply represented as

$$\Pi_\eta = \frac{\Pi' \delta(\eta - \xi)}{P(\eta)} = \frac{\Pi}{1 + \Delta\Pi} \frac{\delta(\eta - \tilde{\xi})}{P(\eta)}. \quad (\text{B.27})$$

The gradient term requires a slight transformation to adjust the sample space and given as

$$\frac{\partial Q_\alpha(\eta)}{\partial \eta} = \frac{Q_\alpha(\eta) - Q_\alpha(\eta^*)}{\eta - \eta^*}, \quad (\text{B.28})$$

where η^* is $\eta^* = \eta(1 + \Delta\Pi) - \Delta\Pi$.

Lebenslauf

Persönliche Daten

Name	Ukai, Satoshi
Geburtsdatum und -ort	13, Aug, 1984, Kyoto/Japan
Anschrift	Tilsiter Str. 11 70374 / Stuttgart

Schulischer Werdegang

April 2000 - März 2003	Rakusei High School Kyoto / Japan
-------------------------------	--------------------------------------

Studium

August 2003 - Mai 2007	The University of Texas at Arlington Bachelor of Science in Aerospace Engineering Arlington, Texas / USA
August 2007 - August 2010	Georgia Institute of Technology Master of Science in Aerospace Engineering Atlanta, Georgia / USA

Beruflicher Werdegang

Mai 2005 - August 2005

Undergraduate Research Assistant am
The University of Texas at Arlington

Leiter: Prof. Brian Dennis

August 2005 - Mai 2007

Undergraduate Teaching Assistant am
The University of Texas at Arlington

Leiter: Prof. Frank Lu

August 2007 - Juli 2010

Graduate Research Assistant am
Georgia Institute of Technology

Leiter: Prof. Suresh Menon

Juli 2010 - März 2014

Wissenschaftlicher Angestellter am Institut
für Technische Verbrennung der

Universität Stuttgart,

Leiter: Prof. Dr. Andreas Kronenburg